Motion control design for a 4ws and 4wd overactuated vehicle

Leenen, R.

Award date:
2004

Motion Control Design for a 4ws and 4wd Overactuated Vehicle

Ing. Roel Leenen

DCT 2003.121

Master's thesis

Coach:	Ir. J. Ploeg (TNO Automotive)
Supervisor:	Prof. dr. H. Nijmeijer
Committee members:	Dr. ir. L.P.M. Moreau Dr. ir. F.E. Veldpaus

TNO Automotive
Department Advanced Chassis and Transport Systems
Section New Transportation Systems

Eindhoven University of Technology
Department Mechanical Engineering
Dynamics and Control Technology Group

Eindhoven, January 2004

Preface

This report is the result of a traineeship at TNO Automotive, department of Advanced Chassis and Transport Systems, in partial fulfillment of my graduation at the Technical University Eindhoven, faculty Mechanical Engineering. During my Master's Thesis I participated in the Automatic Guided Vehicle project. The timescale for the traineeship was twelve months, from which one month was spend on Literature research at the Technical University of Eindhoven. I would like to thank prof. dr. Henk Nijmeijer for his supervision and criticism, ir. Jeroen Ploeg at TNO for his support and guidance during this project and dr. ir. L. Moreau, dr. ir. F.E. Veldpaus for participating in my graduation committee.

Summary

In this report, the motion control design for an autonomous four wheel steer and four wheel drive overactuated vehicle is considered. The objective of the motion control is to enable the independent control of the longitudinal translation, lateral translation and orientation angle of the vehicle. A method is designed which handles the redundant number of actuators in the motion control problem.

For that purpose, a non-linear dynamic vehicle model has been formulated which describes the force and momentum equilibria in the longitudinal, lateral and yaw direction of the overactuated vehicle. The empirical tyre model of Pacejka [12], called the "Magic Formula", is used to represent the longitudinal and lateral tyre forces in the model. The steer and drive actuator dynamics are neglected in the modelling.
Secondly, a Dynamic Inverse Algorithm (DIA) has been designed in order to decouple the dynamics of the vehicle. In this dynamic inverse algorithm, an objective function consisting of the model error equations, the estimated vertical wheel loads and some additional constraints are formulated in order to deal with the redundancy. Given a smooth reference trajectory, the minimization of the objective function results in four optimal reference wheel rotational velocities and four optimal reference steer angles. For the real-time application of the algorithm, the objective function is minimized once during each sample interval using the previous obtained 'minimum' as an initial starting guess in the iterative optimization process.
The steer and drive commands are dealt with by closing local loops around each steer and drive actuator; the presence of large friction forces makes it a necessity to apply servo control. A master-slave control structure is proposed for the motion control of the vehicle. With the servo controllers in the slave loop, a proportional controller in the outer feedback loop, combined with a feedforward acceleration input, is used for the trajectory tracking. Furthermore, estimated longitudinal tyre forces are used in the feedforward compensation for the drive actuators in order to increase the tracking performance.

Typical vehicle manoeuvres are evaluated through simulation and experiment in order to assess the performance of the motion controller. The simulation results show that the control system is capable of coordinating all eight actuators of the vehicle up to limit tyre adhesion conditions without excessive wheel slip. The algorithm explicitly handles the saturation of the longitudinal and lateral tyre forces according to the modelled force/slip-characteristics of the tyre. Initial experimental results show that the algorithm is successfully implemented. However, more experiments have to be conducted in order to assess the algorithm's potential.

Samenvatting

In dit rapport wordt een positie regeling ontworpen voor een autonoom vier wiel gestuurd en vier wiel aangedreven overgeactueerd voertuig. Het doel van de regeling is om de longitudinale translatie, de laterale translatie en de orientatie hoek van het voertuig onafhankelijk van elkaar te kunnen regelen. Een methode is ontworpen waarbij expliciet rekening gehouden wordt met de hoeveelheid aan actuatoren.

Om dit te bereiken is er een niet-lineair dynamisch voertuig model opgesteld waarin een krachten en momenten evenwicht wordt beschouwd voor de longitudinale richting, de laterale richting en de rotatie van het voertuig om het zwaartepunt. Het empirisch bandmodel van Pacejka, ook wel bekend als de "Magic Formula", is gebruikt voor het modelleren van de longitudinale en de laterale bandkracht. De actuator dynamica wordt niet beschouwd in dit model.
Ten tweede, een Dynamisch Inverteer Algoritme (DIA) is ontworpen voor het ontkoppelen van de dynamica in het voertuigmodel. In dit dynamisch inverteer algoritme wordt een doelfunctie opgesteld, welke bestaat uit model fouten, een geschatte verticale wielbelasing en additionele constraint vergelijkingen, om zodanig te kunnen omgaan met de hoeveelheid aan actuatoren in het regelprobleem. Op voorwaarde van een glad referentie traject resulteert het minimaliseren van de doelfunctie in vier optimale referentie waarden voor respectievelijk de stuurhoeken en de wiel omwentel snelheden. Om het algoritme 'online' te kunnen toepassen wordt de doelfunctie tijdens elk sample interval geminimaliseerd, waarbij de vorige oplossing gebruikt wordt als beginwaarde voor de optimalisatie.
De verkregen referentie waardes voor de stuur en aandrijf actuatoren worden gebruikt om locale servo-regelingen aan te sturen; de aanwezigheid van grote frictie krachten tussen de band en het wegdek maakt het gebruik van servo-regelingen noodzakelijk. Een Master-slave architecture is gebruikt voor de positie regeling van het voertuig. Met de servo-regelaars in de slaaflus wordt er voor de positie regeling in de buitenste lus een proportionele terugkoppeling in combinatie met een versnelling feedforward gebruikt.
Om de prestaties van de positie regeling te kunnen beoordelen worden er typische voertuig manoeuvres gesimuleerd en geëxperimenteerd. De simulaties wijzen uit dat het algoritme in staat is om de hoeveelheid aan actuatoren op een gecontroleerde manier aan te sturen tot aan het grensbereik van het voertuig model. Het algoritme houdt expliciet rekening met de saturaties van de longitudinale en lateral bandkracht. Experimentele resultaten bevestigen een succesvolle implementatie van het algoritme. Echter, er zullen meer experimenten moeten worden uitgevoerd om de mogelijkheden van het algoritme volledig te kunnen benutten.

Glossary of symbols

Symbol	Unit	Description
B	$-$	Magic formula parameter
C	$-$	Magic formula parameter
D	$-$	Magic formula parameter
F	N	Tyre force
F_z	N	Vertical wheel load
H	$-$	Plant transfer function
H_h	$-$	Hessian matrix of objective function
I_z	kgm^2	Vehicle inertia in center of gravity
J	kgm^2	Inertia
L	m	Distance from vehicle center of gravity to wheel axle
M	Nm	Momentum in the center of gravity of the vehicle
R	m	Wheel radius
R_e	m	Effective wheel radius
S	m	Wheel axle width
T	Nm	Torque
T_d	Nm	Disturbance torque
a	m/s^2	Acceleration in vehicle coordinate frame
a_p	m/s^2	Acceleration in operational coordinate frame
c	N	Linear tyre stiffness
e	m	Tracking error in operational space coordinates
e_p	$m/s^2, rad/s^2$	Control model error
g	m/s^2	Gravitational constant
h	$-$	Objective function
i	$-$	Gear ratio
$k_{s,p}$	$-$	Proportional gain in steer servo controller
k_p	$-$	Proportional gain in tracking controller
$k_{w,p}$	$-$	Proportional Gain in drive servo controller
$k_{w,i}$	$-$	Integral Gain in drive servo controller
m	kg	Vehicle mass
ψ	rad	Vehicle orientation angle
$\dot{\psi}$	rad/s	Vehicle angular velocity
$\ddot{\psi}$	rad/s^2	Vehicle angular acceleration

Symbol	Unit	Description
q	$-$	Weight parameter in objective function h
r	$-$	Combined slip weight parameter
s	$-$	Stepsize resulting from optimization
t	sec	Time
u	Nm	Actuator input
v	m/s	Velocity in vehicle coordinate frame
x	m	X-position in global coordinate frame
$\dot{x}$	m/s	First derivative of x
$\ddot{x}$	m/s^2	Second derivative of x
y	m	Y-position in global coordinate frame
$\dot{y}$	m/s	First derivative of y
$\ddot{y}$	m/s^2	Second derivative of y
z	$-$	Virtual input variable
α	$-$	Lateral slip value
β	rad	Side slip angle
δ	rad	Steer angle
$\dot{\delta}$	rad/s	Steer velocity
$\ddot{\delta}$	rad/s^2	Steer acceleration
θ	rad	Orientation angle of the operational space coordinate frame
κ	$-$	Longitudinal slip value
μ	$-$	Tyre/road-friction coefficient
ν	m/s	Velocity at wheel corner
ν_w	m/s	Velocity in wheel plane at the wheel corner
ξ	rad	Servocompensator state variable
σ	sec	Tyre relaxation length
τ	sec	Time constant
ω	rad/sec	Wheel rotational velocity
$\dot{\omega}$	rad/sec^2	Derivative of the wheel rotational velocity
$\triangle t$	sec	Sample time
∇h	$-$	Gradient of objective function h
$\mathbf{a}_p$	$-$	Vector with acceleration compenents in operational space coordinates
$\mathbf{e}$	$-$	Vector with tracking error components in operational space coordinates
$\mathbf{f}_1$	$-$	Vector with vehicle body dynamics
$\mathbf{f}_2$	$-$	Vector with actuator dynamics
$\mathbf{f}$	$-$	Vector with the control model dynamics
$\mathbf{K}_p$	$-$	Matrix with tracking controller gains
$\mathbf{p}$	$-$	Vector with the operational space state variables
$\mathbf{R}$	$-$	Coordinate rotation matrix
$\mathbf{u}$	$-$	Vector with actuator inputs
$\mathbf{U}$	$-$	Vector with inputs for the Dynamic Inverse Algorithm
$\mathbf{x}_1$	$-$	Vector with vehicle state variables
$\mathbf{x}_2$	$-$	Vector with actuator state variables
$\mathbf{z}$	$-$	Vector with virtual inputs

Indices	Description
0	Pure longitudinal or lateral tyre behavior.
α	Lateral slip component
d	Disturbance
drv	Drive actuator or servo
$filt$	Filtered
F	Front
g	wrt Global coordinate frame
$ideal$	Ideal value
ij	Wheel index
k	Iteration number
κ	Longitudinal slip component
lat	Lateral component
$long$	Longitudinal component
m	Measured
nom	Nominal value
$norm$	Normalized value
$p1$	P1-direction in operational space coordinate frame (longitudinal)
$p2$	P2-direction in operational space coordinate frame (lateral)
$p3$	P3-direction in operational space coordinate frame (angular)
$peak$	Peak value
ref	Reference value
R	Rear
s	Steer
str	Steer actuator or servo
w	Wheel
x	Longitudinal direction
y	Lateral direction
z	Vertical direction

Contents

Chapter 1

Introduction

1.1 Motivation

Nowadays, wheeled mobile robots are a common practise in industry. They are often used for autonomous path following purposes, thereby increasing the transport efficiency or level of automation, which in turn results in a cost reduction. TNO Automotive is currently developing a unique autonomous wheeled mobile robot or Automatic Guided Vehicle, called ATS/AGV - 'Advanced Transport Systems / Automatic Guided Vehicle', which will be operated in the VEHIL test laboratory [15]. The ATS/AGV is capable of extreme manoeuvring at high velocity. Moreover, its dynamic response on position commands should considerably exceed the handling performance of modern road vehicles. This results in a set of control requirements for the ATS/AGV that is new in the world of automated vehicles. The research described in this report focusses on the motion control design for this experimental facility.

The motion control of the ATS/AGV is defined as the tracking of two position coordinates and a vehicle orientation angle in the horizontal plane. The design of the vehicle chassis has an independent four wheel steer and independent four wheel drive actuator configuration. So there are a total of eight actuator inputs available. Since there are more actuator inputs than degrees of freedom in the motion control problem, the vehicle is actually an overactuated system. In the motion control of the vehicle one typically has to deal with the coordination of the redundant number of actuators. For the manoeuvring of the vehicle there typically exists more than one allowable actuator configuration. Furthermore, due to the extreme manoeuvring requirements, wheel slip can not be neglected in the motion control. The saturating non-linear tyre/road-contact behavior has to be considered in the control design in order to improve the tracking performance of the ATS/AGV.

In this project, the actuator redundancy in the motion control of the vehicle will be dealt with through the use of numerical optimization techniques in combination with the formulation of a performance criterion.

1.2 Definition of the project objectives

In this project, the motion control of an autonomous four wheel steer and four wheel drive overactuated vehicle is considered. The objectives of this project are twofold:

- Design a control system which enables the decoupled input-output control of the longitudinal translation, lateral translation and orientation angle of the vehicle. This typically requires the design of a method which handles the redundant number of actuators in the motion control problem.
- Evaluate the control design by means of simulations and real-time experiments with the ATS/AGV.

1.3 Outline of the report

The report is organized as follows:

Chapter 2 contains the literature study conducted with respect to wheeled mobile robots and overactuated systems in general. Chapter 3 describes the analysis of the relevant vehicle dynamics for the control design in this project. The fundamental tyre behavior and the actuator modelling is discussed first, after which a two-track dynamic vehicle model is presented, which forms the basis of the control design. In chapter 4, the dynamic inverse problem is defined. It comprises the essence of the motion control problem, which is the decoupled control of an overactuated vehicle. Chapter 5 proposes the solution method to the dynamic inverse problem, in the form of a Dynamic Inverse Algorithm. In chapter 6, the feedback controllers for the ATS/AGV are discussed. They consist of local servo controllers for the driving and steering and an outer loop controller for the trajectory tracking. Finally, simulations and experimental results are presented in chapter 7 and 8, respectively. The final chapter contains conclusions about the obtained results and gives recommendations for future research.

Chapter 2

Literature

This chapter is the result of a literature study conducted on relevant topics concerning the control of a four wheel steered and four wheel driven (4ws+4wd) overactuated Automatic Guided Vehicle. In the robotics research field, the ATS/AGV falls within the class of Wheeled Mobile Robots (WMRs). The focus of this literature study will be mainly on the research conducted on the control and modelling of WMRs, and overactuated WMRs in particular.
In section 2.1 a distinction is made between a holonomic and nonholonomic dynamical system. Section 2.2 gives a short survey of the modelling and control of WMRs in general. Relevant topics concerning the overactuated WMRs in particular are discussed in section 2.3. The conclusions drawn from this literature study are summarized in section 2.4 and indicate the outline of the research performed in this project.

2.1 Holonomic or nonholonomic

The motion control of a WMR involves the notion that there are constraints on the (wheel) velocity of the mobile robot. The constraints arise either from the nature of the controls that can be physically applied to the system or from conservation laws which apply to the system. For instance, a car like robot with two front drive steering wheels and two fixed rear wheels cannot move sideways. And unanchored robots in space are difficult to control with thrusters because they conserve total angular momentum. These type of systems are examples of typical mechanical nonholonomic systems subjected to kinematic constraints of the form

$$\mathrm{f}(\dot{q}_1, \dot{q}_2, ..., \dot{q}_n; q_1, q_2, ..., q_n; t) = 0 \tag{2.1}$$

where $q_1, ..., q_n$ are the generalized coordinates of the mechanical system with derivatives $\dot{q}_1, ..., \dot{q}_n$. Equation (2.1) implies that there are velocity restrictions on the motion of the mechanical system.

Definition 2.1:
A mechanical system is defined to be nonholonomic when the kinematic constraints are not integrable with respect to time. If these constraints are integrable with respect to time, into the so called geometric constraints h (q;t)=0, i.e. the constraint (2.1) follows from this geometric constraint via differentiation, the mechanical system is said to be

holonomic.

In literature, a mobile robot is either characterized as an holonomic or a nonholonomic system. However, in the case of a four wheel steered WMR there are some implications in determining the nature of the system. The wheel as a mechanical system is nonholonomic because it can not move sidewards. But since each wheel can be oriented independently, and thus enabling 'instant' sideward movement of the robot, the system as a whole is in fact holonomic. The point is that the velocity of the steer actuator is finite and consequently there will always be a phase delay in the commanded wheel orientations. This phase delay increasingly influences the holonomic behaviour of the four wheel steered WMR when operating the robot at higher frequencies. As a consequence hereof, the holonomic system will eventually show a nonholonomic behavior.

2.2 Wheeled mobile robots

The first step in the approach towards the control of the WMR is the formulation of a kinematic and dynamic model. G.Campion, G.Bastin and B.D'Andrea-Novel [6, 1] were among the first to formulate a general approach for the modelling of WMRs in which different wheel configurations are considered. The considered WMR is typically characterized by kinematic constraints that are not integrable (nonholonomic) and therefore cannot be eliminated from the model equations. The kinematic constraints are based on a pure rolling motion (no-slip) of the wheels and the velocity properties orthogonal to the wheel plane. The constraints are satisfied if and only if: a. either the perpendiculars to the plane of each wheel (drawn from the center of the wheel) are all concurrent in an instantaneous center of rotation (ICR) or b, the wheels are all parallel, i.e. the robot motion is a pure translation.
Campion et al. found that according to the restriction on the mobility induced by the kinematic constraints, all WMR can be classified into 5 types, characterized by generic structures of the model equations. For each type of model the following questions were addressed: (ir)reducibility and (non)holonomy, mobility and controllability, configuration of the motorization, and feedback equivalence.

2.3 Overactuated wheeled mobile robots

From a control point of view, mobile robots equipped with two or more steering wheels have the additional problem that their configuration space presents intrinsically some singular points. For example, consider the sideward movement of a four wheel steered WMR at a constant forward velocity. The wheels are steered according to the desired sideward velocity. A singularity in the control of the WMR will be met when the wheels are steered such that the ICR lies in the center of a wheel (or close enough to it). Control strategies must be designed in such a way that it will be guaranteed that the singularities will not be met during the robot motion. With regard to the tracking, the reference trajectory can be used to keep the robot away from singularities. The only period where singularities might be met is therefore the transient phase when the robot converges to the reference trajectory. Thuilot et al. [14] provided conditions on the initial error between the robot configuration and the reference trajectory, which

are sufficient to ensure that singularities will not be met during the transient phase. It is a general approach for mobile robots and has the advantage that the same approach can be used for the avoidance of obstacles.
In the method suggested in [14], the same kinematical modelling as in [6, 1] was performed. This means that it is assumed that the contact between the wheels and the motion plane obeys the pure rolling and non-slipping conditions (a and b from section 2.2). The term admissible wheel configuration (AWC) was defined in order to translate the prerequisites a and b into implementation details. The AWC are the only wheel configurations compatible with the pure rolling and no slipping assumptions, and thus the only ones that allow the robot to move. A subset of the AWC is the defined singular wheel configuration (SWC). When the number of steering wheels $n \geq 3$: the SWC consist of all the AWC whose associated ICR is located on a wheel center $WC_{1 \leq i \leq n}$ (or close enough to it). Note that the situation when the front wheels are pointed in a direction opposite to the rear wheels is not an AWC and hence automatically rejected by the definition of AWC. These SWC have to be avoided at all cost from a control point of view. The two defined sets of configurations provide us a description of the allowable wheel configurations. Besides the SWC, the coordinates of its associated ICR can identify any AWC without ambiguity (each AWC has one unique ICR (and vice versa) in the motion plane).

If the number of steer wheels is larger than the controllable planar degrees of freedom, then the motion of the 'extra' wheels must be coordinated to guarantee the existence of the ICR at each time instant [6]. Bendtsen et al. proposed in [5] a master-slave concept in which the orientation of the 'extra' wheels is subjected to the steer angles of the master wheels by a geometrical relation ($\beta_{3,4} = f(\beta 1, \beta 2)$), and thereby guaranteed the existence of an ICR for the independent four wheel steer and independent four wheel drive vehicle in their study. Following the approach taken in [6, 1], they presented a dynamic model of the vehicle based on the kinematic constraints. In the modelling it was assumed that there is no wheel slip. The model is highly non-linear and involves nonholonomic constraints, therefore an input-output feedback linearization based control law was designed to solve the trajectory tracking problem. The presence of large friction forces made it a necessity to use computed torques (linearization of control) and local servo loops around the steering motors. As the system is overactuated a torque distribution for the four driving motors was suggested. The minimization of the maximum torque applied to any wheel at a given moment was chosen as the torque distribution criterion.
Feedback linearization designs are sensitive to model uncertainties, since the technique explicitly cancels the nonlinearities. Besides uncertainties also sensor noise and actuator saturation play an important role. These may all lead to the instability of the controlled vehicle. As a consequence hereof, a robustness analysis of the feedback linearization design is conducted. It was shown that even quite limited uncertainties can cause instability under normal driving conditions. Two approaches were suggested to deal with this problem:

1. minimize the effects of the uncertainties in the model using local feedback loops

2. guarantee an upper bound on the perturbations to the nominal linearized system by avoiding planned (local) paths that tends to destabilize the robot

Rolling assumptions are violated in tractive manoeuvring of WMRs, predominantly due to wheel slip [4, 3]. The problem of traction control for WMRs is of enormous importance to the automotive industry. Traction control systems reduce or eliminate excessive wheel slip during vehicle acceleration or deceleration and thus enhance the controllability and manoeuvrability of the vehicle. Traction control aims to achieve maximum torque transfer from the wheel axle to the forward acceleration. The friction force between the tyre and the road is the main mechanism for converting wheel angular acceleration (due to the motor torque) to forward acceleration (longitudinal force). Therefore, the study of friction force characteristics at the tyre/road interface has received a great deal of attention in the automotive literature [8].

2.4 Summary

The mobility literature of wheeled mobile robots is traditionally founded on the kinematic models derived from the rolling with no-slip constraints on the wheels. Together with the wheel orientation encoders that are used to infer the configuration (end-point) of the mobile robot, these constraints are convenient in reducing the order of the state-space description of the mobile robot. However, in practice, wheel-slip-induced disturbances on the kinematic constraints are inevitable, especially when there are high performance requirements on the robot's mobility. Slip dynamics play a more significant role at high velocities and accelerations of the mobile robot.
The independent four wheel steer and independent four wheel drive configuration of the ATS/AGV is considered. The fact that there are eight actuators available for the control of three degrees of freedom of the vehicle makes the system overactuated. Possible solutions in order to deal with this redundancy are found in literature. It appears that in the discussed literature it is common to introduce an instantaneous center of rotation (ICR). The (slave) steering wheels are then subjected to this ICR in order to deal with the redundancy. The location of the ICR then mainly controls the manoeuvring and hence the stability of the vehicle. A disadvantage of the ICR is that it is used to control the 'ideal' steer angles in a no-slip scenario. In addition, the use of an ICR severely restricts the manoeuvrability of the ATS/AGV, since the vehicle is capable of performing manoeuvres in which the existence of a single ICR can not be guaranteed.
The one thing that separates the ATS/AGV from most of the other wheeled mobile robots or car-like vehicles are the extreme manoeuvring and accelerating requirements. Because of it, wheel slip can not be neglected in the dynamic modelling of the ATS/AGV. Therefore, the saturating non-linear tyre-road contact behavior has to be considered in the control design in order to improve the tracking performance of the AGV in extreme conditions.

Chapter 3

Analysis of vehicle dynamics for control design

In this chapter, the relevant dynamics of the vehicle will be described. In section 3.1.2, a short overview of the proposed tyre model equations is given. Then in section 3.1.3, the dynamic models of respectively the drive and steer actuator are analyzed. Finally, in section 3.2, all the submodels are combined into one model, called the two-track vehicle model, which forms the basis of the control design process. The ATS/AGV and its technical specifications are formally introduced in appendix A.

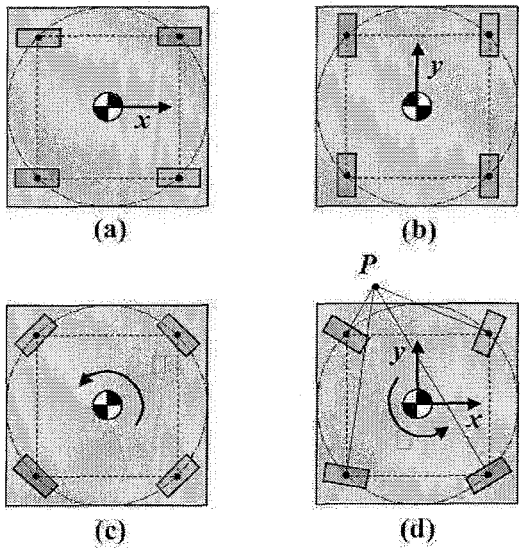

Figure 3.1: Types of motion with three degrees of freedom.

The degrees of freedom in the motion of the vehicle are explained first. The vehicle platform is equipped with independent all-wheel steering, and consequently independent all-wheel drive, as depicted in figure 3.1. This figure illustrates the platform's capability of motion in x-direction (a), crab-like motion in y-direction (b), pure ro-

tation around its center of gravity (c) as well as any combination of these types of motion, i.e. rotation around a momentary pole P (d).

3.1 Fundamentals

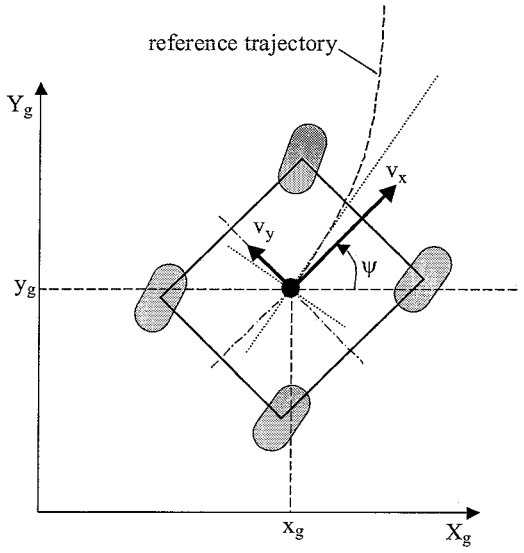

Figure 3.2: Definition of posture coordinates **x** and vehicle space coordinates **v**

3.1.1 Change of coordinates

The posture coordinates $[x_g \;\; y_g \;\; \psi]^T$ which define the absolute position and orientation of the vehicle in the reference frame fixed to the world, are given in figure 3.2. In deriving a vehicle model for the ATS/AGV, the velocity coordinates $[v_x \;\; v_y \;\; \dot{\psi}]^T$ are introduced, see also figure 3.2. These new coordinates describe the longitudinal, lateral and angular velocity of the center of gravity of the vehicle and are fixed to the chassis. They are thereby referred to as vehicle space coordinates. The velocity coordinates in vehicle space are calculated with the rotation matrix $\mathrm{R}(\psi)$ and the derivatives of the posture coordinates.

$$\begin{bmatrix} v_x \\ v_y \\ \dot{\psi} \end{bmatrix} = \begin{bmatrix} \cos(\psi) & \sin(\psi) & 0 \\ -\sin(\psi) & \cos(\psi) & 0 \\ 0 & 0 & 1 \end{bmatrix} \cdot \begin{bmatrix} \dot{x}_g \\ \dot{y}_g \\ \dot{\psi} \end{bmatrix} = \mathrm{R}(\psi) \begin{bmatrix} \dot{x}_g \\ \dot{y}_g \\ \dot{\psi} \end{bmatrix} \tag{3.1}$$

From now on, the modelling of the vehicle will be described in vehicle space coordinates only. The velocities $\nu_{x,ij}$ and $\nu_{y,ij}$ are denoted as the wheel corner velocities, in longitudinal and lateral vehicle direction, respectively, and are calculated for each wheel. The subscript ij is used to distinguish between the four tyres of the ATS/AGV, i = 1, 2 for the front and rear axle and j = L, R for the left and right side of the vehicle,

respectively. A general formulation for the wheel corner velocity is

$$\nu_{ij} = \begin{bmatrix} \nu_{x,ij} \\ \nu_{y,ij} \end{bmatrix} = \begin{bmatrix} v_x \\ v_y \end{bmatrix} + \mathrm{q}_{ij}\dot{\psi} \tag{3.2}$$

in which q_{ij} is the position vector of the wheel corner originating from the center of gravity and expressed with respect to the vehicle space coordinate frame. For the front left wheel corner they read for example:

$$\begin{aligned} \nu_{x,1L} &= v_x - S_F/2 \cdot \dot{\psi} \\ \nu_{y,1L} &= v_y + L_F \cdot \dot{\psi} \end{aligned}$$

Characteristic dimensions are the distance from center of gravity to the two axles denoted as L_F and L_R for the front and rear axle and axle width S_F and S_R, respectively. A complete overview of the longitudinal and lateral wheel corner velocities can be found in appendix B. It is important to note that a distinction is made between the wheel corner velocities ν_{ij} (3.2), which are used for the calculation of the ideal steer angle $\delta_{ideal,ij}$, on one hand and the wheel plane velocities $\nu_{w,ij}$, which are used for the calculation of the wheel slip values, on the other hand. See also figure 3.3. The wheel plane velocities consist of a longitudinal component parallel to the wheel plane, $\nu_{x,w,ij}$, and a lateral component perpendicular to the wheel plane, $\nu_{y,w,ij}$. Both velocities originate from the wheel center of rotation. A general formulation of the wheel plane velocities in combination with the velocities calculated in (3.2) reads as follows

$$\nu_{w,ij} = \begin{bmatrix} \nu_{x,w,ij} \\ \nu_{y,w,ij} \end{bmatrix} = \begin{bmatrix} \cos(\delta_{ij}) & \sin(\delta_{ij}) \\ \sin(\delta_{ij}) & -\cos(\delta_{ij}) \end{bmatrix} \cdot \begin{bmatrix} \nu_{x,ij} \\ \nu_{y,ij} \end{bmatrix} \tag{3.3}$$

Where δ_{ij} is the steerangle, defined to be the angle between the longitudinal wheel plane and the longitudinal chassis direction.

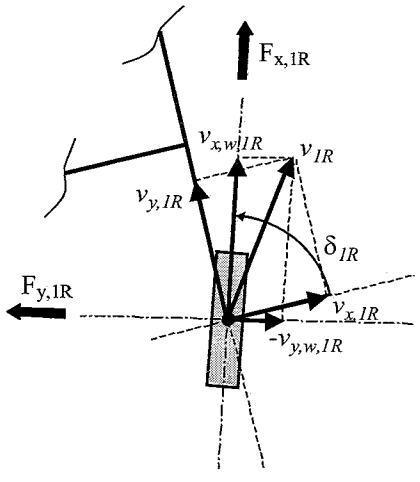

Figure 3.3: Graphical depiction of the components of the wheel corner velocity ν_{1R} and the wheel plane velocity $\nu_{w,1R}$ for the front right wheel.

3.1.2 Tyre modelling

The force/slip models of Pacejka [12], which are discussed in more detail in appendix C, are considered for the modelling of the tyre characteristics of the ATS/AGV. The Magic Formula has been shown to suitably match experimental data, obtained under particular conditions of constant translational and rotational velocities. A simplified version of this Magic Formula is used to model the longitudinal tyre force $F_{x,ij}$ and the lateral tyre force $F_{y,ij}$. The steady-state longitudinal slip value κ and the steady-state lateral slip value α are derived from the wheel velocities represented by (3.2) and (3.3):

$$\kappa_{ij} = \frac{R_e \cdot \omega_{ij} - \nu_{x,w,ij}}{|\nu_{x,w,ij}|} \tag{3.4}$$

$$\alpha_{ij} = -\frac{\nu_{y,w,ij}}{|\nu_{x,w,ij}|} \tag{3.5}$$

and are used as inputs to the tyre model. $\omega_{ij}\,[rad/s]$ is the wheel rotational velocity and $R_e\,[m]$ the effective rolling radius of the tyre. $\nu_{x,w,ij}$ and $\nu_{y,w,ij}$ are the longitudinal and lateral wheel plane velocities in $[m/s]$. When it is assumed that $\nu_{x,w,ij} > 0$, the following relation holds:

$$\alpha_{ij} = \tan(\delta_{ij} - \delta_{ideal,ij}) \tag{3.6}$$

with

$$\delta_{ideal,ij} = atan\left(\frac{\nu_{y,ij}}{\nu_{x,ij}}\right) \quad \text{for} \quad \nu_{x,w,ij} > 0 \tag{3.7}$$

The ideal steering angle $\delta_{ideal}\,[rad]$ is defined as the steer angle at which there would be no lateral wheel slip, or the velocity perpendicular to the wheel plane is equal to zero. The velocities $\nu_{x,ij}$ and $\nu_{y,ij}$ are the velocities at the wheel corner, in longitudinal and lateral direction of the vehicle chassis, respectively.

The pure force/slip model for modelling the tyre behavior of the ATS/AGV then becomes:

$$F_{x,ij,0}(\kappa_{ij}, F_{z,ij}) = D_{x,norm} \sin(C_{x,norm} \arctan(B_{x,norm}\kappa_{ij}))F_{z,ij} \tag{3.8}$$

$$F_{y,ij,0}(\alpha_{ij}, F_{z,ij}) = D_{y,norm} \sin(C_{y,norm} \arctan(B_{y,norm}\alpha_{ij}))F_{z,ij} \tag{3.9}$$

in which the pure longitudinal tyre force $F_{x,ij,0}$ and pure lateral tyre force $F_{y,ij,0}$ are assumed to be proportional to the vertical wheel load F_z. Also, the parameters B_{norm}, C_{norm} and D_{norm} are assumed to be constant. Note that these assumptions are not reasonable when the wheel load variations of the ATS/AGV are significant. The assumed pure longitudinal and lateral force/slip-characteristics for the modelling of the ATS/AGV, normalized with respect to the vertical wheel load F_z, are illustrated in fig 3.4. The tyre model parameters B_{norm}, C_{norm} and D_{norm} are based on the available technical specifications of the used formula SAE tyres obtained under average road/friction conditions.
It can be seen that the tyre has the characteristic that for small values of slip the force generation is approximately proportional to the slip. As the slip increases the force reaches a point of saturation after which it declines. In the modelled force/slip-curves the longitudinal force reaches this point of saturation at approximately 0.06 slip, i.e.

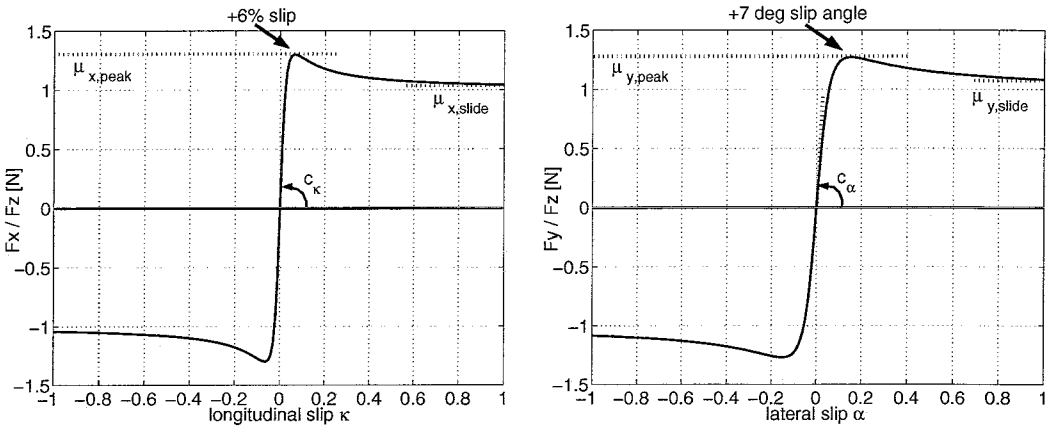

Figure 3.4: Typical force/slip characteristics; pure longitudinal (left) and pure lateral (right).

a slip percentage of 6%. For the lateral force the maximum is reached at an approximately 7 deg ($= atan(\alpha)$) slip angle. One can see that the shape of the curves show a similar behavior for the longitudinal and lateral direction. The slopes of the curves in the linear region of the characteristic are denoted as c_κ and c_α for the longitudinal and lateral direction, respectively. The maximum longitudinal and lateral friction coefficients $\mu_{x,peak}$ and $\mu_{y,peak}$ (also shown in figure 3.4) determine the maximum level of friction in the corresponding direction.
It is chosen to model the combined slip situation for the tyres. The parameters (rx_1, rx_2, ry_1, ry_2) in the combined slip weight functions however, have to be based on assumptions, since in this study it is not possible to validate them with experimental tyre data. The combined slip weight functions are [12]:

$$B(\kappa)_{x,ij} = rx_1 \cdot \cos(\arctan(rx_2 \cdot \kappa_{ij})) \tag{3.10}$$
$$G(\kappa,\alpha)_{x,ij} = \cos(\arctan(B(\kappa)_{x,ij} \cdot \alpha_{ij})) \tag{3.11}$$
$$B(\alpha)_{y,ij} = ry_1 \cdot \cos(\arctan(ry_2 \cdot \alpha_{ij})) \tag{3.12}$$
$$G(\kappa,\alpha)_{y,ij} = \cos(\arctan(B(\alpha)_{y,ij} \cdot \kappa_{ij})) \tag{3.13}$$

the combined force/slip model then becomes

$$F_{x,ij}(\kappa_{ij},\alpha_{ij},F_{z,ij}) = G(\kappa,\alpha)_{x,ij} \cdot F_{x,ij,0}(\kappa_{ij},F_{z,ij}) \tag{3.14}$$
$$F_{y,ij}(\kappa_{ij},\alpha_{ij},F_{z,ij}) = G(\kappa,\alpha)_{y,ij} \cdot F_{y,ij,0}(\alpha_{ij},F_{z,ij}) \tag{3.15}$$

Because of the combined slip, strong interactions between the longitudinal and lateral direction of the tyre as a force actuator occur. This will definitely make the control design of the overactuated vehicle more challenging. When driving and steering the wheel at the same time, a compromise has to be made between its longitudinal and lateral force actuation. For a more detailed analysis of the behavior of the tyre model, the reader is referred to appendix C.

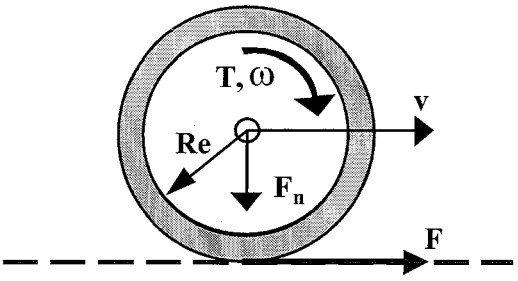

Figure 3.5: Quarter car model

3.1.3 Actuator modelling

In this section, the dynamics of the actuators are studied. Because of the limited bandwidth of the steer and drive actuator, plus the non-linear and saturating force/slip behavior of the tyre, the actuator dynamics are to be considered in the vehicle model. Especially when operating the ATS/AGV in extreme conditions. In contrast to the drive actuator dynamics, the steer actuator dynamics are rather straightforward, which will therefore be discussed in short detail at the end of this section.

The drive actuator

At the top level, the drive actuator can be seen as the system which converts a torque input to the wheel into a tyre/road-friction force which propels a certain attached mass in an horizontal direction. In order to get a better understanding of the dynamics of the drive actuator, a quarter car model is illustrated in figure 3.5.
Divided into dynamic submodels from input to output, the system consists of a dc-motor, gearbox, wheel rim and finally the tyre. The dynamic behavior of the tyre depends on several input variables and time-varying parameters, such as the vertical wheel load, the longitudinal and lateral wheel slip, the relaxation length, and the road friction coefficient. When operated at small levels of wheel slip, the tyre can be seen as a two-dimensional force generator which shows time-varying linear dynamic behavior. When operated at large levels of wheel slip (e.g. $\kappa \rightarrow \kappa_{peak}$) the tyre reaches the maximum tyre/road friction level. At this point, the tyre force saturates and operating the level of wheel slip beyond the peak value κ_{peak} will degenerate the tyre force (e.g. a negative damping effect occurs). The region of interest for controlling the ATS/AGV lies left from the peak slip value in the force/slip characteristic.

$$m\dot{v} = F(\kappa) \qquad [N] \qquad (3.16a)$$

$$\sigma(\kappa)\dot{\kappa} = -|v|\kappa + R_e\omega - v \qquad [-] \qquad (3.16b)$$

$$J_w\dot{\omega} = -B_w\omega - R_eF(\kappa) + i_{drv}T_{drv} \qquad [Nm] \qquad (3.16c)$$

$$\tau_d\dot{T}_{drv} = -T_{drv} + u_d \qquad [Nm] \qquad (3.16d)$$

The quarter car model consists of an equation of motion (3.16a) where m is 1/4 of the vehicle mass, the wheel slip dynamics (3.16b), the wheel rotational dynamics (3.16c), and the dynamics of the dc-motor (3.16d). For simplicity reasons, the vertical wheel load F_z is assumed constant and only the longitudinal motion of the wheel is considered. $F(\kappa)$ is the pure longitudinal tyre force and v the longitudinal velocity. ω represents the wheel rotational velocity, T_{drv} the distributed torque to the wheel rim and u_d is the accelerating (or braking) input torque. The parameter $\sigma(\kappa)$ is the tyre relaxation length which is actually dependent on the level of induced wheel slip. The dynamics of the dc-motor are modelled as a first order lag system in which the time-constant τ_d represents the inertia of the dc-motor, i_{drv} is the gear ratio. The dynamics of the dc-motor cannot be neglected because they have the same order of magnitude as the desired bandwidth of the controlled system. For the friction model, the rolling resistance of the tyre and the friction present in the dc-motor and gearbox are both modelled as a constant viscous friction B_w which is proportional to the wheel rotational velocity ω. No other type of friction is considered in this model. The quarter car model parameters are chosen so as to represent the dynamic behavior of the ATS/AGV as close as possible and are listed in table 3.1.
The frequency response characteristics of the linearized quarter car model are given in appendix D. It can be concluded that the system dynamics are highly dependent on the velocity v and the tyre relaxation length σ. For higher velocities the drive actuator shows a reasonable damped behavior. However, when the velocity is near zero the system shows a weak damped behavior. The same holds for the bandwidth of the uncontrolled system, which decreases at higher velocities and/or larger relaxation length values. It is clear that for the non-linear system these parameters are time-varying and therefore cause a complex non-linear multivariable behavior which is rather difficult to analyse.
Note that besides the non-linear dynamics of the system, the tyre/road-friction force F acts as a disturbance on the system dynamics (see also (3.16c)). Because of it, the lower frequent gain in the Bode plot of the tyre force is significantly reduced. Also, the poles of the system get an increasing imaginary part, which implies that the drive actuator dynamics will become less damped. In the design of the drive servo controller in section 6.1, the disturbance force F will be compensated for by a feedforward implementation, and thereby improving the response behavior of the servo controlled drive actuator.

The steer actuator

Similar to the analysis of the quarter car model, the dynamics of the steer actuator are studied. The steer actuator controls the angle of the wheel in the horizontal plane. Naturally, by regulating the steer angle of the wheel one controls the lateral tyre/road friction force induced by the lateral slip of the wheel.

$$\alpha \;=\; \tan(\delta - \delta_{ideal}) \quad \text{for} \quad \nu_{x,w} > 0 \qquad (3.17)$$

parameter	value
m	$122Kg$
J_w	$0.36Kgm^2$
B_w	$0.57Nms/rad$
i_{drv}	5
τ_d	$5.5ms$
R_e	$0.2246m$
c_x	$77634N$
σ	$0.03 - 0.42m$
v	$0 - 50km/h$

Table 3.1: Parameters of the quarter car model

The slip angle or lateral slip coefficient α is a function of the steer angle and serves as an input to the lateral tyre force. For this reason the steer actuator is considered as a positioning system which converts a torque input u_s in to a steer angle δ. The system consist of a dc-motor, gearbox and tyre suspension. The tyre suspension is assumed to have an infinite stiffness. Combining the components into one system, called the steer actuator, the dynamics in the horizontal wheel plane are:

$$J_s\ddot{\delta} = i_{str}T_{str} \qquad [Nm] \tag{3.18a}$$

$$\tau_s\dot{T}_{str} = -T_{str} + u_s \qquad [Nm] \tag{3.18b}$$

with J_s the system's inertia, i_{str} the gearbox ratio and T_{str} the torque output of the dc-motor. The friction present in the dc-motor and gearbox is also neglected. The dynamics of the dc-motor are represented as a first-order lag system with time constant τ_s; u_s is the system input. The main difference with the drive actuator is that the tyre/road friction disturbance torque, in vehicle dynamics literature also called the self aligning moment around the vertical wheel axis, is assumed to be relatively small and therefore it is not incorporated in the dynamic model of the steer actuator. In addition, the rather large gear ratio i_{str} reduces the effect of the self aligning moment on the disturbance of the steer torque T_{str}. The used parameter values are summarized in tabel 3.2.

parameter	value
J_s	$2.30kgm^2$
i_{str}	59
τ_s	$5.7ms$

Table 3.2: Parameters of the steer actuator

3.2 The two-track dynamic vehicle model

The two-track model describes the vehicle body dynamics in the horizontal plane using three degrees of freedom, i.e. the displacements in the longitudinal and the lateral direction, and the rotation around the vertical z-axis (yaw). As an exception to this, also the distribution of the gravitational force between the front, rear, left and right wheels as a function of the longitudinal and lateral acceleration is accounted for. The two-track model forms an extension to the well known one-track model, in literature also referred to as the bicycle-model.
The dynamics in the model are derived from an existing simulation model library developed by TNO Automotive, called ATS/CAR [2]. The two-track model consists of the minimum required dynamics for an approximation of the dynamic behavior of the ATS/AGV up to extreme performance conditions, e.g. a maximum level of tyre/road friction. At the time of development, the ATS/CAR model library was experimentally validated with the ATS/AGV. From literature, it is concluded that in order to be able to deal with the wheel slip, one has to consider the force/slip-characteristics of the tyre. As a consequence, the equations of motion of the vehicle, based on force and momentum equilibria, are considered. Also, the drive actuator dynamics and the steer actuator dynamics, discussed in section 3.1.3, are incorporated in the two-track dynamic vehicle model. Finally, an assessment will be made of the influence of the estimated vertical wheel load. The quality of the vehicle model greatly depends on the validity of the tyre model and the validity of some requirements on the vehicle's operational environment.

The main features of this model are:

1. With the exception of the estimated wheel load transfer, the complexity of the model is limited to motions in the horizontal plane.

2. Because of the desired manoeuvrability of the ATS/AGV, the four wheel steer and four wheel drive configuration has to be considered. Together with the wheel load transfer estimation this requires the use of a two-track vehicle model. In this case, the existence of just one instantaneous center of rotation for the center of gravity of the vehicle, as used for common road vehicles, cannot be guaranteed.

3. The behavior of the tyres is assumed nonlinear, according to the force/slip-characteristics presented in section 3.1.2.

4. It is assumed that the vehicle travels over a perfectly flat road surface with a homogeneous tyre/road-friction coefficient.

The various quantities of interest for the modelling are depicted in figure 3.6. The center of gravity moves with speed v over the followed path where v_x and v_y are its components in longitudinal and lateral vehicle direction, respectively. All four wheels are located at equal distances from the vehicle's center of gravity. Characteristic dimensions are the distance from center of gravity to the two axles denoted as L_F and L_R for the front and rear axle and axle width S_F and S_R, respectively. The angle between the fixed axes of the posture coordinate system and the vehicle is the yaw angle ψ. The angle between the vehicle longitudinal axis and the direction of motion

is called the sideslip angle β. The steering angles are denoted as δ_{ij}, with the subindex $i = 1, 2$ representing the front and rear axle, respectively, and $j = L, R$ the left and right side of the vehicle, respectively. The resulting forces and moment working in the center of gravity are assumed to result exclusively from the longitudinal and lateral friction forces between the tyres and the road, $F_{x,ij}$ and $F_{y,ij}$, respectively. Note, that the angle between the wheel corner velocity ν_{1L} and the longitudinal wheel plane velocity $\nu_{x,w,1L}$ results in a lateral slip value α_{1L}. The same holds for the other wheels. External forces, such as forces due to aerodynamics, are neglected.

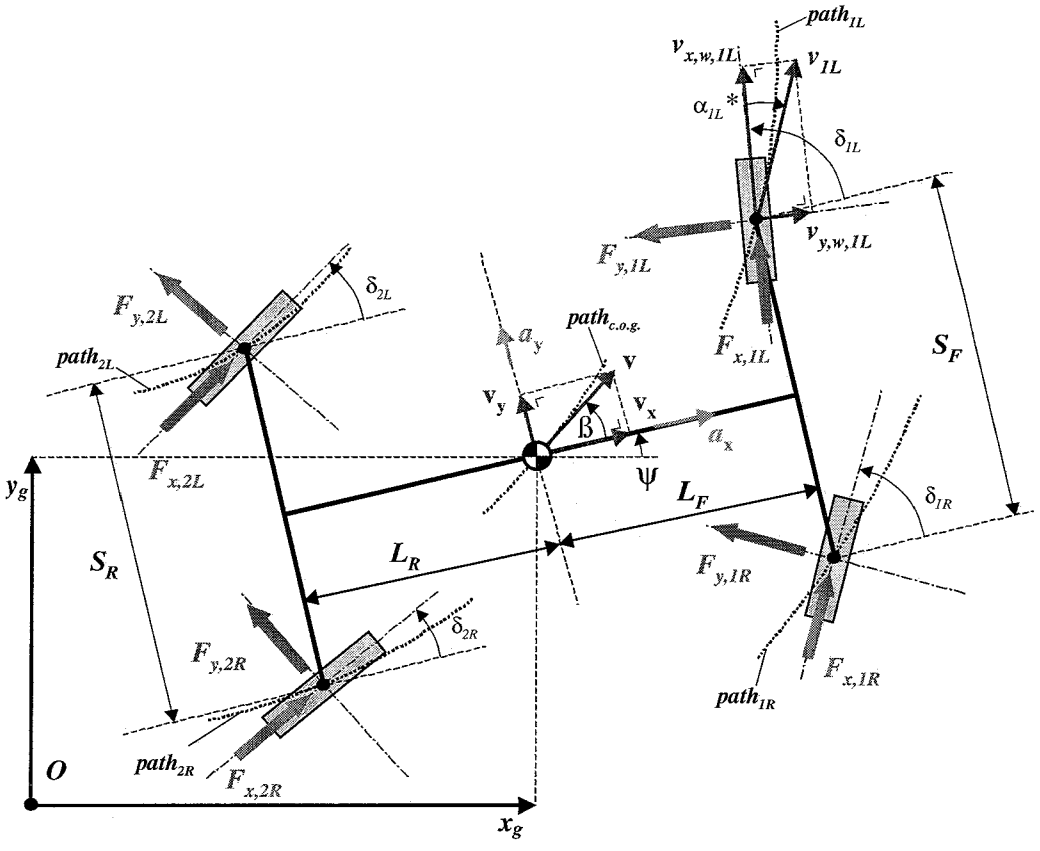

Figure 3.6: The two-track vehicle model

3.2.1 Equations of motion

With this information, the complete non-linear vehicle model consisting of the vehicle planar equations of motion, the tyre force/slip model, the drive actuator dynamics and the steer actuator dynamics, can be written as

$$\dot{\mathrm{x}}_1(t) = \mathrm{f}_1(\mathrm{x}_1(t), \mathrm{x}_2(t)) \tag{3.19}$$

$$\dot{\mathrm{x}}_2(t) = \mathrm{f}_2(\mathrm{x}_1(t), \mathrm{x}_2(t)) + \mathrm{B}\mathrm{u}(t) \tag{3.20}$$

with input $\mathrm{u}(t) = [\mathrm{u}_d(t)\ \mathrm{u}_s(t)]^T$ and the state vectors $\mathrm{x}_1(t)$ and $\mathrm{x}_2(t)$, which describe the vehicle body movement and the actuator dynamics for steering and driving, respectively. From now on, the time element t is omitted from the notation.

$$\mathrm{x}_1 = \left[v_x\ v_y\ \psi\ \dot{\psi}\right]^T \tag{3.21}$$

$$\mathrm{x}_2 = [\kappa_{ij}\ \alpha_{ij}\ \omega_{ij}\ \delta_{ij}\ T_{drv,ij}\ T_{str,ij}]^T \tag{3.22}$$

$$\mathrm{u}_d = [u_{d,ij}]^T \tag{3.23}$$

$$\mathrm{u}_s = [u_{s,ij}]^T \tag{3.24}$$

and

$$\mathrm{f}_1 = \begin{bmatrix} x_{14}x_{16} + \sum F_{long}(\mathrm{x}_1, \mathrm{x}_2, F_{z,ij})/m \\ -x_{12}x_{16} + \sum F_{lat}(\mathrm{x}_1, \mathrm{x}_2, F_{z,ij})/m \\ x_{16} \\ M(\mathrm{x}_1, \mathrm{x}_2, F_{z,ij})/I_z \end{bmatrix} \tag{3.25}$$

$$\mathrm{f}_2 = \begin{bmatrix} \frac{1}{\sigma}[-|\nu_{x,w,ij}|\kappa_{ij} + R_e\omega_{ij} - \nu_{x,w,ij}] \\ \frac{1}{\sigma}[-|\nu_{x,w,ij}|\alpha_{ij} + \nu_{y,w,ij}] \\ \frac{1}{J_w}[-R_eF_{x,ij}(\kappa_{ij}, \alpha_{ij}, F_{z,ij}) + i_{drv}T_{drv,ij}] \\ \frac{1}{J_s}[i_{str}T_{str,ij}] \\ \frac{1}{\tau_d}[-T_{drv,ij}] \\ \frac{1}{\tau_s}[-T_{str,ij}] \end{bmatrix} \tag{3.26}$$

$$\mathrm{B} = \begin{bmatrix} 0 & 0 \\ 0 & 0 \\ 0 & 0 \\ 0 & 0 \\ \frac{1}{\tau_d} & 0 \\ 0 & \frac{1}{\tau_s} \end{bmatrix} \tag{3.27}$$

where $\sum F_{long}$ and $\sum F_{lat}$ represent the force equilibrium equations in longitudinal and lateral direction, respectively. And M the moment equilibrium around the vehicle's center of gravity. m is the vehicle mass and I_z the vehicle inertia around the vertical axis in the center of gravity. Detailed equations for the force and momentum equilibria can be found in appendix E. $F_{x,ij}$ are the combined longitudinal tyre forces which do not only depend on κ_{ij} or α_{ij}, but also on the vertical wheel load estimates $F_{z,ij}$. These vertical wheel load estimates $F_{z,ij}$ depend on the measured longitudinal and lateral acceleration in the center of gravity and are further discussed in appendix F. The equations of motion are considered for the vertical and the horizontal wheel plane, which describe the drive and steer dynamics, respectively. These actuator dynamics,

discussed in the previous section, are described by the non-linear function f_2. $\nu_{x,w,ij}$ and $\nu_{y,w,ij}$ are the longitudinal and lateral wheel plane velocities.
Furthermore, it can be seen that compared with the number of independent state variables x_1 in the vehicle model there are a redundant number of (torque) actuator inputs from which four for steering u_s and four for driving u_d.

3.3 Summary

In this chapter, all necessary dynamics for describing the vehicle behavior up to extreme performance conditions are discussed. The fundamental vehicle components, like for example the tyres or the drive and steer actuators, are discussed first. The drive actuator in combination with the pure longitudinal tyre model is analyzed in more detail by linearizing a quarter car model. Together with the estimated vertical wheel loads, the two-track dynamic vehicle model will be used as a basis for the control design process addressed in the next chapters.

Chapter 4

Motion control problem

In this chapter, the motion control problem is formulated for the overactuated vehicle. While controlling the four wheeled vehicle there typically exists more than one allowable actuator configuration for the trajectory tracking. The main difficulty in controlling the overactuated vehicle is when and how to use which actuator in the system's motion. The transformation of the reference trajectory and derivatives into a corresponding 'optimal' actuator input combination, which satisfies arbitrarily chosen performance criteria, is denoted as the Dynamic Inverse Problem.

The dynamic inverse problem will be discussed in more detail in section 4.1. The control model, which contains the considered dynamics for the inverse problem, is discussed in section 4.2.

4.1 The dynamic inverse problem

Before going into any details about the inverse problem, the conceptual principle of the proposed motion control design is explained first. In this project, the tyre is regarded as a two-dimensional force generator in the horizontal plane. Its longitudinal and lateral tyre force components, $F_{x,ij}$ and $F_{y,ij}$ respectively, are suggested for the motion control of the vehicle. Figure 4.1 illustrates the force components at each wheel corner. The desired resultant forces $F_{x,cog}$, $F_{y,cog}$ and momentum $M_{z,cog}$ in the center of gravity of the vehicle are derived from the 2nd order derivatives of the reference trajectory, given the vehicle's mass m and inertia I_z. Note that by adequate steering and driving, the longitudinal and lateral tyre force components for each wheel can be controlled independently. As a consequence of this (overactuated) control freedom, the motion of the vehicle can be controlled by solving the force and momentum equilibrium equations, which are formed by equalizing the reference forces $F_{x,cog}$, $F_{y,cog}$ and reference momentum $M_{z,cog}$, and the tyre force components.

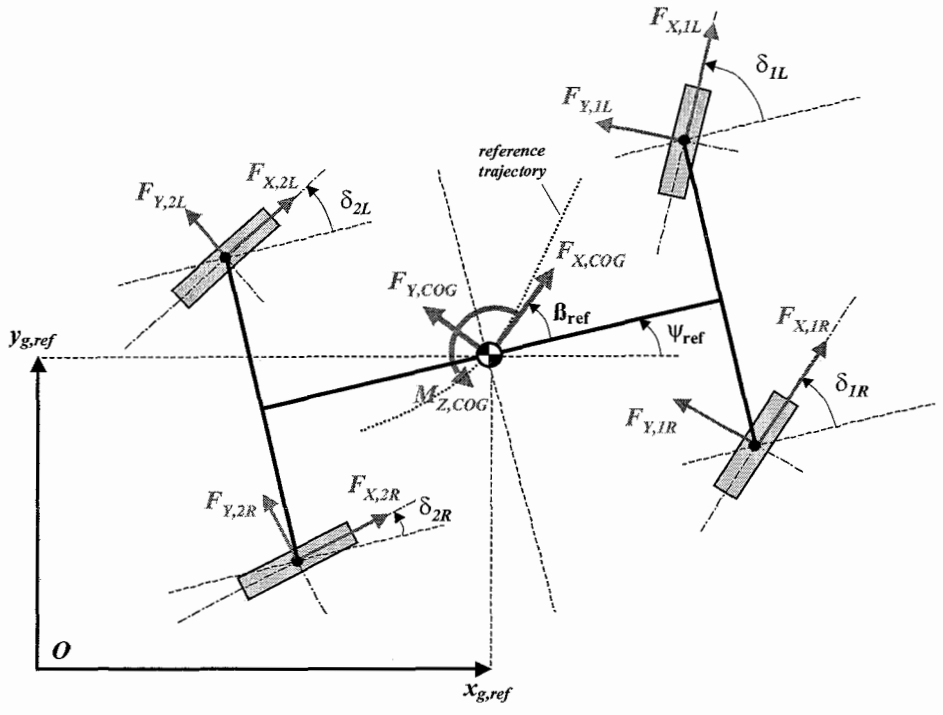

Figure 4.1: The two-track vehicle model with the considered force vectors.

Assume that the force and momentum equilibrium equations of the vehicle body, as suggested in the previous section, are described by a non-linear and non-affine dynamic model, called the control model.

$$\dot{\mathrm{p}}(t) = \mathrm{f}\left(\mathrm{p}(t)\,,\, \mathrm{z}(t)\right) \tag{4.1}$$

with state vector p and input vector z. Given the reference vector $\mathrm{p}_{ref}(t)$ and its derivative $\dot{\mathrm{p}}_{ref}(t)$, the dynamic inverse problem is then defined as

$$\text{find a } \mathrm{z}_{ref}(t) \text{ such that } \quad \dot{\mathrm{p}}_{ref}(t) = \mathrm{f}\left(\mathrm{p}_{ref}(t)\,,\, \mathrm{z}_{ref}(t)\right) \tag{4.2}$$

A detailed description of the control model and the input variables $\mathrm{z}_{ref}(t)$ will be given in section 4.2. The difficulty in obtaining a solution to the dynamic inverse problem is that the model is non-linear and non-affine. The following points of interest are to be considered:

- The model (4.1) is non-linear with respect to the states and the inputs, therefore an iterative solution method has to be sought.
- Multiple solutions $\mathrm{z}_{ref}(t)$ exist due to the non-linear nature of the model (4.1) and the redundant number of inputs.
- Extra (performance) constraint equations will have to be formulated in order to deal with the redundant number of inputs $\mathrm{z}_{ref}(t)$.

- The solutions $z_{ref}(t)$, which are infeasible with respect to the vehicle dynamics, are to be avoided.
- A certain degree of smoothness is required in the obtained solution $z_{ref}(t)$, since no actuator dynamics are considered in the dynamic inverse problem.

Optimality with respect to the obtained solution to the dynamic inverse problem is reached when the solution is feasible with respect to the vehicle dynamics. An important factor with respect to this feasibility forms the non-linear saturating tyre force. Tyre force saturation or excessive wheel slip can lead to a decreased tracking performance or even instability. In the motion control design of the vehicle it is therefore suggested to take the saturation effect of the tyre force into account. This is done by substituting the tyre force components $F_{x,ij}$ and $F_{y,ij}$ in the control model with the steady-state force/slip-characteristics of pacejka [12]. This empirical tyre model describes the tyre force as a function of the longitudinal and lateral wheel slip. In this way, wheel slip can be accounted for in a feedforward manner.

4.2 Control model

In this section, the control model (4.1) will be discussed in more detail. The control model comprises the force and momentum equilibrium equations of the vehicle body, actuator dynamics are not considered in the dynamic inverse problem.
In the control requirements it was stated that the vehicle orientation angle $\psi(t)$ should be independently controllable from the trajectory to be followed. In other words, the orientation of the vehicle does not have to be tangent to the trajectory, which is approximately the case for many common road vehicles. Since the orientation of the wheels are most of the time in the direction of the reference trajectory, it is then convenient to introduce a new coordinate system $[p_1 \;\; p_2 \;\; p_3]^T$, which has its origin fixed in the center of gravity of the vehicle and the direction p_1 tangent to the reference trajectory. The direction p_2 is always perpendicular to the reference trajectory or p_1; p_3 is taken equivalent to the vehicle orientation angle ψ, see figure 4.2. This new coordinate system will be referred to as operational space, in which θ is the angle between the axis p_1 and the axis X_g of the global absolute world.

$$\theta(t) = atan\left(\frac{\dot{y}_g(t)}{\dot{x}_g(t)}\right) \tag{4.3}$$

The operational space coordinate frame is, depending on the trajectory of the center of gravity of the vehicle, a constantly rotating coordinate frame. Therefore, all transformations between the global cartesian coordinates $[x_g \;\; y_g]^T$ and the operational space coordinates $[p_1 \;\; p_2]^T$ are performed by the use of the rotation matrix $\mathrm{R}(\theta(t))$.

$$\mathrm{R}(\theta(t)) = \begin{bmatrix} \cos(\theta(t)) & \sin(\theta(t)) \\ -\sin(\theta(t)) & \cos(\theta(t)) \end{bmatrix} \tag{4.4}$$

When looking at the velocity and acceleration of the center of gravity, the following transformations hold:

$$\begin{bmatrix} v_{p1}(t) \\ v_{p2}(t) \end{bmatrix} = \mathrm{R}(\theta(t)) \begin{bmatrix} \dot{x}_g(t) \\ \dot{y}_g(t) \end{bmatrix} \tag{4.5}$$

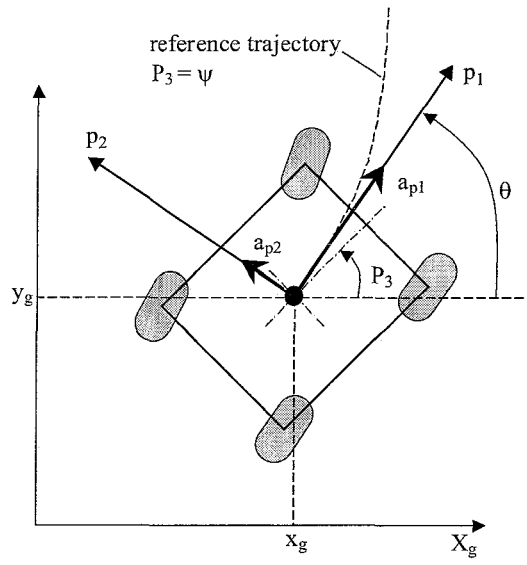

Figure 4.2: Vehicle in operational space coordinates

and

$$\begin{bmatrix} a_{p1}(t) \\ a_{p2}(t) \end{bmatrix} = \mathrm{R}(\theta(t)) \begin{bmatrix} \ddot{x}_g(t) \\ \ddot{y}_g(t) \end{bmatrix} \tag{4.6}$$

where v_{pi} are the velocity components and a_{pi} the acceleration components in operational space coordinates in the center of gravity of the vehicle. From now on, the motion of the vehicle will be described in the operational space coordinates only.

The decision which variables to incorporate into the control model input vector $\mathrm{z}(t)$ faces a design dilemma. In this project, it is chosen to use the following combination:

$$\begin{array}{llll} z_1 = \kappa_{1L} & z_2 = \kappa_{1R} & z_3 = \kappa_{2L} & z_4 = \kappa_{2R} \\ z_5 = \delta_{1L} & z_6 = \delta_{1R} & z_7 = \delta_{2L} & z_8 = \delta_{2R} \end{array}$$

The input selection is motivated by the fact that κ_{ij} and δ_{ij} are the inputs which control the tyre force magnitude and direction, respectively, considering the modelled force/slip-characteristics of the tyres. Now, the control model is written as

$$\dot{\mathrm{p}}(t) = \mathrm{f}\left(\mathrm{p}(t), \mathrm{z}(t)\right)$$

with

$$\mathrm{f} = \begin{bmatrix} \dot{\psi}(t) \cdot v_{p2}(t) + \sum F_{p1}\left(\mathrm{p}(t), \mathrm{z}(t), F_{z,ij}(t)\right)/m \\ -\dot{\psi}(t) \cdot v_{p1}(t) + \sum F_{p2}\left(\mathrm{p}(t), \mathrm{z}(t), F_{z,ij}(t)\right)/m \\ \dot{\psi}(t) \\ M_{p3}\left(\mathrm{p}(t), \mathrm{z}(t), F_{z,ij}(t)\right)/I_z \end{bmatrix} \tag{4.7}$$

and

$$\mathrm{p}(t) = \left[v_{p1}(t) \;\; v_{p2}(t) \;\; \psi(t) \;\; \dot{\psi}(t)\right]^T \tag{4.8}$$

$$\mathrm{z}(t) = \left[\kappa_{1L}(t) \;\; \kappa_{1R}(t) \;\; \kappa_{2L}(t) \;\; \kappa_{2R}(t) \;\; \delta_{1L}(t) \;\; \delta_{1R}(t) \;\; \delta_{2L}(t) \;\; \delta_{2R}(t)\right]^T \tag{4.9}$$

The vector p contains the state variables in operational space coordinates and the vector z contains the inputs. The components p_1 and p_2 are not relevant for the control design and therefore not considered. v_{p1} and v_{p2} are the longitudinal and lateral vehicle velocities, respectively, in operational space. κ_{ij} is the longitudinal slip value of the tyre and δ_{ij} the steer angle, in which the subindex ij is used to distinguish between the four tyres. $i = 1, 2$ for the front and rear axle and $j = L, R$ for the left and right side of the vehicle, respectively. From now on, time is omitted from the notations. The force equations in the control model are in longitudinal direction,

$$\sum F_{p1} = \left(\sum_{i=1,2}^{j=L,R} F_{x,ij} \cos(\delta_{ij} - \beta) - \sum_{i=1,2}^{j=L,R} F_{y,ij} \sin(\delta_{ij} - \beta) \right) \qquad [N] \qquad (4.10)$$

lateral direction.

$$\sum F_{p2} = \left(\sum_{i=1,2}^{j=L,R} F_{x,ij} \sin(\delta_{ij} - \beta) + \sum_{i=1,2}^{j=L,R} F_{y,ij} \cos(\delta_{ij} - \beta) \right) \qquad [N] \qquad (4.11)$$

The angular momentum equation is

$$\begin{aligned} M_{p3} = \; & L_F \cdot (F_{x,1L} \cdot \sin(\delta_{1L}) + F_{y,1L} \cdot \cos(\delta_{1L})) \\ & -\frac{1}{2} \cdot S_F \cdot (F_{x,1L} \cdot \cos(\delta_{1L}) - F_{y,1L} \cdot \sin(\delta_{1L})) \\ & +L_F \cdot (F_{x,1R} \cdot \sin(\delta_{1R}) + F_{y,1R} \cdot \cos(\delta_{1R})) \\ & +\frac{1}{2} \cdot S_F \cdot (F_{x,1R} \cdot \cos(\delta_{1R}) - F_{y,1R} \cdot \sin(\delta_{1R})) \\ & -L_R \cdot (F_{x,2L} \cdot \sin(\delta_{2L}) + F_{y,2L} \cdot \cos(\delta_{2L})) \\ & -\frac{1}{2} \cdot S_R \cdot (F_{x,2L} \cdot \cos(\delta_{2L}) - F_{y,2L} \cdot \sin(\delta_{2L})) \\ & -L_R \cdot (F_{x,2R} \cdot \sin(\delta_{2R}) + F_{y,2R} \cdot \cos(\delta_{2R})) \\ & +\frac{1}{2} \cdot S_R \cdot (F_{x,2R} \cdot \cos(\delta_{2R}) - F_{y,2R} \cdot \sin(\delta_{2R})) \qquad [Nm] \end{aligned} \qquad (4.12)$$

where the side slip angle β in the center of gravity of the vehicle is calculated as

$$\beta = \theta - \psi \qquad (4.13)$$

$F_{x,ij}$ and $F_{y,ij}$ are the combined longitudinal and lateral tyre forces, respectively. A more detailed description of the tyre model equations can be found in section 3.1.2. Note that the longitudinal slip value κ_{ij} and the steer angle δ_{ij} have its origin in both the longitudinal and lateral tyre force components. This clarifies the non-linearity of the control model with respect to its inputs z. The proposed solution method to the dynamic inverse problem is presented in chapter 5.

Chapter 5

Motion control design

In this chapter, a motion control design method, based on the minimization of an objective function, is proposed for the solution to the dynamic inverse problem in chapter 4. The proposed method, called the Dynamic Inverse Algorithm (DIA), will be discussed in section 5.1. Consequently, the proposed performance criterium or objective function will be discussed in section 5.2, and section 5.3 deals with the implementation details of the DIA. Finally, in section 5.4, the performance of the DIA is evaluated through open loop simulation results with the algorithm. The results are summarized in section 5.5.

5.1 The Dynamic Inverse Algorithm

In this project, the actuator redundancy in the motion control of the vehicle is dealt with through the use of numerical optimization techniques in combination with the formulation of a performance criterion. The dynamic inverse problem, defined in section 4.1, is therefore re-stated as an optimization problem.
The optimization problem is defined as:

$$\underbrace{\min}_{z_{ref}(t)} \; \mathrm{h}\left(\mathrm{p}_{ref}(t)\,,\, \dot{\mathrm{p}}_{ref}(t)\,,\, \mathrm{z}_{ref}(t)\right) \tag{5.1}$$

$\mathrm{h}\left(\mathrm{p}_{ref}(t)\,,\, \dot{\mathrm{p}}_{ref}(t)\,,\, \mathrm{z}_{ref}(t)\right)$ is a self chosen performance criterion or objective function, which has to be 'minimized' in order to solve the dynamic inverse problem. For the real-time application of the algorithm, the dynamic inverse problem has to be solved 'on-line'. This implies that the objective function has to be minimized once during each sample interval of the controlled system. The reference trajectory and higher derivatives are assumed available on a samplewise basis. Time is omitted from the notations in the text below.
Newton's method for unconstrained optimization [10] is chosen to obtain a solution to the optimization problem. Note that since the method solves an unconstrained optimization problem, the redundancy constraints have to be incorporated in the objective function h as minimization criteria. A detailed description of the composition of the objective function will be given in section 5.2. For now, it is assumed that the objective function h is available. Newton's method comprises the iterative evaluation

of the Hessian matrix $\mathrm{H_h}$ and the gradient $\nabla \mathrm{h}$ of the objective function h:

$$\mathrm{H_h}_{m,n}(\mathrm{p}_{ref}\,,\,\dot{\mathrm{p}}_{ref}\,,\,\mathrm{z}_{ref,k-1}) = \frac{\partial^2 \mathrm{h}(\mathrm{p}_{ref}\,,\,\dot{\mathrm{p}}_{ref}\,,\,\mathrm{z}_{ref,k-1})}{\partial z_{ref,m}\,\partial z_{ref,n}} \tag{5.2}$$

$$\nabla \mathrm{h}_m(\mathrm{p}_{ref}\,,\,\dot{\mathrm{p}}_{ref}\,,\,\mathrm{z}_{ref,k-1}) = \frac{\partial \mathrm{h}(\mathrm{p}_{ref}\,,\,\dot{\mathrm{p}}_{ref}\,,\,\mathrm{z}_{ref,k-1})}{\partial z_{ref,m}} \tag{5.3}$$

with $m = 1, 2, ..., 8$ and $n = 1, 2, ..., 8$. The index k represents the iteration number of the optimization process. The direction and magnitude of the stepsize s_k is then calculated according to:

$$\mathrm{H_h} \cdot \mathrm{s}_k + \nabla \mathrm{h} = 0 \tag{5.4}$$

$$\Rightarrow \quad \mathrm{s}_k = -\mathrm{H_h^{-1}}(\mathrm{p}_{ref}\,,\,\dot{\mathrm{p}}_{ref}\,,\,\mathrm{z}_{ref,k-1})\nabla \mathrm{h}(\mathrm{p}_{ref}\,,\,\dot{\mathrm{p}}_{ref}\,,\,\mathrm{z}_{ref,k-1}) \tag{5.5}$$

$$\Rightarrow \quad \mathrm{z}_{ref,k} = \mathrm{z}_{ref,k-1} + \mathrm{s}_k \tag{5.6}$$

The computational effort of the method depends primarily on the dimensions of the Hessian matrix and gradient vector, since they are used for obtaining the step size s_k at each iteration. A pseudo code example of the iterative optimization process or dynamic inverse algorithm is listed below:

$k = 0$
$z_{ref,0}$ = initial guess
while $\sim$ conv
  $k = k + 1$
  Solve $H_\mathrm{h}\,(z_{ref,k-1}) \cdot s_k = -\nabla \mathrm{h}\,(z_{ref,k-1})$ for s_k
  $z_{ref,k} = z_{ref,k-1} + s_k$
  conv $= \left| \frac{z_{ref,k} - z_{ref,k-1}}{z_{ref,k-1}} \right| \leq tolerance$
end

The solution obtained for the previous minimization of the objective function is used as an initial guess for $\mathrm{z}_{ref,0}$ in order to improve the convergence of the optimization. In general, the convergence criterium conv is free to choose, depending on the desired accuracy of the solution or the number of allowable iteration steps in the minimization of the objective function.

5.2 Objective function

The criteria in the objective function are entirely based on reference values, this in order to emphasize a feedforward implementation of the algorithm. Where the control model in section 4.2 was defined in order to give a formal description of the considered dynamics in the inverse problem. In the design of the objective function h , only the force and momentum equilibrium equations discussed in the control model are actually used as a system representation. For that purpose, the reference accelerations in the vehicle longitudinal direction $a_{p1,ref}$, lateral direction $a_{p2,ref}$ and yaw direction $\ddot{\psi}_{ref}$, are introduced. They are derived from the 2nd derivatives of the reference trajectory in global space coordinates:

$$\begin{bmatrix} a_{p1,ref} \\ a_{p2,ref} \\ \ddot{\psi}_{ref} \end{bmatrix} = \begin{bmatrix} \cos(\theta_{ref}) & \sin(\theta_{ref}) & 0 \\ -\sin(\theta_{ref}) & \cos(\theta_{ref}) & 0 \\ 0 & 0 & 1 \end{bmatrix} \cdot \begin{bmatrix} \ddot{x}_{g,ref} \\ \ddot{y}_{g,ref} \\ \ddot{\psi}_{ref} \end{bmatrix} \tag{5.7}$$

with

$$\theta_{ref} = atan\left(\frac{\dot{y}_{g,ref}}{\dot{x}_{g,ref}}\right) \tag{5.8}$$

The objective function h consists of the model errors e_{p1}, e_{p2} and e_{p3}, and some additional minimization criteria (constraints) as a function of the optimization variables z_{ref}. The additional criteria are formulated in order to deal with the redundant number of input variables z_{ref} and to improve the convergence of the optimization, while the model errors imply the solution to the dynamic inverse problem. After an elaborate study of suitable minimization criteria or constraints in the objective function and simulations with the algorithm, the following minimization criteria are finally chosen for the composition of the objective function.

5.2.1 Model error

The model errors are considered to be the most important criteria in the objective function and express the overall quality of the inverse solution z_{ref}. They represent the error between the desired reference acceleration and the model acceleration, based on the optimization variables z_{ref}.

$$e_{p1} = a_{p1,ref} - \sum F_{p1}\left(p_{ref}, z_{ref}, F_{z,ij}\right)/m \quad [m/s^2] \tag{5.9}$$

$$e_{p2} = a_{p2,ref} - \sum F_{p2}\left(p_{ref}, z_{ref}, F_{z,ij}\right)/m \quad [m/s^2] \tag{5.10}$$

$$e_{p3} = \ddot{\psi}_{ref} - \sum M_{p3}\left(p_{ref}, z_{ref}, F_{z,ij}\right)/I_z \quad [rad/s^2] \tag{5.11}$$

The equations (5.9) till (5.11) represent the errors of the force and momentum equilibrium equations in the longitudinal, lateral and yaw direction of the vehicle, respectively. See appendix G for a more detailed description. Note that the model error e_{pi} either has an unit $[m/s^2]$ or $[rad/s^2]$, and therefore suggests the control of the vehicle on an acceleration level.

5.2.2 Weight transfer criteria

The weight transfer functions in the transmission of the tyre forces $F_{x,ij}$ and $F_{y,ij}$ over each wheel are criteria of secondary importance, but nevertheless crucial for an optimal performance of the vehicle and the dynamic inverse algorithm. In terms of vehicle dynamics the weight transfer functions imply nothing else than that the wheel with the largest vertical load $F_{z,ij}$ should transfer the biggest tyre force. For the two-track model the longitudinal, lateral and diagonal weight transfer is considered. The ideal weight transfer functions expressed in terms of the pure longitudinal tyre force $F_{x,0,ij}$ and the pure lateral tyre force $F_{y,0,ij}$ are

$$\frac{|F_{x,0,1R}|}{F_{z1R}} = \frac{|F_{x,0,1L}|}{F_{z1L}} \quad \Rightarrow \quad |F_{x,norm,0,1R}| = |F_{x,norm,0,1L}|$$

$$\frac{|F_{x,0,2L}|}{F_{z2L}} = \frac{|F_{x,0,1L}|}{F_{z1L}} \quad \Rightarrow \quad |F_{x,norm,0,2L}| = |F_{x,norm,0,1L}|$$

$$\frac{|F_{x,0,2R}|}{F_{z2R}} = \frac{|F_{x,0,1L}|}{F_{z1L}} \quad \Rightarrow \quad |F_{x,norm,0,2R}| = |F_{x,norm,0,1L}|$$

$$\frac{|F_{y,0,1R}|}{F_{z1R}} = \frac{|F_{y,0,1L}|}{F_{z1L}} \quad \Rightarrow \quad |F_{y,norm,0,1R}| = |F_{y,norm,0,1L}|$$

$$\frac{|F_{y,0,2L}|}{F_{z2L}} = \frac{|F_{y,0,1L}|}{F_{z1L}} \quad \Rightarrow \quad |F_{y,norm,0,2L}| = |F_{y,norm,0,1L}|$$

$$\frac{|F_{y,0,2R}|}{F_{z2R}} = \frac{|F_{y,0,1L}|}{F_{z1L}} \quad \Rightarrow \quad |F_{y,norm,0,2R}| = |F_{y,norm,0,1L}|$$

The tyre force components with the subscript $_{norm}$ are normalized with respect to the vertical wheel load $F_{z,ij}$. Note that only normalized pure ($subscript : ..._0$) tyre forces are used, i.e. non-combined slip. The pure normalized tyre force equations discussed above can be simplified even further, consider for example:

$$\begin{aligned} &|F_{x,norm,0,1R}| = |F_{x,norm,0,1L}| \\ &|D_{x,norm} sin(C_{x,norm} \arctan(B_{x,norm} \cdot \kappa_{1R}))| = |D_{x,norm} sin(C_{x,norm} \arctan(B_{x,norm} \cdot \kappa_{1L}))| \\ &|\kappa_{1R}| = |\kappa_{1L}| \end{aligned} \tag{5.12}$$

The same reasoning holds for the normalized pure lateral tyre force components $F_{y,norm,0,ij}$. In general, the use of absolute values in the minimization criteria is not preferable because of their non-smoothness. Derived from the ideal weight transfer functions above and the simplification in (5.12), it is chosen to use the functions g_1,g_2,g_3 and g_4,g_5,g_6 for the longitudinal and lateral tyre force components, respectively:

$$\begin{aligned} g_1 &= \kappa_{ref,1R} - \kappa_{ref,1L} \\ g_2 &= \kappa_{ref,2L} - \kappa_{ref,1L} \\ g_3 &= \kappa_{ref,2R} - \kappa_{ref,1L} \end{aligned} \tag{5.13}$$

$$\begin{aligned} g_4 &= \alpha_{ref,1R} - \alpha_{ref,1L} \\ &= (\delta_{ref,1R} - \delta_{ideal,1R}) - (\delta_{ref,1L} - \delta_{ideal,1L}) \\ g_5 &= \alpha_{ref,2L} - \alpha_{ref,1L} \\ &= (\delta_{ref,2L} - \delta_{ideal,2L}) - (\delta_{ref,1L} - \delta_{ideal,1L}) \\ g_6 &= \alpha_{ref,2R} - \alpha_{ref,1L} \\ &= (\delta_{ref,2R} - \delta_{ideal,2R}) - (\delta_{ref,1L} - \delta_{ideal,1L}) \end{aligned} \tag{5.14}$$

The functions g_i are minimized with respect to $\kappa_{ref,ij}$ and $\delta_{ref,ij}$ which are elements of the vector z_{ref}. Note that all optimization variables z_{ref} are incorporated into the minimization criteria g_i. Another reason for using these weight transfer functions is that they contribute to a feasible solution to the dynamics inverse problem. To give an example, one could accelerate a vehicle in longitudinal direction by generating large positive tyre forces at the front wheels and large, but in absolute values just a fraction smaller, negative tyre forces for the rear wheels. The net result would still be an accelerating vehicle, but nevertheless undesirable because of physical reasons.
For the weight transfer minimization criteria g_i it can be concluded that they force the variables $\kappa_{ref,ij}$ and $\alpha_{ref,ij}$ to attain the same order of magnitude (not necessarily the smallest). And that at all times the variables are to keep an equal sign. For some typical vehicle manoeuvring, e.g. a lateral acceleration combined with a large instantaneous yaw acceleration, the weight transfer functions g_i are contradictory. So a compromise has to be made. In this study, it is chosen to strife for an equal sign of the wheel slip values $\kappa_{ref,ij}$ and $\alpha_{ref,ij}$, respectively.

5.2.3 Actuator effort criteria

From the force/slip-characteristics of the tyre it is known that the longitudinal and lateral tyre forces are subjected to physical limitations. Therefore, the energy usage of the actuators (tyre) is penalized by using the quadratic-norm of the longitudinal and lateral slip values, respectively. This gives for the longitudinal direction of the wheel, in which $\kappa_{ref,ij}$ is the relevant variable,

$$\|z_{ref,1-4}\|^2 = {\kappa_{ref,1L}}^2 + {\kappa_{ref,1R}}^2 + {\kappa_{ref,2L}}^2 + {\kappa_{ref,2R}}^2 \tag{5.15}$$

For the lateral direction of the wheel the quadratic-norm of the lateral slip values $\alpha_{ref,ij}$, which can be approximated by

$$\begin{aligned}\|z_{ref,5-8} - \delta_{ideal,ij}\|^2 = {} & (\delta_{ref,1L} - \delta_{ideal,1L})^2 + (\delta_{ref,1R} - \delta_{ideal,1R})^2 + \\ & (\delta_{ref,2L} - \delta_{ideal,2L})^2 + (\delta_{ref,2R} - \delta_{ideal,2R})^2\end{aligned} \tag{5.16}$$

will be minimized. Remind that the ideal steer angle $\delta_{ideal,ij}$ (3.17) was defined to be the steer angle at which the velocity perpendicular to the vertical wheel plane is equal to zero.

5.2.4 Actuator dynamics criteria

The derivatives of the optimization variables are also used as objective function criteria. In this way, a damped behavior and a certain smoothness of the optimization variables is achieved. The derivatives are calculated using a forward Euler approximation according to:

$$\dot{z}_{ref}(k) = \frac{z_{ref}(k) - z_{ref}(k-1)}{\Delta t} \tag{5.17}$$

Note that $z_{ref}(k-1)$ is the vector with the optimization variables obtained from the previous iterative minimization of the objective function. The suggestion that the derivatives in the objective function take the actuator dynamics into account is not true, although to some degree they penalize the 'speed of actuating'.

Combining the different minimization criteria leads to the objective function h which is then used in the optimization process to obtain the solution, z_{ref}, to the dynamic inverse problem. In short, the objective function is formulated as:

$$\begin{aligned}\mathrm{h} = {} & \|e_{p1-p3}\|^2 + \|g_{1-6}\|^2 + \|z_{ref,1-4}\|^2 + \|\dot{z}_{ref,1-8}\|^2 + \\ & \|z_{ref,5-8} - \delta_{ideal,ij}\|^2\end{aligned} \tag{5.18}$$

Weight parameters q_i ($q_i > 0; i = 1, ..., 9$) are added in order to be able to emphasize the relative importance of the different minimization criteria in the objective function, yielding the final optimization function:

$$\begin{aligned}\mathrm{h} = {} & q_1 e_{p1}^2 + q_2 e_{p2}^2 + q_3 e_{p3}^2 + q_4 ({g_1}^2 + {g_2}^2 + {g_3}^2) + q_5 ({g_4}^2 + {g_5}^2 + {g_6}^2) + \\ & q_6 ({\kappa_{ref,1L}}^2 + {\kappa_{ref,1R}}^2 + {\kappa_{ref,2L}}^2 + {\kappa_{ref,2R}}^2) + \\ & q_7 ({\dot{\kappa}_{ref,1L}}^2 + {\dot{\kappa}_{ref,1R}}^2 + {\dot{\kappa}_{ref,2L}}^2 + {\dot{\kappa}_{ref,2R}}^2) + \\ & q_8 ({\dot{\delta}_{ref,1L}}^2 + {\dot{\delta}_{ref,1R}}^2 + {\dot{\delta}_{ref,2L}}^2 + {\dot{\delta}_{ref,2R}}^2) + \\ & q_9 ((\delta_{ref,1L} - \delta_{ideal,1L})^2 + (\delta_{ref,1R} - \delta_{ideal,1R})^2 + \\ & (\delta_{ref,2L} - \delta_{ideal,2L})^2 + (\delta_{ref,2R} - \delta_{ideal,2R})^2)\end{aligned}$$

The tuning of the weights q_i requires some trial and error. Note that if some weights are chosen too large the optimization might not converge to an 'optimum' at all, so a compromise must be made. Together with the initial starting guess, the weights in the objective function are key components in the result of the optimization.

5.3 Implementation details

Having discussed the proposed solution method to the dynamic inverse problem, the implementation of the Dynamic Inverse Algorithm (DIA) will be discussed in this section. The implementation is illustrated in figure 5.1.

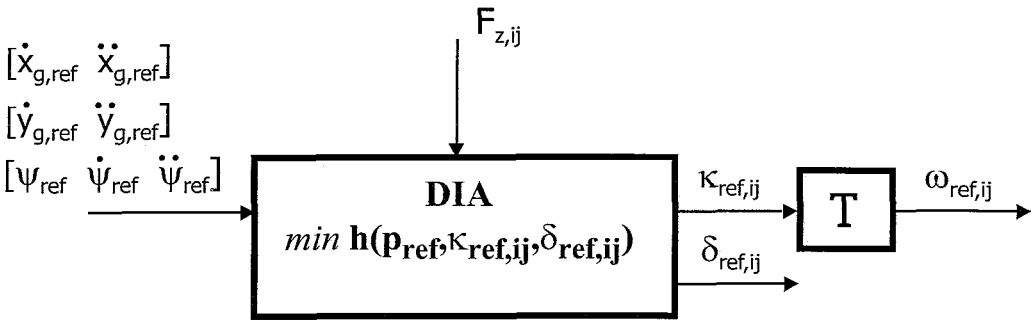

Figure 5.1: Implementation of the DIA

So what have we achieved? The figure implies that given certain reference trajectory information and a vertical wheel load estimate, the DIA provides reference values for the steerangles $\delta_{ref,ij}$, and reference values for longitudinal slip $\kappa_{ref,ij}$. However, the problem is that the DIA output $\kappa_{ref,ij}$ cannot be directly used for control purposes. A transformation is proposed, assuming that the obtained reference values are dealt with by local servo controllers.
In addition, it will be shown that the physical reference values for the servo controllers are derived from the DIA output according to a separation principle. This separation principle clarifies the distinction made between compensating for wheel slip in the motion control of the vehicle and not compensating for wheel slip (nominal control).

5.3.1 Actuator reference values

Having obtained the output z_{ref}, the reference signals for the local servo controllers, $\omega_{ref,ij}$ and $\delta_{ref,ij}$, can now be calculated. Recall that the minimization of the objective function resulted in the sample wise solution z_{ref} such that

$$z_{ref} = [\kappa_{ref,ij} \quad \delta_{ref,ij}]$$

Using the equations for calculating the steady-state slip, the following transformation is proposed for calculating the reference wheel rotational velocity

$$\begin{aligned} \omega_{ref}(\kappa_{ref}, v_{x,w,ref}) &= \omega_{nom}(1 + \Delta\omega_{slip}) \\ &= \frac{v_{x,w,ref}}{R_e}(1 + sign(v_{x,w,ref})\kappa_{ref}) \end{aligned} \tag{5.19}$$

in which R_e is the effective rolling radius of the tyre and $\nu_{x,w,ref}$ the reference longitudinal wheel velocity. The reference steer angle δ_{ref} is directly obtained from the inverse solution variables z_{ref}. Note that the reference steer angle as a function of the lateral reference slip value α_{ref} can be written as

$$\begin{aligned} \delta_{ref}(\alpha_{ref}, \delta_{ideal}) &= \delta_{nom} + \Delta\delta_{slip} \\ &= \delta_{ideal} + atan(\alpha_{ref}) \end{aligned} \tag{5.20}$$

with

$$\delta_{ideal,ij} = atan\left(\frac{\nu_{y,ref,ij}}{\nu_{x,ref,ij}}\right)$$

according to (3.17). In (5.19) and (5.20), the contribution of slip in the longitudinal and lateral direction of the wheel are represented by $\Delta\omega_{slip}$ and $\Delta\delta_{slip}$, respectively. When the wheel slip is underestimated in the modelling, the Δ_{slip} part in (5.19) and (5.20) becomes negligible small and thus only the nominal reference values are prescribed by the DIA. Any overcompensation of the wheel slip is bounded since the DIA explicitly handles the control saturation in the longitudinal and lateral wheel slip compensation, as will be shown in section 5.4. In addition, note that the Δ_{slip} part in the reference signals is relatively small compared to the nominal reference values. Based on the separation principle, it is stated that the implementation of the DIA is based on a feedforward compensation of the longitudinal and lateral wheel slip.
An assessment of the required control accuracy for the realization of the desired longitudinal slip κ_{ref} and lateral slip α_{ref} has been made. Theoretically, the minimum required numerical accuracy of the controlled slip values must be in the order of $\Delta 10^{-2}$ slip. In order to fulfill this requirement, the measured wheel rotational velocity ω_m $[rad/s]$, the measured steer angle δ_m $[rad]$ and the measured velocity $\nu_{x,w,m}$ $[m/s]$ also require a minimum accuracy of $\Delta 10^{-2}$. For this reason, (5.19) and (5.20) are purely based on reference signals derived from the reference trajectory in order to achieve a tracking of the vehicle which is less sensitive for erroneous feedback information. As a consequence hereof, the magnitude of the steady-state tracking error of the servo controlled actuators must be smaller than $\Delta 10^{-2}$.

5.4 Performance evaluation

In this section, the performance of the DIA is evaluated through simulation results of some typical vehicle manoeuvring. The output of the algorithm, which consists of the reference longitudinal slip values $\kappa_{ref,ij}(t)$ and reference steer angles $\delta_{ref,ij}(t)$, is calculated together with the control model errors $e_{p1}(t)$, $e_{p2}(t)$ and $e_{p3}(t)$ in (5.9) till (5.11). Only the output of the DIA is considered, no vehicle model is used for the performance evaluation.
A rule of thumb for the tuning of the weight parameters is that the tuning should be conducted on extreme trajectories, such as for example a (non-smooth) lane change manoeuvre, making sure that all degrees of freedom are used in the prescribed motion of the vehicle. The quality of the tuning is assessed by the size of the model errors e_{p1}, e_{p2} and e_{p3}, and the feasibility of $\kappa_{ref,ij}(t)$ and $\delta_{ref,ij}(t)$ with respect to the actuator dynamics. The optimal tuning of the weight parameters in the objective

function involves a trade-off between the generality and the quality of the tuned objective function. After a time consuming tuning of the weight parameters in the objective function, the set in tabel 5.1 is finally used.

q_1	q_2	q_3	q_4	q_5	q_6	q_7	q_8	q_9
$\frac{2*487}{m}$	$\frac{10*487}{m}$	$\frac{9*305}{I_z}$	$1\,10^{10}$	$1\,10^{8}$	$5\,10^{7}$	$5\,10^{4}$	$1\,10^{5}$	$5\,10^{7}$

Table 5.1: Tuned weight parameters for the objective function; $m = 487\ [kg]$ and $I_z = 305\ [Kgm^2]$

In order to get a better insight into the obtained weight parameter values, the weights are normalized such that each criterion in the objective function has a unit $[N]$. This results in the following normalized parameter set:

$q_{1,norm}$	$q_{2,norm}$	$q_{3,norm}$	$q_{4,norm}$	$q_{5,norm}$	$q_{6,norm}$	$q_{7,norm}$	$q_{8,norm}$	$q_{9,norm}$
1.4	3.2	1.9	20.5	2.1	1.5	18.4	26.0	1.5

Table 5.2: Normalized weight parameters for the objective function.

From tabel 5.2 it can be concluded that the weights $q_{4,norm}$, $q_{7,norm}$ and $q_{8,norm}$ are approximately a factor 10 larger than the other weights. There are two main explanations for this observed effect:

- For optimal traction, the longitudinal tyre force components have to be forced to attain an equal sign and an equal magnitude. These requirements are implied by the weight transfer criteria in the objective function, see also section 5.2.2.
- The objective function in the dynamic inverse algorithm has to be able to deal (to a certain extent) with non-smooth reference trajectories, which can destabilize the optimization process. The actuator dynamics criteria in section 5.2.4 are used for that purpose.

5.4.1 Steady-state slip behavior

First, the reference longitudinal slip values $\kappa_{ref,ij}(t)$ are examined during pure longitudinal reference accelerations $a_{p1,ref}(t)$ ($a_{p2,ref}(t) = \ddot{\psi}_{ref}(t) = 0$). The acceleration level starting in zero is gradually increased till well beyond the theoretical maximum vehicle acceleration of approximately 13 $[m/s^2]$, which is ultimately determined by the assumed force/slip-characteristic of the tyre in the DIA and the estimated vertical wheel load. In figure 5.2, the longitudinal reference slip values $\kappa_{ref,ij}(t)$, resulting from the DIA output, are plotted versus the reference longitudinal acceleration $a_{p1,ref}(t)$. It can be seen that each longitudinal reference slip value of the four wheels attains the same magnitude. This is the typical result of the longitudinal weight transfer constraints in the objective function. The nominal friction level μ_{nom} in the control

model is set to respectively 50% and 150% in order to investigate the effect of model errors in the assumed longitudinal force/slip-characteristics on the reference slip values. The 50% curve represents a lower modelled tyre stiffness, and the 150% curve represents a higher modelled tyre stiffness, compared to the nominal model. All three curves asymptotically converge to the longitudinal peak slip value $\kappa_{peak} \approx 6\%$ for increasing reference accelerations. Also, for small reference accelerations the slip curves become linear and show a close resemblance with the modelled longitudinal force/slip-characteristics in the control model. In terms of vehicle dynamics, the corresponding attained peak slip value of approximately 6 percent wheel slip would result in a maximum tyre acceleration force without excessive wheel slip. Exactly the same holds for negative slip values during decelerating or braking, since the assumed force/slip-characteristic is symmetric for positive and negative slip values.

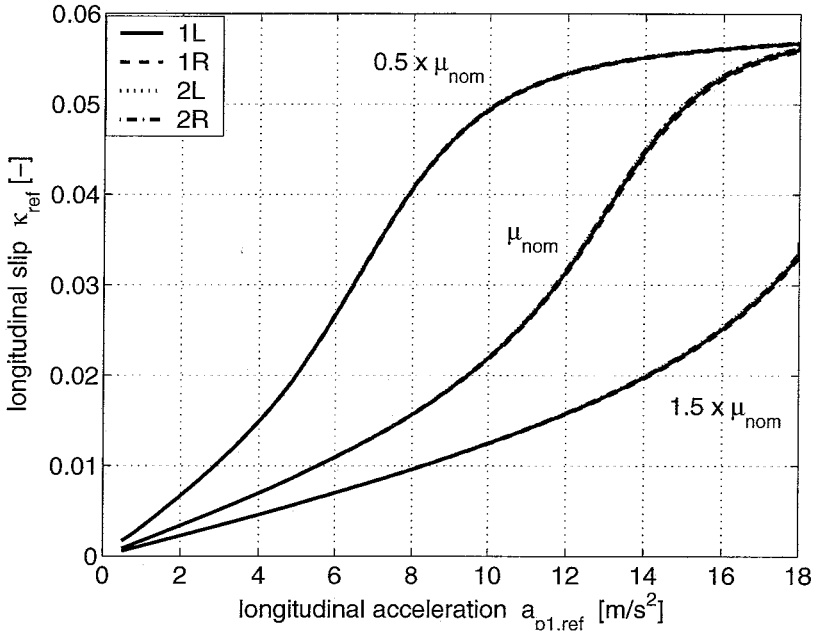

Figure 5.2: Steady-state pure longitudinal acceleration manoeuvring.

An identical behavior is observed for the lateral reference slip anlges $\alpha_{ref,ij}(t)$ during steady-state cornering. A circular reference trajectory with a radius of $R = 5m$ is followed with a gradually increasing longitudinal velocity. In figure 5.3, the reference steer angle for the front left wheel $\delta_{ref,1L}$, resulting from the DIA output, is plotted versus the reference lateral acceleration $a_{p2,ref}$. The Ackerman steer angle, also called the ideal or nominal steer angle, is illustrated by the straight horizontal line in the graph and represents the steer angle with zero lateral wheel plane velocity $v_{y,w}$. No lateral tyre force is generated while steering at this nominal angle. Any steer angle increase or decrease would directly result in a nonzero lateral slip angle and thus a lateral tyre force. Figure 5.3 therefore illustrates the ability of the DIA to compensate for centripetal forces in the center of gravity of the vehicle. Again, the three curves

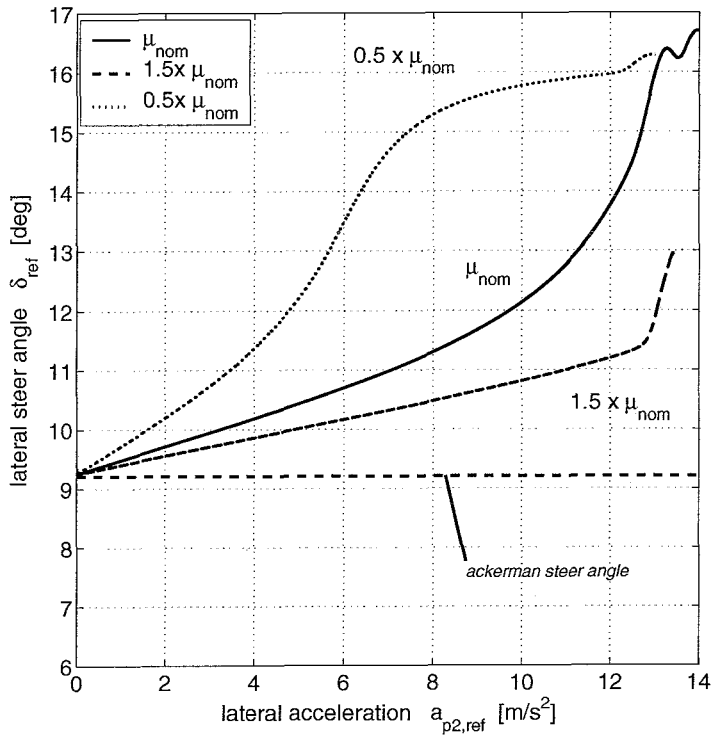

Figure 5.3: Steady-state cornering at a circular radius of $R = 5m$; the front left wheel (bottom).

asymptotically converge to the lateral peak slip angle α_{peak} of approximately 7 $[deg]$ $(= \delta_{ref,max} - \delta_{ideal})$ in accordance with the modelled lateral force/slip-characteristics in the control model. Note that in both the longitudinal and lateral direction of the tyre an underestimated friction level $(0.5 \times \mu_{nom})$ leads to a reference slip value which is chosen to heavily for small acceleration values and also leads to a faster saturation of the reference slip value. An overestimated friction level $(1.5 \times \mu_{nom})$ appears to degrade the overall slip compensation.

Figure 5.4 shows all four lateral reference slip angles $\alpha_{ref,ij}(t)$ for the same steady-state cornering manoeuvre as described by figure 5.3. Again, it can be seen that the four reference slip angles attain approximately the same magnitude which indicates the effect of the lateral weight transfer constraints in the objective function. The oscillating behavior of the reference slip values at the peak slip levels, both in longitudinal and lateral direction, is caused by the convergence of the optimization near the (local) 'minimum' of the objective function.

In general, it can be concluded that the DIA is capable of coordinating the eight actuators of the vehicle up to limit tyre adhesion conditions and thereby enables the high performance control of the vehicle. Furthermore, the algorithm explicitly handles the control saturation in the longitudinal and lateral direction of the tyre. Optimal tractive forces for the longitudinal and lateral direction of the tyre are commanded without excessive wheel slip.

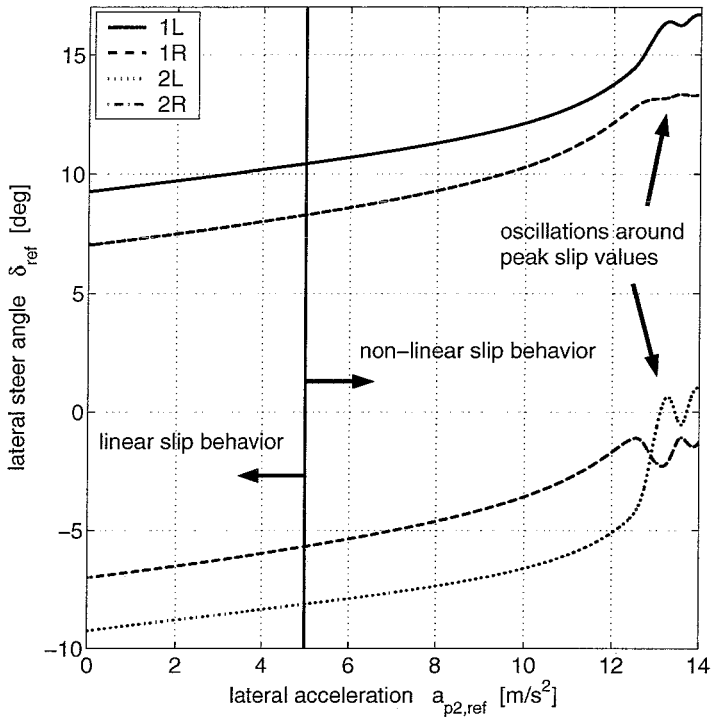

Figure 5.4: Steady-state cornering at a circular radius of $R = 5m$; nominal friction μ_{nom}.

5.4.2 A case study

Having discussed the basic behavior of the DIA in the previous section, the control model error signals $e_{p1}(t)$, $e_{p2}(t)$ and $e_{p3}(t)$, resulting from the minimization of the objective function, are examined more closely in this section. As a case study, the lane change manoeuvre is used for this purpose.

Figure 5.5 illustrates the lane change trajectory in the global coordinates x_g and y_g. During the lane change manoeuvre the vehicle moves approximately 3 meter sidewards at a constant longitudinal velocity of 22 km/h while keeping the orientation angle of the vehicle tangent to the trajectory (see arrowheads in figure). The corresponding longitudinal $a_{p1,ref}$(t), lateral $a_{p2,ref}(t)$ and yaw $\ddot{\psi}_{ref}(t)$ reference acceleration profiles are plotted in the right side of figure 5.5.

The difficulty of the lane change manoeuvre lies in the simultaneous reference accelerations for the three degrees of freedom of the vehicle. A large and non-smooth yaw acceleration profile $\ddot{\psi}_{ref}(t)$ is chosen in order to be able to emphasize the performance of the DIA. In fact, by applying a step input on the reference yaw acceleration infinite actuator accelerations are required for the instantaneous yaw motion. Since there are no actuator dynamics incorporated in the control model of the DIA, a non-smooth behavior for the DIA output signals $\kappa_{ref,ij}(t)$ and $\delta_{ref,ij}(t)$ is expected as well.

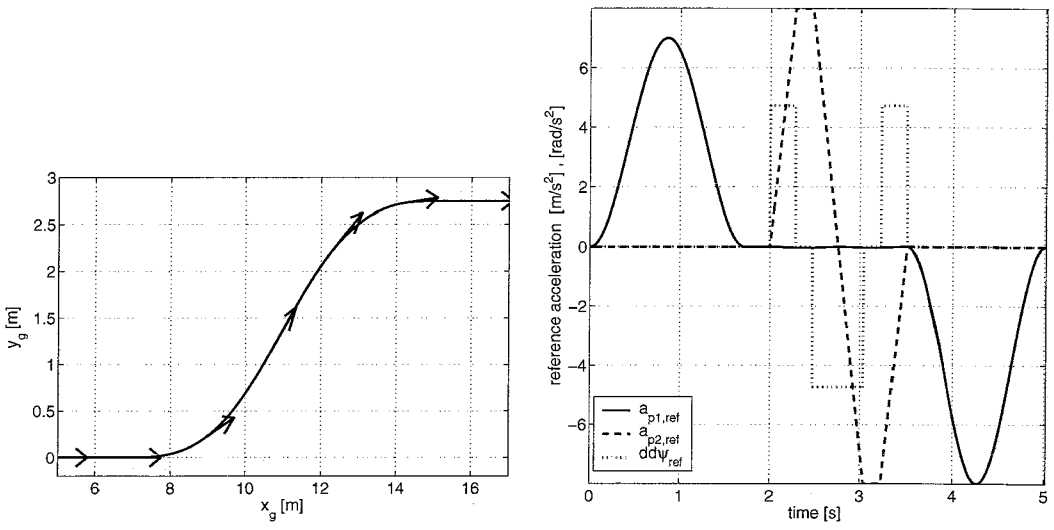

Figure 5.5: Lane change manoeuvre with a longitudinal constant velocity of 22 km/h (left). Reference acceleration profiles (right).

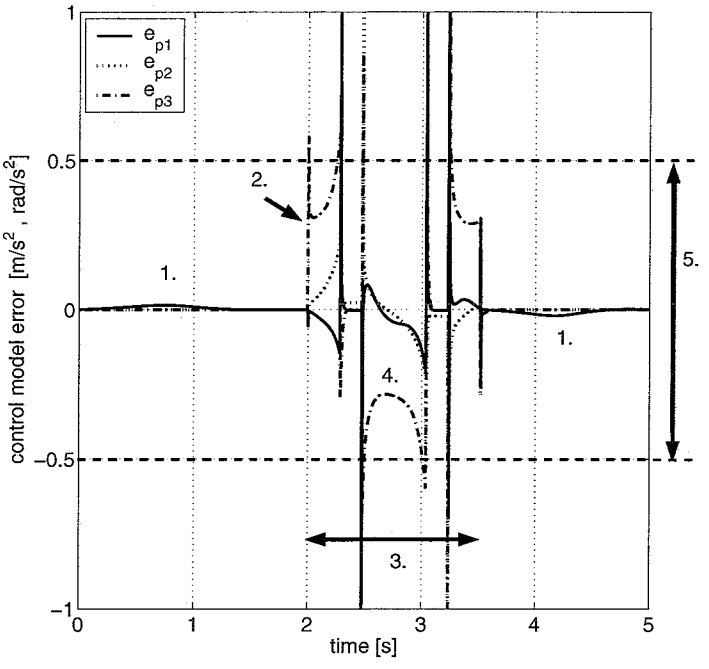

Figure 5.6: Control model error signals $e_{p1}(t)$, $e_{p2}(t)$ and $e_{p3}(t)$ for the simulated lane change manoeuvre

In figure 5.6, the control model error signals $e_{p1}(t)$, $e_{p2}(t)$ and $e_{p3}(t)$ resulting from the simulated lane change manoeuvre are plotted. The error signals represent the ability of the DIA to solve the force and momentum equilibria equations (5.9) till (5.11) in the control model given the additional constraints and weights in the objective function (5.18). The numbers in the figure represent typical observed properties of the DIA and are explained as follows:

1. The motion of the vehicle in only one directional degree of freedom, i.e. either in the longitudinal, the lateral or the yaw direction, is typically solved with an error less than 1 % of the reference acceleration, i.e. $< 0.07 m/s^2$.

2. Non-smooth solutions to the dynamic inverse problem are observed due to the neglected actuator dynamics in the control model. The weights in the objective function are tuned in such a way that the DIA solutions remain stable/feasible for reference trajectories which are to a certain extent non-smooth. This de-tuning is performed at the cost of an increase in the model error.

3. It appears that the combined manoeuvring in longitudinal, lateral and yaw direction leads to an overall increase in the model errors due to a more complex optimization problem.

4. The relative magnitudes of the three error signals primarily depend on the combination of the tuned weights q_1, q_2 and q_3. For this case study, it appears that the yaw manoeuvring has the largest model error. Partially because the lateral component of the control model error is weighted more heavily in the objective function, but probably also because of the fact that the yaw manoeuvring of the vehicle depends on both the steering and the driving (δ and κ).

5. In general, it is observed that the control model error $e_{p3}(t)$ remains smaller then 10% and the errors $e_{p1}(t)$ and $e_{p2}(t)$ even smaller than 5% of its reference values. Although these percentages are derived from just a single reference trajectory, remind that trajectories with milder reference acceleration profiles will most likely lead to smaller model errors provided that the non-smoothness in the acceleration profiles is limited!

The DIA output signals for the front right wheel, expressed as the reference longitudinal slip $\kappa_{ref,1R}(t)$ and the reference lateral slip $\alpha_{ref,1R}(t)$, are plotted in figure 5.7. Note the non-smoothness of the reference slip values between $t = 2$ and $t = 4\,[s]$ which is a direct result of the non-smooth reference acceleration profiles $a_{p2,ref}(t)$ and $\ddot{\psi}_{ref}(t)$. Furthermore, till $t = 2[s]$ the longitudinal reference slip values are perfectly smooth, as could be expected from figure 5.2.

5.5 Conclusion

The Dynamic Inverse Algorithm (DIA) addresses the decoupled control of an over-actuated vehicle, the four wheel steer and four wheel drive ATS/AGV. An objective function is formulated in order to deal with the redundant number of acutators. A numerically fast unconstrained optimization procedure is used for the minimization of the objective function. Convergence is guaranteed by using the previous output of

the DIA as initial starting guess for the optimization procedure. The resulting output of the DIA is used for the calculation of the reference wheel rotational velocities and the reference steer angles. They are used as reference inputs to the local servo controllers, which will be further discussed in chapter 6. Based on the addressed separation principle for the reference values of the local servo controllers it is stated that the implementation of the DIA is based on a feedforward compensation of the longitudinal and lateral wheel slip.
Since no actuator dynamics are incorporated in the DIA, the reference trajectory is required to show a certain degree of smoothness in its acceleration profiles. Furthermore, it is required that the initial conditions of the DIA (optimization), represented by the longitudinal slip $\kappa_{ij,0}$ and steer angles $\delta_{ij,0}$, closely match with the reference trajectory.
In general, it can be concluded that the DIA is capable of coordinating all eight actuators of the vehicle up to limit tyre adhesion conditions and thereby enables the control of the ATS/AGV under extreme performance conditions. Furthermore, because the force/slip characteristics are incorporated into the control model, the algorithm explicitly handles the control saturation in the longitudinal and lateral direction of the tyre. Optimal tractive forces for the longitudinal and lateral direction of the tyre are commanded without excessive wheel slip.

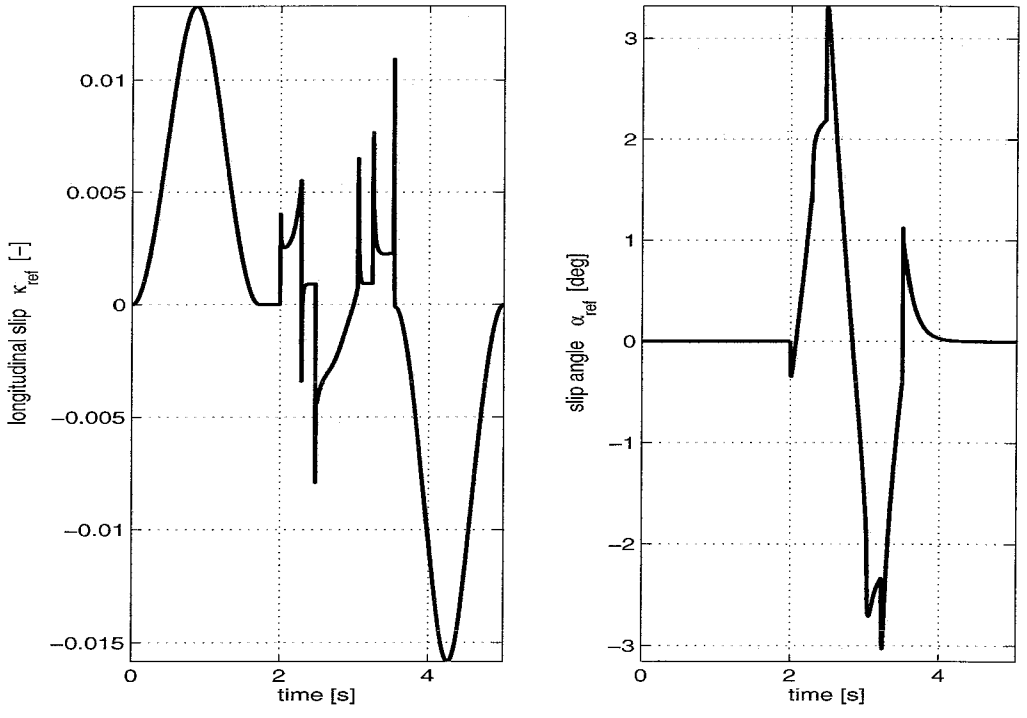

Figure 5.7: Reference longitudinal slip $\kappa_{ref,1R}$ (left) and reference lateral slip $\alpha_{ref,1R}$ (right)

Chapter 6

Feedback control

Finally, a master-slave control architecture is proposed for the motion control design. At the slave control level, the four steer angles and the four wheel rotational velocities are regulated by the local servo controllers. The master control level deals with the trajectory tracking of the vehicle. With the independent control of the wheel rotational velocities ω_{ij} and the steer angles δ_{ij} a certain degree of independence in the actuation of the vehicle is realized. In this way, a more generic controller design and robustness to external (model) disturbances can be achieved. In section 6.1, the design of the local servo controllers will be discussed, while section 6.2 is devoted to the design of the tracking controller.

6.1 Local servo control

In the slave control level, the four drive actuators and the four steer actuators are regulated by local servo controllers. It is assumed that the reference values $\omega_{ref,ij}$ and $\delta_{ref,ij}$ are available from the DIA. They are used as reference inputs for the local servo controllers of the drive actuators and the steer actuators, respectively.
Figure 6.1 graphically illustrates the slave controllers. Each local servo controller has a feedback from the vehicle model. The dynamic vehicle model discussed in section 3.2 is used for this purpose. Figure 6.1 also shows the disturbance torques $T_{d,drive,ij}$ and $T_{d,steer,ij}$ acting on the drive and steer actuators, respectively, which are a direct result of the tyre/road-friction forces generated by the tyre. This behavior requires a control design for the local servo controllers which is robust with respect to the disturbance T_d. In section 6.1.1, the design of the servo controller for the drive actuator will be discussed and section 6.1.2 deals with the design of the servo controller for the steer actuator.

6.1.1 Drive servo

The quarter car model, discussed in section 3.1.3, is used for the design of the servo controller and the simulation of the servo controlled drive actuator. Originally, the dynamic model of the drive actuator is non-linear. However, for the design of the servo controller only the linear plant model, consisting of the dc-motor, the gearbox and the wheel rim, is considered. Recalling (3.16c) and (3.16d), the transfer functions

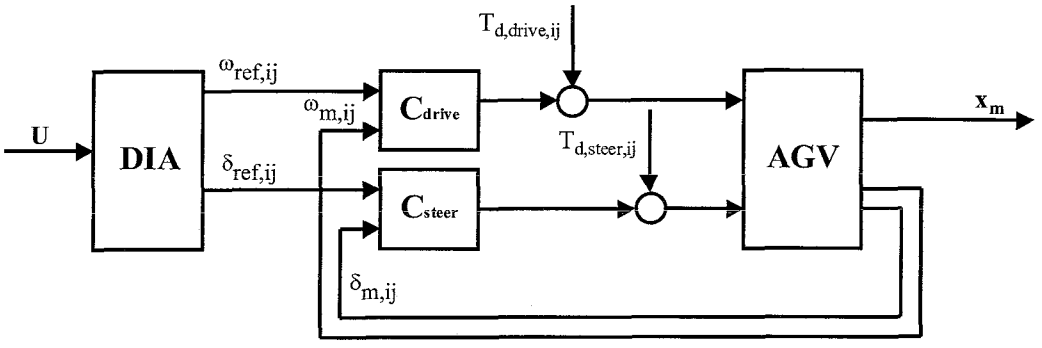

Figure 6.1: Lower control level of the proposed master-slave control architecture; local servo controllers for the drive and steer actuators, C_{drive} and C_{steer}, respectively.

H_1 and H_2 are defined as

$$H_1(s) = \frac{\omega(s)}{u_d(s)} = \frac{i_{drv}}{\tau_d s + 1} \cdot \frac{1}{J_w s + B_w} \tag{6.1}$$

$$H_2(s) = \frac{\omega(s)}{T_{d,drive}(s)} = \frac{1}{J_w s + B_w} \tag{6.2}$$

with J_w the inertia of the wheel rim, τ_d the time constant of the dc-motor, i_{drv} the gear ratio and B_w the viscus friction. Considering the linear plant model transfer function H_1, a rather straightforward linear controller C_{drive} is proposed, consisting of a proportional and integral action with gain $K_{w,p}$ and $K_{w,i}$, respectively.

$$\begin{aligned} \frac{u_d(s)}{e(s)} &= C_{drive}(s) \\ &= K_{w,p} + \frac{K_{w,i}}{s} \end{aligned} \tag{6.3}$$

with

$$e(s) = \omega_{ref}(s) - \omega_m(s) \tag{6.4}$$

In order to protect the servo controller for the wind-up behavior of the integral action, an upper bound $u_{d,max}$ and lower bound $u_{d,min}$ are defined and are set to approximately 30% of the nominal actuator torque. Since the dc-motor has a bandwidth of approximately $30Hz$, it is chosen to tune the controller at a bandwidth of $15Hz$. In figure 6.2, details on the controlled system are given in the frequency plots of the open-loop (CH_1) and the sensitivity ($(1 + CH_1)^{-1}$) transfer function. It can be concluded that the integral action enhances the steady-state tracking performance at the cost of $-\pi/2\,[rad]$ phase delay. The marginally chosen control bandwidth also provides some robustness to external disturbances or model uncertainties through the rather large attained gain margin (GM=65dB) and phase margin (PM=52deg). Furthermore, it is found that the process disturbance $T_{d,drive}$ significantly reduces the tracking performance of the servo controlled drive actuator. Therefore, in the next section a method for the disturbance rejection is proposed which enhances the tracking performance with a relatively small design effort.

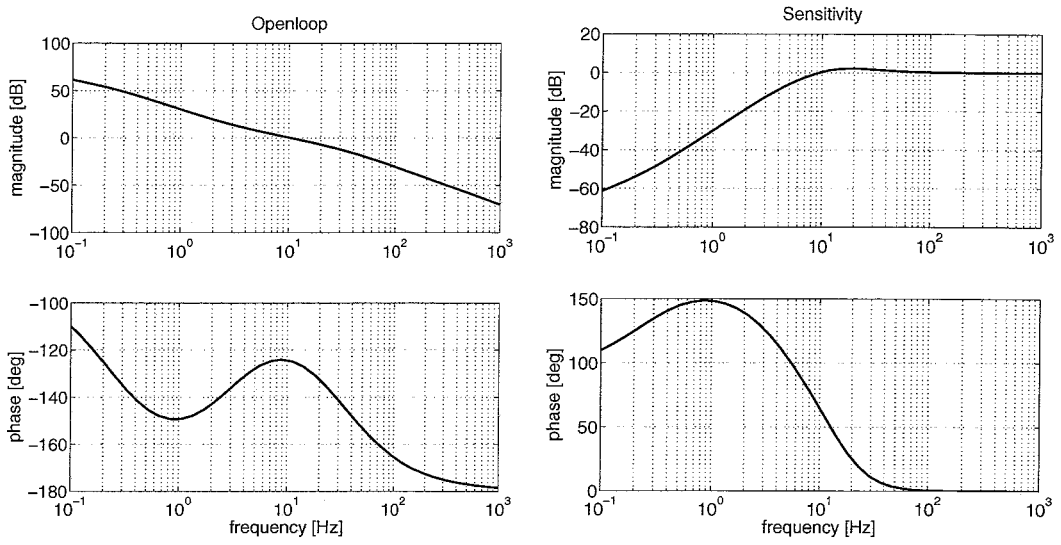

Figure 6.2: frequency characteristics of the tuned drive servo system; Open loop (left) and Sensitivity S (right), $\max|S| = 3dB$

Disturbance rejection

The generated tyre/road-friction force $F(\kappa, F_z)$ acts as a proces disturbance torque on the plant model H_2 and was therefore not initially considered in the design of the controller $C_{drive}(s)$. In order to investigate the real nature of the proces disturbance, the servo controlled drive actuator with the quarter car model is schematically depicted in figure 6.3. Note the feedback of the measured rotational velocity of the wheel ω_m and the longitudinal velocity v. In the figure it is shown that the wheel rotational velocity ω is finally converted into a tyre force F which causes the wheel with a certain attached mass m to accelerate to a planar velocity v. The same tyre force F is also fed back through the arm R_e which gives $T_{d,drive} = R_e \cdot F(\kappa, F_z)$. As illustrated in figure 6.3, the dynamics of the wheel rotational velocity $\omega(s)$ can be written as

$$\omega(s) = H_1(s)\, u_d(s) - H_2(s)\, T_{d,drive}(s) \tag{6.5}$$

In order to improve the tracking performance of the servo controlled drive actuator it is chosen to apply a linear feedforward compensation for the disturbance $T_{d,drive}$ and the dynamics of the wheel rim presented in (6.1). The drive servo control law then becomes

$$\begin{aligned} u_d(s) &= \underbrace{H_1^{-1}(s)\,(\omega_{ref}(s) + H_2(s)\, T_{d,drive}(s))}_{feedforward\ compensation} + \underbrace{C_{drive}(s)\, e(s)}_{feedback\ compensation} \\ &= \left(\frac{\hat{J}_w}{i_{drv}} \cdot s + \frac{\hat{B}_w}{i_{drv}}\right) \omega_{ref}(s) + \frac{R_e}{i_{drv}} \cdot \hat{c}_{x,norm,0} \hat{F}_z \kappa_{ref}(s) + \\ &\quad \left(K_{w,p} + \frac{K_{w,i}}{s}\right) e(s) \end{aligned} \tag{6.6}$$

The reference signals $\omega_{ref}(s)$ and $\kappa_{ref}(s)$ are assumed available from the Dynamic Inverse Algorithm. $\hat{c}_{x,norm,0}$ is the estimated normalized linear tyre stiffness in longitudinal direction and $\hat{F}_z$ the estimated vertical wheel load. $\hat{J}_w$ and $\hat{B}_w$ are the estimated wheel inertia and the velocity dependent friction, respectively. Note that the dc-motor dynamics in the transfer function H_1 are neglected in the feedforward compensation.

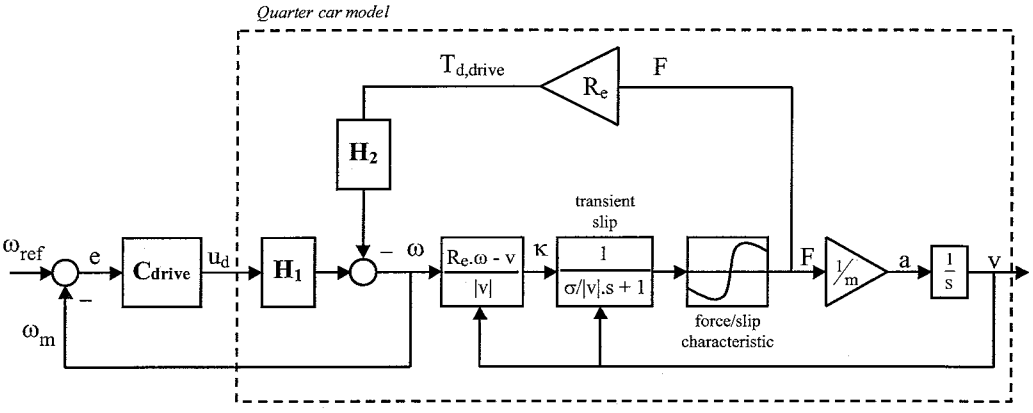

Figure 6.3: Schematic depiction of the quarter car system interactions

It is well known that the tyre has non-linear dynamics which are responsible for a strong varying bandwidth of the tyre while generating a force. It is therefore very difficult to obtain an accurate prediction of the dynamic behavior of the disturbance torque $T_{d,drive}$. For this reason, the design of the feedforward compensator is limited to the well known (linear) steady-state force/slip characteristic of the tyre. Figure 6.4 illustrates the response behavior of the wheel rotational velocity $\omega_m(t)$ of the servo controlled quarter car model for a ramp input on the reference wheel rotational velocity $\omega_{ref}(t)$. An initial velocity of $v_0 = 5\,km/h$ is commanded in order to avoid the poor damped behavior of the tyre near zero velocities.
From figure 6.4, it can be concluded that the response of the servo controller in combination with the feedforward compensation leads to a faster and better damped response behavior of the wheel rotational velocity $\omega(t)$. Although the tracking performance of the drive servo is significantly improved, it is still believed that the drive servo can be further improved by taking the following aspects into account:

- Dynamic estimated vertical wheel loads in case of a multiple-wheel vehicle model.
- The combined slip situation for the longitudinal and lateral direction of the tyre.
- Transient tyre behavior.

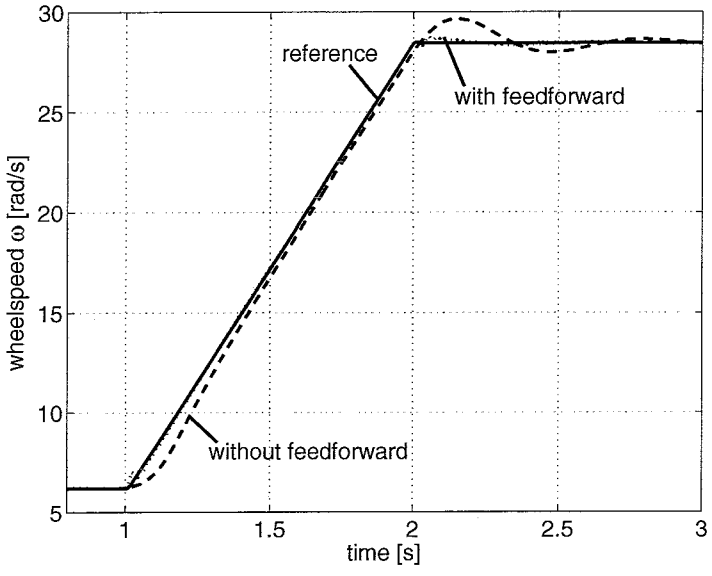

Figure 6.4: Dynamic response of the wheel rotational velocity $\omega(t)$; reference wheelspeed (solid), servo control without feedforward (dashed) and servo control with feedforward (dotted)

Dynamic behavior

The dynamic behavior is analyzed by looking at the ramp-input and sine-input dynamic responses of the servo controlled non-linear quarter car model, which is implemented in Matlab Simulink for that purpose. The reference acceleration $a_{ref}(t)$ is translated into a reference wheel rotational velocity $\omega_{ref}(t)$ using a simplified version of the proposed dynamic inverse method. Since the considered quarter car model is a SISO-system, the solution $\kappa_{ref}(t)$ is unique and therefore easy to determine. The obtained $\omega_{ref}(t)$ serves as an input to the servo controller C_{drive} in (6.3). In this way, the dynamic response of $a_{ref}(t) \rightarrow a_m(t)$ can be simulated.
The acceleration response behavior for the ramp-input and sine-input reference acceleration is plotted in figure 6.5. The ramp-input responses in figure 6.5 show some high frequent dynamics in the beginning of each response. This transient behavior typically results from the excitated higher frequent dynamics of the tyre. By using a ramp-input instead of a step-input less high frequent tyre dynamics are excitated and thereby a smoother response is obtained. A faster transient response behavior for $a_m(t)$ is observed for ramp-input excitations with a larger amplitude. The integral action of the drive servo controller results in an excellent steady-state tracking behavior. Furthermore, for the higher frequent ($\geq 5Hz$) sine-input responses it can be seen that there is a gradual decrease in the tracking performance at the cost of some phase delay and amplitude.

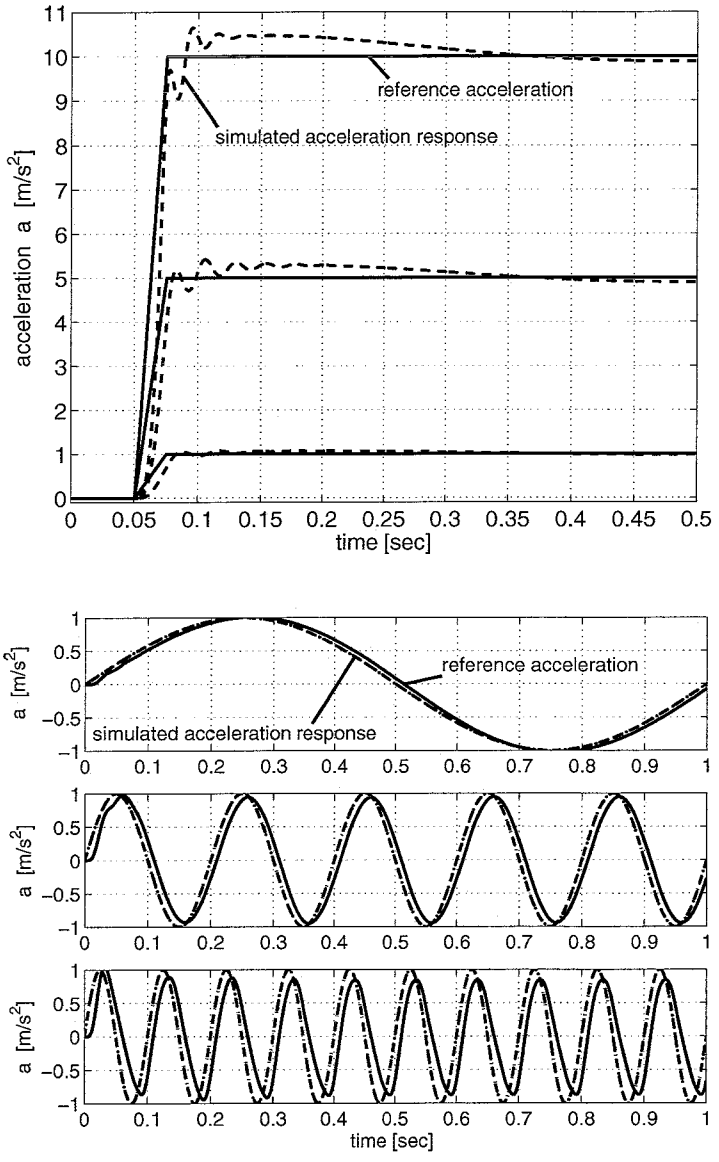

Figure 6.5: Acceleration response behavior of the servo controlled drive actuator. Top: ramp-input reference acceleration ($\Delta a = 1, 5, 10\, m/s^2$ at $v_0 = 20\, km/h$), $a_{ref}(t) \rightarrow a_m(t)$; Bottom: sine-input reference acceleration (amplitude $= 1\, m/s^2$ and $freq = 1, 5, 10\, Hz$ at $v_0 = 0\, km/h$), $a_{ref}(t) \rightarrow a_m(t)$

6.1.2 Steer servo

The design of the servo controller for the steer actuator is based on the asymptotic robust controller design in [9]. The so-called Davison controller was used in a previous ATS/AGV application and is experimentally validated at a control bandwidth of 5 Hz. The same controller is used in this study. The steer servo controller provides asymptotic tracking combined with a certain degree of robustness against external process disturbances for a limited torque usage. A short description of the Davison controller is given below. The steer actuator dynamics are represented by the second order system representation:

$$J_s\ddot{\delta} = i_{str}u_s \qquad [Nm] \tag{6.7}$$

where J_s is the system's inertia, i_{str} the gearbox ratio and u_s the torque input. Integrating $\ddot{\delta}(t)$ twice gives the steer angle $\delta(t)$. The external disturbance torque $T_{d,steer}$, exerted on the tyre vertical axis by the road surface, is not considered in the controller design. This is found acceptable because the relatively large gearbox ratio reduces the influence of the disturbance torque $T_{d,steer}$ on the system dynamics. The servo problem is therefore initially considered as a positioning problem without external disturbances.

The Davison controller has two objectives: Firstly, the controller has to track the reference steer angle δ_{ref}, secondly, the controller needs to stabilize the steer dynamics in (6.7). The tracking error $e_s(t) = \delta_{ref}(t) - \delta(t)$ is introduced. For the asymptotic tracking it is required that

$$\lim_{t\to\infty} e_s(t) \to 0 \tag{6.8}$$

This asymptotic tracking behavior in (6.8) is achieved by introducing the servocompensator state equation in:

$$\dot{\xi}(t) = e_s(t) \tag{6.9}$$

Obtained by integration, $\xi(t)$ is the state variable of the servocompensator and the tracking error $e_s(t)$ forms the input. The input to the steer actuator is then chosen as:

$$u_s(t) = k_3\xi(t) + v \tag{6.10}$$

with $k_3 > 0$ and v a new additional input. Besides the asymptotic tracking behavior for the orientation of the wheel $\delta(t)$, it is also required that the controller assures stable closed loop dynamics of the servo controlled steer actuator. The steer dynamics are stabilized by using proportional state feedback control. It is assumed that the states $\delta(t)$ and $\dot{\delta}(t)$ are available. The state feedback law then becomes:

$$v = k_1\delta(t) + k_2\dot{\delta}(t) \tag{6.11}$$

such that the steer actuator input can be written as

$$u_s = k_1\delta(t) + k_2\dot{\delta}(t) + k_3\xi(t) \tag{6.12}$$

with $k_1, k_2 < 0$. By properly choosing the values for k_1 and k_2, the closed loop system poles can be assigned arbitrary negative real components and hence stabilize

the dynamics of the servo controlled steer actuator. Finally, the values for the constants k_1, k_2, k_3 are calculated by using optimal control theory. This is done by using the following system representation:

$$\begin{bmatrix} \dot{\delta} \\ \ddot{\delta} \\ \dot{\xi} \end{bmatrix} = \begin{bmatrix} 0 & 1 & 0 \\ 0 & 0 & 0 \\ -1 & 0 & 0 \end{bmatrix} \cdot \begin{bmatrix} \delta \\ \dot{\delta} \\ \xi \end{bmatrix} + \begin{bmatrix} 0 \\ i_{str}/J_s \\ 0 \end{bmatrix} u_s + \begin{bmatrix} 0 \\ 0 \\ 1 \end{bmatrix} \delta_{ref} \tag{6.13}$$

where the servocompensator state is incorporated into the system description.

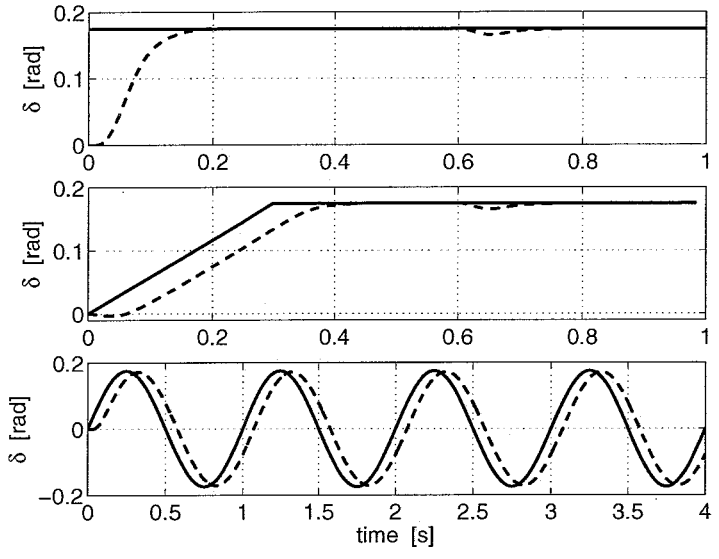

Figure 6.6: Simulated response behavior for the servo controlled steer actuator; reference steer angle (solid) and simulated response

The simulated dynamic response behavior of the steer angle $\delta(t)$ is illustrated in figure 6.6. The reference (solid) input steer angle $\delta_{ref}(t)$ and simulated (dashed) steer angle $\delta(t)$ are compared for three different type of input signals combined with an introduced proces disturbance torque $T_{d,steer}(t)$. For the step- and ramp-input reference steer angles, the disturbance torque is increased stepwize on $t = 0.6\,[s]$ from initially $20\,Nm$ to a final constant value of $60\,Nm$. The sinus-shaped reference steer angle with a frequency of 1 Hz has a corresponding synchroon sinus-shaped disturbance torque of 1 Hz and amplitude $60\,Nm$.
It can be concluded that the tracking response of the steer servo is well damped, has an approximately zero degree overshoot and shows an excellent disturbance rejection behavior. The tracking of the sinusoid reference signal show a good peak-to-peak tracking, although the asymptotic tracking behavior has a significant phase lag.

6.2 Tracking control

With the DIA and the local servo controllers used for the coordination of the drive and steer actuators, a (approximately) decoupled linear input-output behavior of the overactuated vehicle is realized. In the design of the tracking controller it is therefore assumed that the lower (slave) level in the control architecture consists of three independent controllable subsystems representing the longitudinal, lateral and yaw motion of the vehicle. Since there are three independently controlled degrees of freedom in the planar motion of the vehicle, the system is fully controllable. For consistency reasons with the DIA it is chosen to use the rotation matrix (4.4) for calculating the tracking error e(t) in operational space coordinates.

$$\mathrm{e}(t) = \mathrm{R}(\theta_{ref}(t))\,(\mathrm{x}_{g,ref}(t) - \mathrm{x}_g(t))$$

$$\mathrm{e}(t) = \begin{bmatrix} e_1(t) \\ e_2(t) \\ e_3(t) \end{bmatrix} = \begin{bmatrix} \cos(\theta_{ref}(t)) & \sin(\theta_{ref}(t)) & 0 \\ -\sin(\theta_{ref}(t)) & \cos(\theta_{ref}(t)) & 0 \\ 0 & 0 & 1 \end{bmatrix} \cdot \begin{bmatrix} x_{g,ref}(t) - x_g(t) \\ y_{g,ref}(t) - y_g(t) \\ \psi_{ref}(t) - \psi(t) \end{bmatrix} \tag{6.14}$$

where e_1 and e_2 are the longitudinal and lateral position tracking errors in operational space coordinates, respectively, and e_3 the vehicle orientation error. The tracking problem is defined to be: find a feedback control law such that

$$\lim_{t\to\infty} \mathrm{e}(t) \to 0 \tag{6.15}$$

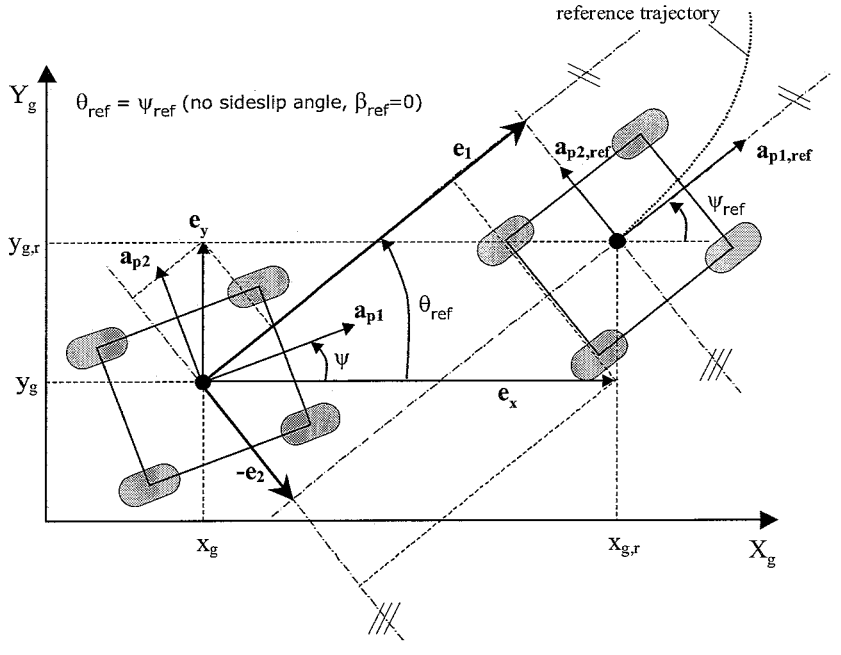

Figure 6.7: Illustration of the tracking problem.

Figure 6.7 illustrates the tracking problem with the use of a virtual reference vehicle. The virtual reference vehicle is assumed to track a reference trajectory with a zero slip

angle β, i.e. the orientation of the vehicle ψ is tangent to the trajectory of the center of gravity. Note that the longitudinal position error vector e_1 and the longitudinal reference acceleration vector $a_{p1,ref}$ lie exactly parallel to each other. The same holds for the lateral components.

The model-based control law $\mathrm{U}(t)$ is proposed for the tracking of the vehicle:

$$\begin{aligned} \mathrm{U}(t) = \begin{bmatrix} U_1(t) \\ U_2(t) \\ U_3(t) \end{bmatrix} &= \mathrm{a}_{p,ref}(t) + \mathrm{K}_p \cdot \mathrm{e}(t) \\ &= \begin{bmatrix} a_{p1,ref}(t) \\ a_{p2,ref}(t) \\ \ddot{\psi}_{ref}(t) \end{bmatrix} + \mathrm{K}_p \begin{bmatrix} e_1(t) \\ e_2(t) \\ e_3(t) \end{bmatrix} \quad \begin{bmatrix} m/s^2 \\ m/s^2 \\ rad/s^2 \end{bmatrix} \end{aligned} \tag{6.16}$$

Equation (6.16) consists of three separate proportional feedback error compensators, each for one degree of freedom of the vehicle to be controlled and three acceleration feedforward compensators, which are used to increase the tracking performance. The proportional feedback error compensation $\mathrm{K}_p\,\mathrm{e}(t)$ is introduced in order to provide robustness to external disturbances and unmodelled dynamics which are not accounted for by either the local servo controllers or the DIA. K_p is a (3×3) positive definite diagonal matrix

$$\mathrm{K}_p = \begin{bmatrix} kp_1 & 0 & 0 \\ 0 & kp_2 & 0 \\ 0 & 0 & kp_3 \end{bmatrix}$$

containing proportional gains which are multiplied with the longitudinal position error, lateral position error and yaw angle error, respectively.
Note that in the control law $\mathrm{U}(t)$, the feedback compensation is applied to the reference trajectory on an acceleration level. This is a direct result of the proposed master-slave control architecture and the position of the Dynamic Inverse Algorithm in the motion controller. When the feedback compensation combined with the acceleration feedforward is used as input to the DIA the closed loop motion control of the vehicle is realized.
Figure 6.8 illustrates the implementation of the tracking control law $\mathrm{U}(t)$ in the master level of the motion control architecture. With the tracking controller C and the approximately decoupled control of the AGV, illustrated as the slave control level, it is possible to achieve different bandwidths for the vehicle's longitudinal translational, lateral translational and yaw angle tracking efforts. It must be said that the yaw angle control operates at a much lower bandwidth than its longitudinal and lateral components. This due to its sensitivity for steer angle variations.
Because the DIA is positioned in the loop, it is very difficult to derive a stability criterion of the controlled system. Therefore, it is suggested that the control of the vehicle remains stable as long as the optimization performed by the Dynamic Inverse Algorithm converges to the 'minimum'. In order to prevent the position error feedback compensation from becoming to large, and hence threaten the convergence of the optimization, it is chosen to apply an upperbound U_{max} and lowerbound U_{min} to the effort of the tracking control law $\mathrm{U}(t)$. The bounds U_{max} and U_{min} are set to $\pm 120\%$

of the maximum achievable acceleration level for a_{p1}, a_{p2} and $\ddot{\psi}$, respectively, which are determined by the peak friction levels in the modelled force/slip-characteristics of the tyre in the Dynamic Inverse Algorithm.

6.3 Conclusion

It can be concluded that the feedforward compensation of the disturbance torque for the drive actuator remarkably improves the dynamic response behavior. A reasonable small steady-state tracking error of the wheel rotational velocity is observed. Recall from section 6.2 that the Dynamic Inverse Algorithm is implemented in the loop between the tracking controller and the vehicle model. It is hypothesized that the closed loop controlled system handles the control saturation of the tyre slip values explicitly, while at the same time it limits, to a certain extent, the ability of the tracking controller to compensate for feedback error information. This faces a dilemma in the control design for the ATS/AGV with the Dynamic Inverse Algorithm.

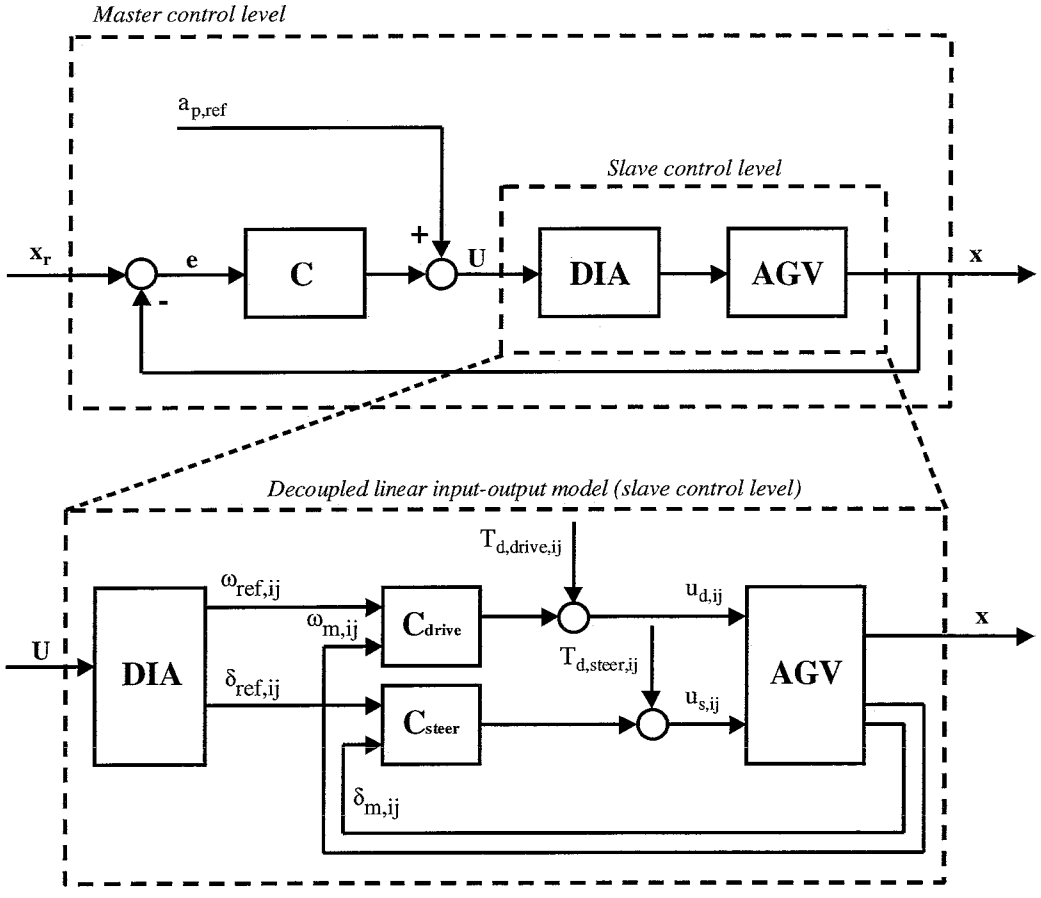

Figure 6.8: Proposed motion control architecture of the ATS/AGV; a master-slave controller.

Chapter 7

Simulation results

In this chapter, the DIA and the local servo controllers, enclosed by the tracking controller, are evaluated through closed loop simulations with the vehicle model. The simulations are performed in Matlab Simulink using the TNO ATS/CAR library [2], which provided the vehicle simulation model described in section 3.2. A sample frequency of 400 Hz is used for the simulations.
As a benchmark, some typical (extreme) vehicle manoeuvres are simulated in order to assess the performance of the motion controlled four wheel steer and four wheel drive vehicle. In order to contribute to the generalization of the control design, the servo controllers and tracking controllers are tuned such that they are able to cope with most of the reference trajectories for just a single set of controller parameters. The longitudinal (k_{p1}) and lateral (k_{p2}) position tracking controllers of the vehicle are tuned at a closed loop bandwidth of approximately $2\,Hz$, while the yaw angle (k_{p3}) tracking controller is tuned at a closed loop bandwidth of approximately $0.5\,Hz$. Note that the tracking controller consists of simple proportional feedback controllers which are rather mildly tuned for the simulated extreme performance trajectories in this chapter. The drive servo ($\omega_{ref} \rightarrow \omega$) and steer servo controllers ($\delta_{ref} \rightarrow \delta$) are tuned at a closed loop bandwidth of $15\,Hz$ and $5\,Hz$, respectively.
A distinction will be made between open loop (without tracking controller) and closed loop simulations, this in order to emphasize the performance of the acceleration feedforward. In section 6.1, the benefits of longitudinal slip compensation in the control of the quarter car model, representing the drive actuator dynamics, are addressed. In addition, the effect of the lateral slip compensation will be evaluated in section 7.1. Section 7.2 will be devoted to the evaluation of the combined longitudinal, lateral and yaw tracking performance of the closed loop controlled vehicle.

7.1 Lateral and yaw response behavior

The response behavior of the lateral acceleration $a_{p2}(t)$ and the yaw angle $\psi(t)$ is analyzed with the J-turn manoeuvre. In the J-turn manoeuvre the vehicle accelerates to a constant longitudinal velocity v_{p1} of $21.6\,km/h$ after which a circle with constant radius $R = 3.6\,[m]$ is followed. The circular trajectory typically results in a (smoothed) step input on the reference lateral acceleration $a_{p2,ref}(t)$ with a magnitude of $v_{p1,ref}^2/R$ and a constant reference yaw rate $\dot{\psi}_{ref}(t)$ with magnitude $v_{p1,ref}/R$. The orientation

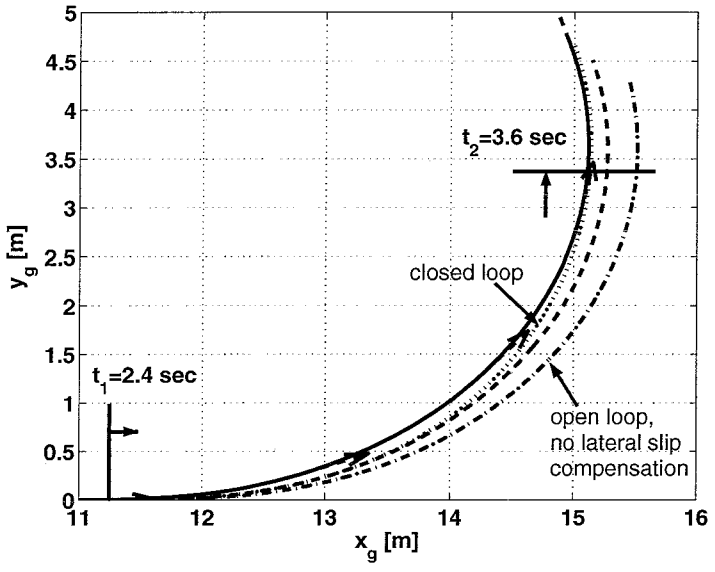

Figure 7.1: Simulated J-turn trajectories; reference trajectory (solid), closed loop (dotted), open loop (dashed), open loop without lateral slip compensation (dashdot).

of the vehicle is thus kept tangent to the reference trajectory, i.e. a reference slip angle $\beta_{ref}(t)$ of zero degrees. The reference acceleration profiles of the J-turn are defined by using a skew-sine acceleration profile. In this way, a reference trajectory is obtained which is guaranteed to be smooth with respect to the acceleration and the jerk profiles. After completing the 360 $[deg]$ circular trajectory the vehicle finally decelerates in longitudinal direction to a complete standstill. Figure 7.1 illustrates the simulated J-turn trajectories for a closed loop and open loop controlled vehicle. For the open loop simulations a comparison has been made for the control with and without lateral slip compensation, while in both simulations the longitudinal slip compensation remains enabled. The closed loop simulation is performed with both the longitudinal and lateral slip compensation. Note that the lateral slip compensation is excluded from the control by setting $\delta_{ref} = \delta_{ideal}$, which gives

$$\delta_{ref,ij} = atan\left(\frac{\nu_{y,ref,ij}}{\nu_{x,ref,ij}}\right)$$

From figure 7.1 it can be seen that the simulated manoeuvre yields a reasonable tracking for the closed loop and open loop control, even without compensation for the lateral slip. This can be mainly explained by the excellent lateral force/slip-characteristics of the Formula SAE tyres of the ATS/AGV, which attain the same level of adhesion as in the longitudinal direction of the tyre, although the lateral slip stiffness is significantly lower (see figure C.2).
Figure 7.2 depicts the tracking error in the operational space coordinates, where e_1 is the longitudinal error, e_2 the lateral and e_3 the yaw error as defined in (6.14). The initial tracking error at the transition to the circular part of the reference trajectory between $t = 2.4$ and $t = 3.6$ $[sec]$ indicates the response time of the lateral acceleration

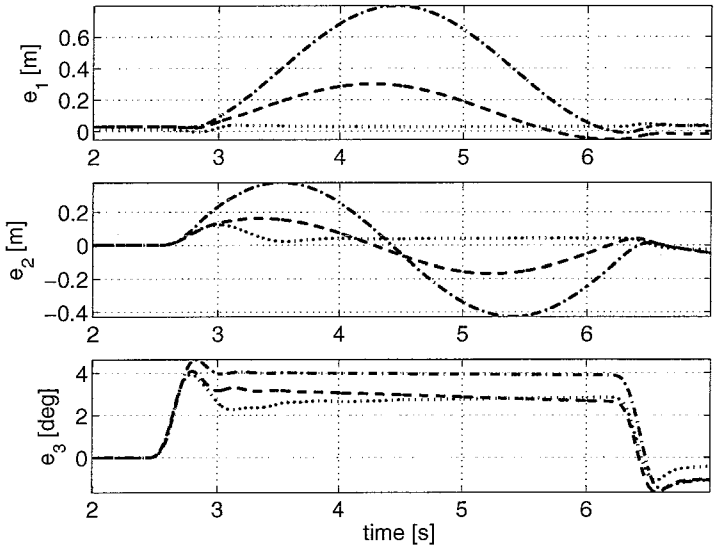

Figure 7.2: Tracking errors of the J-turn simulations; closed loop (dotted), open loop (dashed), open loop without lateral slip compensation (dashdot).

and the orientation angle of the vehicle. After $t \approx 3.6$, the closed loop tracking errors reach their steady-state values and the effect of the tracking controller becomes clearly visible. When comparing the closed loop and open loop tracking performance it can be concluded that both the position errors e_1 and e_2 have been remarkably improved, but no significant improvement is found for the steady-state yaw tracking error e_3. At the beginning of the circular trajectory the error e_3 reaches its peak value after which a static offset in the error remains. Unavoidably, the use of a proportional feedback controller for the tracking allows for a nonzero steady-state tracking error.
The origin of the tracking error e_3 can be partially explained by looking at the transient response behavior in figure 7.3, which depicts the simulation between $t_1 = 2.4$ and $t_2 = 3.6\,[sec]$. Figure 7.3 illustrates the response signals which are typical for describing vehicle dynamics in the automotive literature. The smooth lateral reference acceleration profile $a_{p2,ref}(t)$ has a magnitude of $10\,m/s^2$. The time $T_{transient}$, which defines the length of the transient period for the build up of 90% of the lateral acceleration, is equal to $0.25\,[sec]$. Note that this extreme dynamic behavior is typical for ATS/AGV, which has to exceed the capabilities of modern road cars considerably. From the top graph in figure 7.3 it can be seen that the response with lateral compensation is approximately 25% faster than the response without lateral compensation. The overshoot for the closed loop response of the lateral acceleration is due to the effort of the lateral tracking controller. Remarkably enough, the yawrate response $\dot{\psi}(t)$ and slip angle response $\beta(t)$ $(= \psi_{ref}(t) - \psi(t))$ show a similar behavior for the response with and without lateral slip compensation, open loop or closed loop, till $t \approx 2.7\,[s]$. This might indicate that either the yaw tracking controller, the weighted momentum equilibrium error in the objective function and/or the steer servo is not performing/tuned to our satisfaction. The resulting nonzero slip angle $\beta_{t=2.7} \approx 3\,[deg]$ in the lower graph

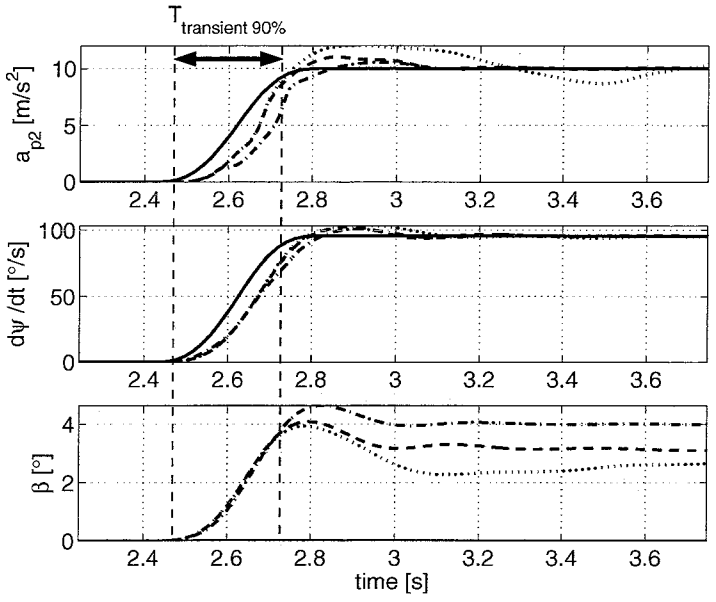

Figure 7.3: Simulated lateral acceleration, yawrate and slip angle response of the J-turn manoeuvre; reference (solid), closed loop (dotted), open loop (dashed), open loop without lateral slip compensation (dashdot)

of figure 7.3 directly reduces the capability of the controlled system to compensate for the lateral reference acceleration, since the resulting slip angle β counteracts the reference slip angles $\alpha_{ref,ij}$ of the wheels which are based on a feedforward compensation. Figure 7.4 illustrates the relevant response signals of the steer actuator. At $t \approx 2.7\,[s]$, the response of the front left steer angle $\delta_{1L}(t)$ shows a tracking error of approximately $6\,[deg]$, which results in a phase lag in the response of the slip angle $\alpha_{1L}(t)$ of the front left wheel. Note that the model error e_{p2} of the DIA at $t \approx 2.7\,[s]$ is approximately 9 % of its reference value U_{p2}. It can be seen that the reference lateral slip angle α_{1L} is kept constant at approximately $6\,[deg]$ slip, which corresponded to the lateral peak slip angle α_{peak} according to the assumed lateral force/slip-characteristic. The control saturation for the lateral slip values α_{ij} is thus handled explicitly.
Concluding, the compensation of the slip is a feedforward implementation. Because of the deviating tracking of for example the side slip angle $\beta(t)$, the performance of the feedforward lateral slip compensation is degraded for this particular trajectory. A more realistic and desirable bound for the side slip angle, in this particular trajectory, would be $\beta(t) < 1[deg]$. It can be concluded that the tracking error, especially for the orientation angle of the vehicle, has to be significantly improved for an appropriate slip compensation. It is suggested to increase the proportional gain of the yaw-tracking controller.

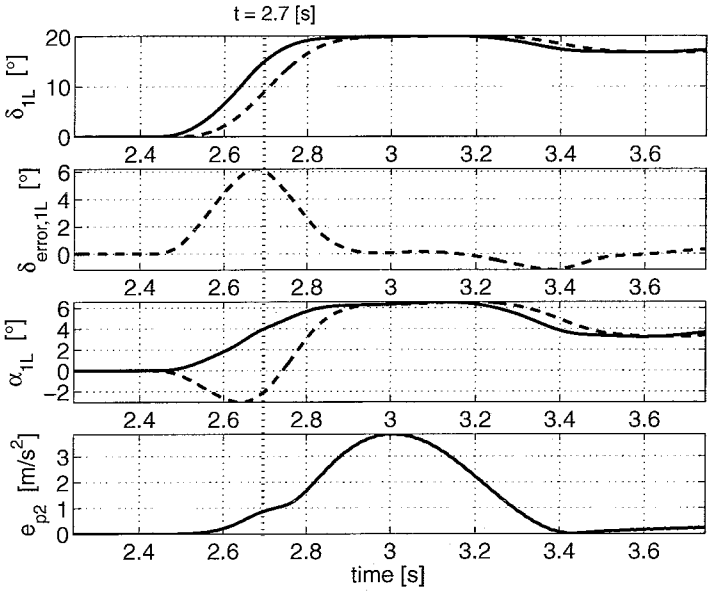

Figure 7.4: Closed loop simulation results of the J-turn manoeuvre for the front left wheel; reference values (solid), measured values (dashed).

7.2 Closed loop tracking

The overal tracking performance for combined longitudinal, lateral and yaw manoeuvring is evaluated through closed loop simulations with the lane change manoeuvre in section 7.2.1 and the eighttrack manoeuvre in section 7.2.2.

7.2.1 Lane change manoeuvre

The same lane change manoeuvre as discussed in section 5.4.2 is used. During the lane change, the vehicle makes a sideward evasive manoeuvre with its orientation angle tangent to the reference trajectory. A constant longitudinal velocity v_{p1} of 22 km/h is attained. Because of the non-smooth reference acceleration profiles, only a static estimate of the vertical wheel load $F_z(t)$ is used in the DIA. Figure 7.5 illustrates the simulated trajectories for the closed loop controlled system with and without lateral slip compensation, respectively. The corresponding position tracking errors $e_i(t)$ are illustrated in figure 7.6. Again, it is found that the compensation of the lateral wheel slip improves the closed loop tracking of the vehicle. Although the reference trajectory is non-smooth with respect to the acceleration profiles, the closed loop system with the DIA is able to cope with the trajectory. Recall the corresponding model errors from the DIA for the lane change manoeuvre in section 5.4.2. In order to illustrate especially the effect of the neglected steer servo dynamics in the DIA, the reference and measured acceleration profiles of the lane change manoeuvre are plotted in figure 7.7. It can be concluded that the tracking of the reference lateral acceleration $a_{p2,ref}(t)$ and the reference yaw acceleration $\ddot{\psi}_{ref}(t)$ suffers from the limited control bandwidth of the servo controlled steer actuator.

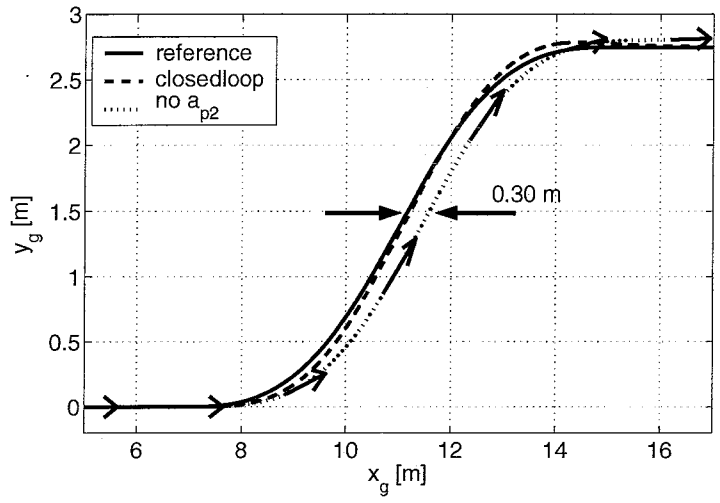

Figure 7.5: Simulated trajectories for the lane change manoeuvre; reference trajectory (solid), closed loop (dashed), closed loop without lateral slip compensation (dotted).

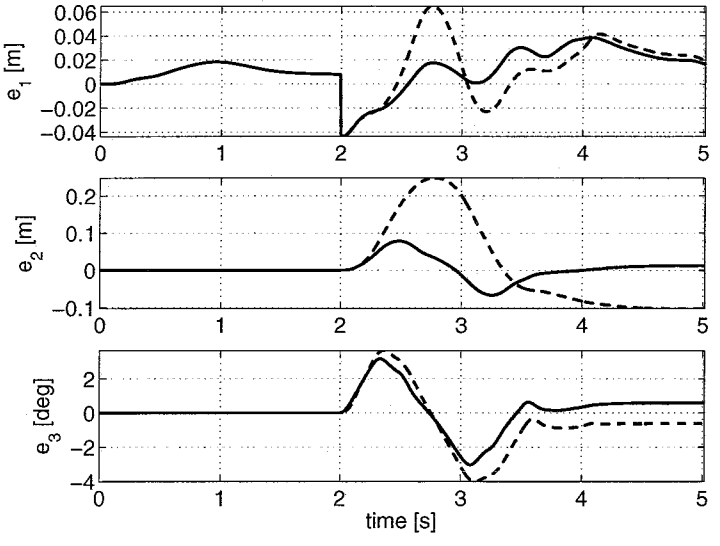

Figure 7.6: Position tracking errors for the lane change manoeuvre; closed loop (solid), closed loop without lateral slip compensation (dashed).

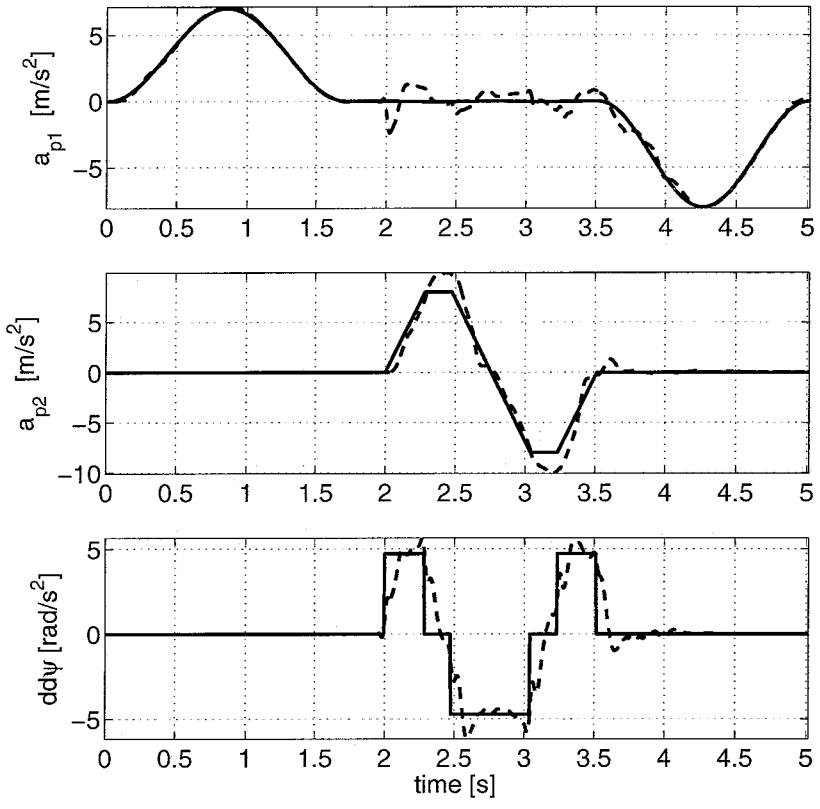

Figure 7.7: Reference (solid) and measured (dashed) acceleration profiles for the closed loop tracking of the lane change manoeuvre with longitudinal and lateral slip compensation.

7.2.2 Eighttrack manoeuvre

The eighttrack manoeuvre is chosen for the evaluation of the closed loop tracking because it is one of the most challenging manoeuvres when looking at the resulting position tracking errors $e_i(t)$. This is explained by the fact that the tracking of the eighttrack manoeuvre requires a constantly changing steer angle $\delta_{ij}(t)$ combined with two circular shaped trajectory parts with a constant radius of $R = 4\,[m]$. The longitudinal velocity $v_{p1}(t)$ is kept constant at 16 and 25 km/h, respectively, after a sine-shaped acceleration. Consequently, a constant reference lateral acceleration $a_{p2,ref}$ of respectively 5 and 12 $[m/s^2]$ during the circular shaped trajectory parts is attained. The orientation angle is kept tangent to the trajectory resulting in a zero degree reference slip angle $\beta_{ref}(t)$. Note that the vertical wheel load shifts from the left side to the right side of the vehicle during the manoeuvre. Figure 7.8 illustrates the closed loop trajectories for the two velocities both in a closed loop scenario with longitudinal and lateral slip compensation.

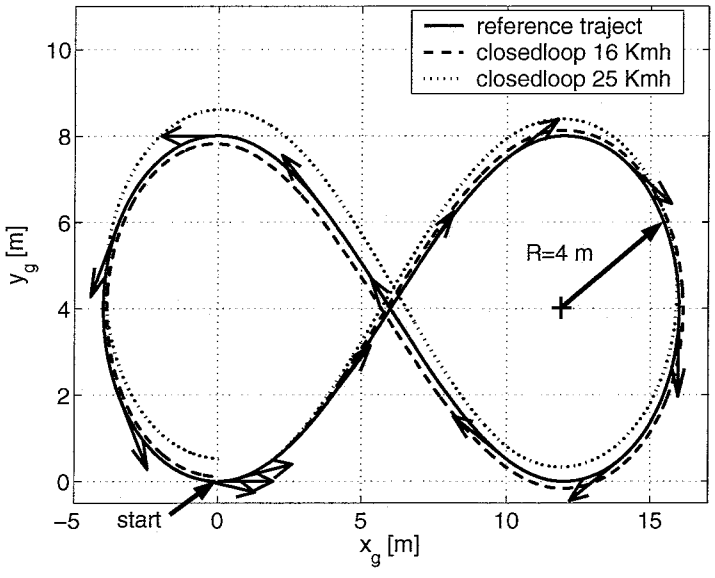

Figure 7.8: Simulated closed loop trajectories with a constant longitudinal velocity of 16 km/h (dashed) and 25 km/h (dotted).

The corresponding smooth reference acceleration profiles $a_{p1,ref}(t)$, $a_{p2,ref}(t)$ and $\ddot{\psi}_{ref}(t)$ are depicted in figure 7.9. Recall that the 25 $[km/h]$ trajectory requires a limit lateral tyre adhesion during tracking, which can thus be considered as an extreme operating manoeuvre. In figure 7.10, the closed loop position tracking errors $e_i(t)$ are compared for the 25 $[km/h]$ trajectory with ($\delta \neq \delta_{ideal}$) and without($\delta = \delta_{ideal}$) lateral slip compensation. Again, it is demonstrated that the lateral slip compensation improves the tracking performance in extreme operating conditions.

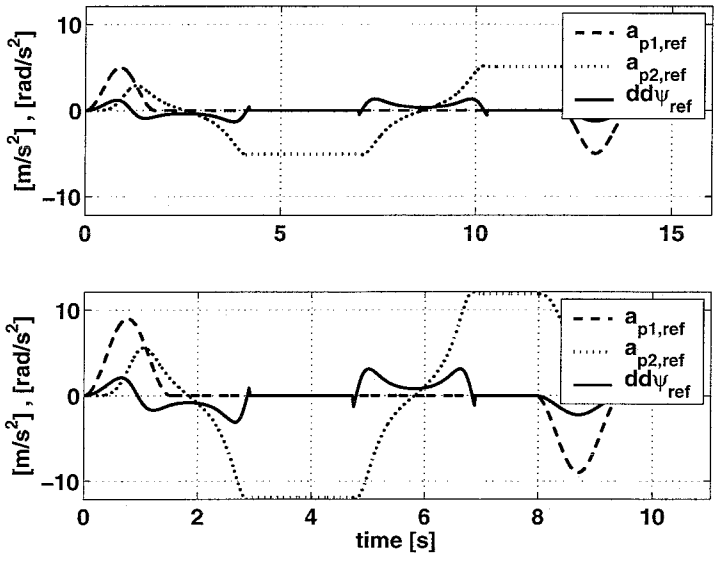

Figure 7.9: Reference acceleration profiles for the 16 km/h (top) and 25 km/h (bottom) longitudinal velocity.

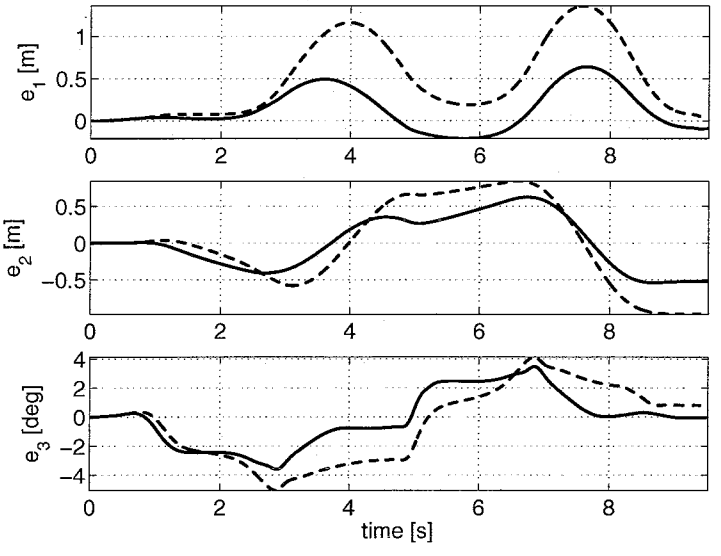

Figure 7.10: Simulated position tracking errors for the 25 km/h eighttrack manoeuvre; closed loop (solid) and closed loop without lateral slip compensation (dashed).

7.3 Conclusion

In all simulated manoeuvres, open loop or closed loop, the compensation for the longitudinal and lateral slip leads to an improved tracking performance, especially for the extreme manoeuvring of the vehicle.
The compensation of the slip is a feedforward implementation. Because of the deviating tracking of for example the side slip angle $\beta(t)$, the performance of the feedforward lateral slip compensation is degraded for most of the simulated trajectories. It can be concluded that the tracking error, especially for the orientation angle of the vehicle, has to be significantly improved for an appropriate slip compensation. It is suggested to increase the proportional gain of the yaw-tracking controller.
The simulated tracking with slip compensation for the eighttrack manoeuvre is improved, although the vehicle is always lagging behind its reference coordinates. No real overcompensation of the vehicle, as in the lane change manoeuvre, is detected. This illustrates a possible shortcoming of the closed loop controlled system as a whole.

Chapter 8

Experimental results

In order to demonstrate the potential of the DIA, experiments have been conducted. The typical vehicle manoeuvres, as discussed in the simulation chapter, are experimentally evaluated. Due to a lack of time, the feedback compensation in the tracking controller (6.16) was not used in the experiments, i.e. only open loop motion control with the use of the servo controllers is conducted. For the open loop controlled system, a comparison has been made between the tracking with and without wheel slip compensation. For the situation without slip compensation, both the reference values for $\delta_{ref,ij}(t)$ and $\omega_{ref,ij}(t)$ are based on the nominal reference values according to the DIA output transformation in (5.20) and (5.19):

$$\omega_{ref}(\nu_{x,w,ref}) = \frac{\nu_{x,w,ref}}{R_e} \tag{8.1}$$

$$\delta_{ref}(\delta_{ideal}) = atan\left(\frac{\nu_{y,ref,ij}}{\nu_{x,ref,ij}}\right)$$

The proposed feedforward compensation of the wheel disturbance torque $T_{d,drive}$ in the drive servo, as discussed in section 6.1.1, is only used in the manoeuvres conducted with wheel slip compensation. Furthermore, static estimated vertical wheel loads are used for $F_{z,ij}$ in the experiments.
The actual position and velocity of the ATS/AGV is estimated using a discrete Kalman filter in combination with a magnetic grid in the road surface. Additional sensors, like e.g. a gyro for the orientation angle of the vehicle and encoders for measuring the steer angle and wheel rotation, respectively, are used in the design of the state estimator. In the experimental results, the estimated position and velocity in the center of gravity of the vehicle is used to evaluate the tracking of the vehicle. Note that the actual vehicle is open loop controlled, hence only the reference trajectory coordinates and derivatives are used as input to the DIA.

The vehicle manoeuvring during the experiments is essentially the same as in the simulations. With the exception that the manoeuvres are restricted to the linear region of the tyre characteristics. The reason for this will be explained in section 8.1. The longitudinal dynamic response behavior of the open loop controlled vehicle is experimentally evaluated in section 8.2. While the cornering behavior, i.e. lateral and yaw response, is discussed in section 8.3.

8.1 Real-time implementation details

The most important implications regarding the real-time implementation of the DIA are summarized in this section. In order to gain real-time execution speed, the tyre model in the considered dynamics of the dynamic inverse problem is simplified to the combined linear tyre model instead of the combined non-linear tyre model. Because of this simplification, the DIA is only valid till an acceleration level of approximately $5\,m/s^2$. With the compiled version of the real-time suitable algorithm, in combination with a dSPACE 1005 processor board, a sample rate of 400 Hz is finally used for the control system.
Due to a lack of time it was not possible to validate the assumed force/slip-characteristics in the control model. Therefore, similar steady-state force/slip characteristics as in the simulation model are used. In practice, the empirical tyre model can be validated by conducting steady-state slip measurements with the tyre.
Another design problem concerns the choice of the controller bandwidths. For example, the bandwidths of the low-pass pre-filters used for the measured steer angle velocity and the measured wheel rotational velocity are subjected to the limited sample rate of the real-time implemented control system. The same holds for the drive servo controller, which has the largest bandwidth among the master- and slave-controllers. It is finally chosen to tune the drive servo controller at a bandwidth of 10 Hz. Then, as a rule of thumb, the bandwidths of the pre-filters are set to a factor four times the bandwidth of the drive servo controller. This implies that the sample rate of the control system is approximately ten times faster than the dynamical subsystem with the highest bandwidth in the control system. Any increase in the sample rate is strongly recommended due to numerical stability reasons and a further reduction of the phase lag introduced by the pre-filters. The bandwidth of the steer servo controller is kept at 5 Hz.

8.2 Longitudinal response behavior

The longitudinal response behavior is evaluated by using a pure longitudinal forward trajectory. Between $t = 0$ and $t = 1\,[sec]$ a constant longitudinal reference acceleration of $5\,m/s^2$ is prescribed after which a constant velocity of $16\,km/h$ is attained. The trajectory is smooth with respect to its acceleration and jerk profiles with a peak jerk level of $50\,m/s^3$. The velocity response signals are given in figure 8.1. It can be concluded that the actual vehicle velocity with wheel slip compensation follows the reference ramp-velocity profile more closely than the vehicle velocity without wheel slip compensation. Also, a better damped response behavior is observed. Although, when comparing the actual vehicle velocity (dashed) with the simulated velocity (dashdot), it can be seen that the slip compensation was not able to completely compensate the longitudinal tyre force, since there is still some minor weak damped behavior present. Therefore, it is suggested that when the longitudinal tyre stiffness of the assumed linear force/slip-characteristics in the control model is further increased, the velocity response will show a more damped response behavior.

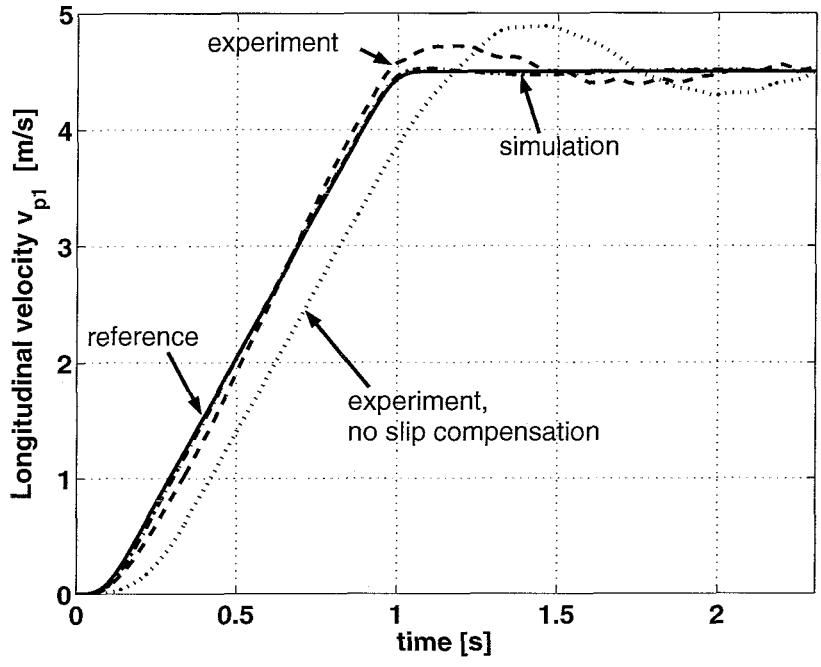

Figure 8.1: Longitudinal velocity $v_{p1}(t)$; reference (solid), actual velocity with slip compensation (dashed), actual velocity without slip compensation (dotted), simulated velocity with slip compensation (dashdot).

The assumption that the actual tyre/road-contact friction forces are much larger than in simulation is emphasized by the observed reference torques for the drive actuators, illustrated in figure 8.2. Both the actual reference drive torques for the control with and without wheel slip compensation show a 160 to 170% increase in torque usage compared with the simulated torque values. This suggests that the friction regime for the wheels is heavily underestimated in the simulation model.
The corresponding position tracking errors are depicted in figure 8.3. As expected, the longitudinal tracking without slip compensation (dashed) suffers from the poor response behavior of the drive servo's. The longitudinal position error is significantly larger that the tracking error with slip compensation. As expected, the lateral position error and vehicle orientation error show a similar behavior. Different tyre/road friction levels for the four wheels cause the actual vehicle to have a lateral position error and orientation angle error which is significantly different from the simulation.

In general, concerning the slip compensation, it can be concluded that the longitudinal wheel slip compensation remarkably improves the tracking of the vehicle. A faster and better damped response is observed for the wheel slip compensated drive servo's.

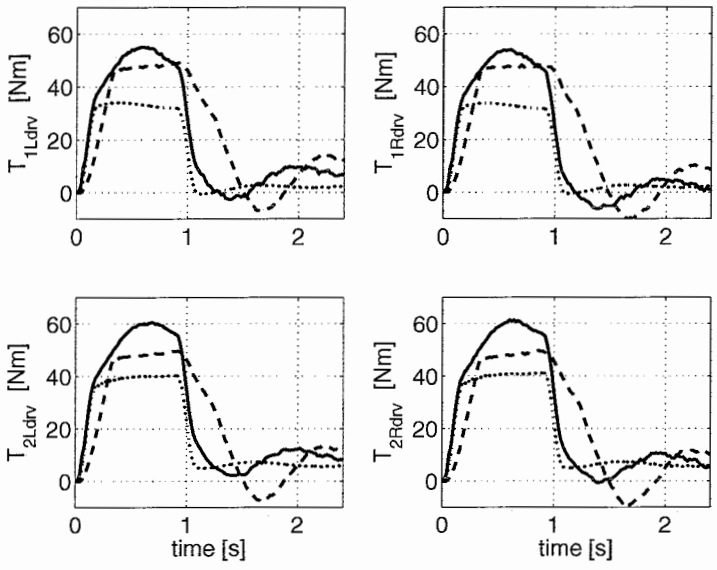

Figure 8.2: Reference torques for the drive actuators; actual torque with slip compensation (solid), actual torque without slip compensation (dashed), simulated torque with slip compensation (dotted).

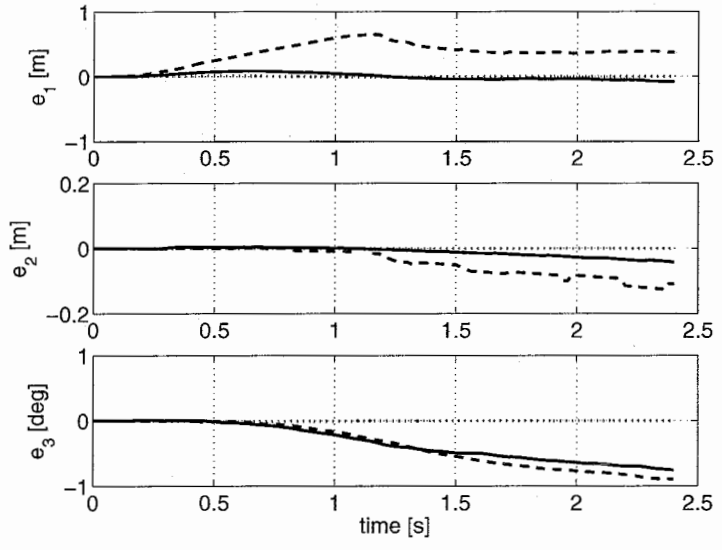

Figure 8.3: tracking errors; actual error with slip compensation (solid), actual error without slip compensation (dashed),simulated error with slip compensation (dotted).

8.3 Lateral and yaw response behavior

The response behavior of the lateral acceleration $a_{p2}(t)$ and the yaw angle $\psi(t)$ is analyzed with the J-turn manoeuvre and the eighttrack manoeuvre in section 8.3.1 and 8.3.2, respectively.

8.3.1 J-turn manoeuvre

The same manoeuvre as in the simulation, discussed in section 7.1, is used. With the exception of a larger chosen radius $R = 7.2\,[m]$, which corresponds to a constant lateral reference acceleration $a_{p2,ref}$ of $5\,m/s$ during the circular shaped reference trajectory. Again, the orientation of the vehicle is kept tangent to the reference trajectory, i.e. a reference side slip angle $\beta_{ref}(t)$ of zero degrees.
Figure 7.1 illustrates the open loop controlled J-turn trajectories with and without wheel slip compensation. Whereas the simulated trajectories, with and without slip compensation, closely match the reference trajectory, both the actual vehicle trajectories, with and without slip compensation, do not. As expected from the simulation results, there should also be a clear distinction between the actual tracking with and without slip compensation, especially in the transient period of the cornering between $t = 3.1$ and $t = 3.7\,[sec]$. However, in this transient period, the two actual vehicle trajectories show an equally poor tracking behavior. This requires a further detailed analysis of the transient response behavior of the J-turn manoeuvre.

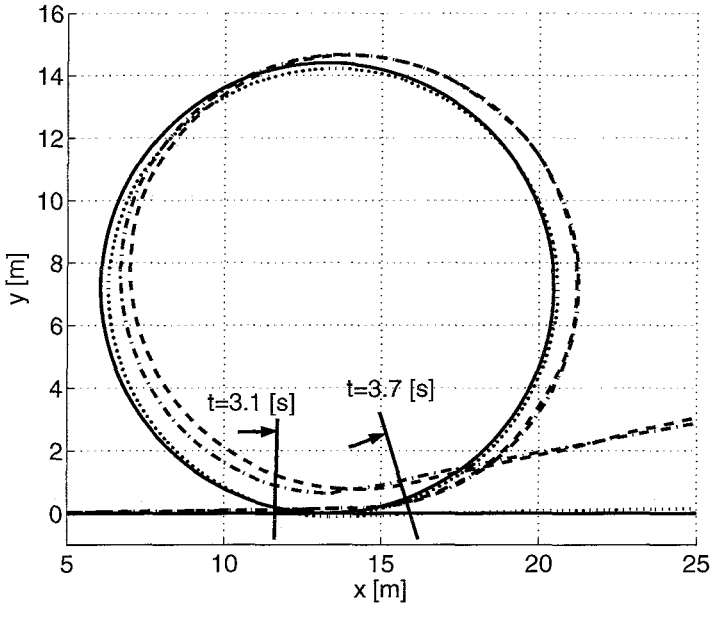

Figure 8.4: Trajectories (open loop) for the J-turn manoeuvre; reference (solid), actual trajectory with slip compensation (dashed), actual trajectory without slip compensation (dashdot), simulated trajectory with slip compensation (dotted).

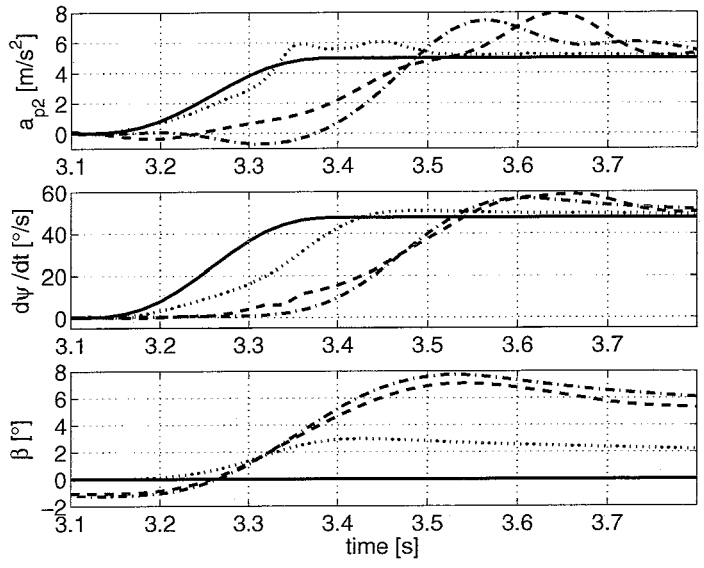

Figure 8.5: Dynamic responses of the lateral acceleration a_{p2}, yawrate $\dot{\psi}$ and side slip angle β; reference (solid), actual response with slip compensation (dashed), actual response without slip compensation (dashdot), simulated response with slip compensation (dotted).

The typical dynamic vehicle response signals between $t = 3.1$ and $t = 3.7\,[sec]$ are depicted in figure 8.5. These signals illustrate the (smooth) transition from the straight line segment to the circular section. Both the actual response and the simulated response of the controlled vehicle is plotted. It can be seen that no significant difference between the actual responses, with and without slip compensation, is found. For the actual lateral acceleration response $a_{p2}(t)$, a slight nonminimum-phase behavior is observed. No real explanation for this behavior is found. Consequently, the actual side slip angle $\beta(t)$ starts with a negative initial angle of $-1\,[deg]$ followed by a large increase to $7\,[deg]$. This lag in the response of the orientation angle of the vehicle totally obscures the ability of the feedforward lateral slip compensation to significantly contribute to an improved tracking behavior of the vehicle, since it is based on reference information only.

The tracking errors of the local steer servo controllers are found to suitably match the simulation tracking results. Nevertheless, from the reference steer and drive torques in figure 8.6 and 8.7, respectively, it can be concluded that a mismatch between the actual and the simulated torques is present. The constant steer and velocity period of the J-turn manoeuvre between $t = 5$ and $t = 10\,[sec]$ suggests structural larger disturbance torques $T_{d,ij}$ for the steer and drive servo's, respectively. This is partially explained by a larger actual friction between the tyre/road surface. The relatively large signal-to-noise ratio for the reference steer torques $T_{ref,str,ij}$ is caused by the combination of a heavily tuned steer servo, the relatively small bandwidths of the pre-filters for the steer velocity signals and the limited sample rate of the control system.

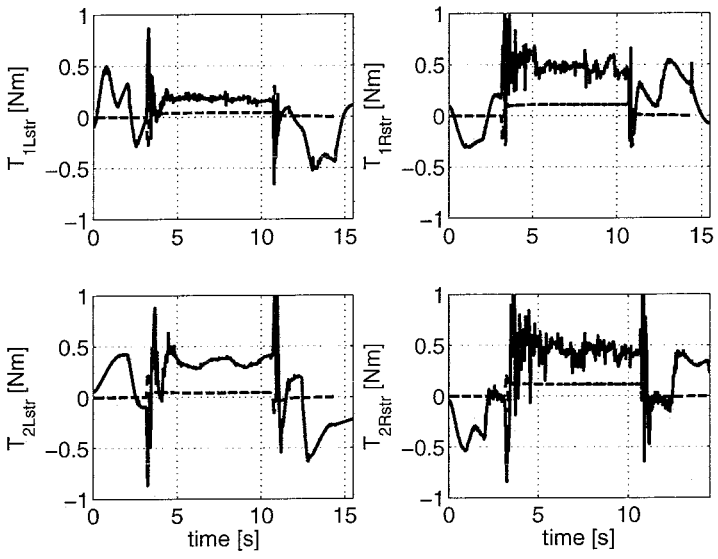

Figure 8.6: Reference torques for the steer actuators; actual torque with slip compensation (solid), simulated torque with slip compensation (dashed).

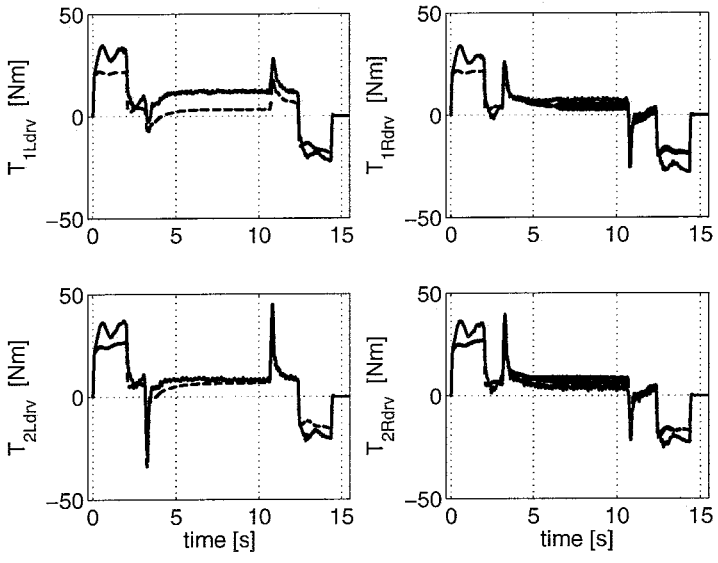

Figure 8.7: Reference torques for the drive actuators; actual torque with slip compensation (solid), simulated torque with slip compensation (dashed).

8.3.2 Eighttrack manoeuvre

Finally, the open loop controlled eighttrack manoeuvre without wheel slip compensation is evaluated. In the eighttrack manoeuvre, the vehicle accelerates to a constant velocity of 16.1 km/h after which the same eighttrack as discussed in section 7.2.2 is completed, followed by a deceleration to a complete standstill. The constant lateral reference acceleration $a_{p2,ref}$ during the circular shaped part ($R = 4\,[m]$) of the trajectory is 5 $[m/s^2]$. The actual and simulated trajectories are illustrated in figure 8.8. The measured orientation angle of the vehicle is depicted in the figure with small arrows. It can be concluded that the actual open loop tracking of the vehicle is reasonable, although the constantly changing reference steer angles cause the vehicle to drift away from its reference trajectory.

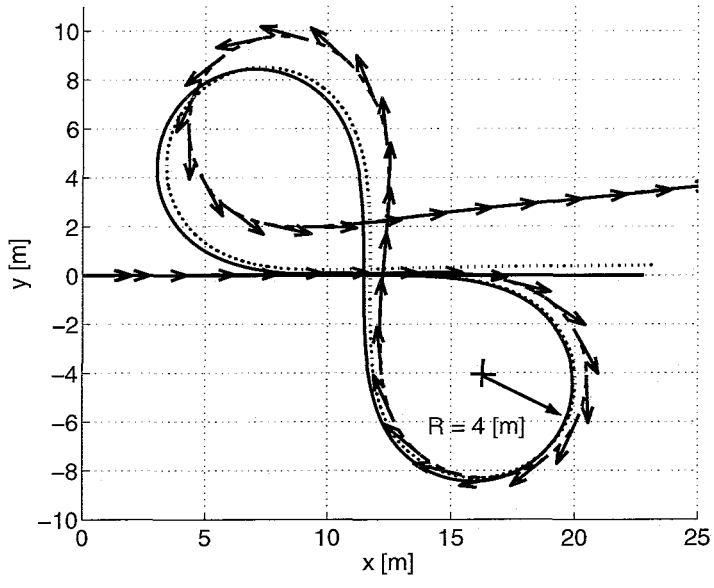

Figure 8.8: Trajectories for the eighttrack manoeuvre; reference (solid), actual trajectory without slip compensation (dashed), simulated trajectory without slip compensation (dotted).

8.4 Conclusion

Experiments are conducted with the open loop controlled ATS/AGV in the VEHIL laboratory. A comparison has been made between the tracking with and without wheel slip compensation. The Dynamic Inverse Algorithm with the modelled linear combined tyre model is valid till an acceleration level of 5 $[m/s^2]$, and consequently, the experimental manoeuvres do not exceed this acceleration level. From the experiments, the following can be concluded:

- The algorithm is successfully implemented in the real-time environment. A sample frequency of $400Hz$ is finally used. Reference wheel rotational velocities

$\omega_{ref,ij}$ and steer angles $\delta_{ref,ij}$, in which wheel slip is accounted for, are prescribed in a feedforward manner.

- Compared to the simulation results, a structural higher actual torque usage by the drive and steer servo is observed.
- The longitudinal slip compensation significantly improves the tracking, even though the slip is not fully compensated for. A faster and better damped response of the servo controlled drive actuator is observed.
- The lateral slip compensation is obscured by the tracking error resulting from the open loop control of the vehicle. The exceptionally large side slip angle $\beta(t)$ exceeds the commanded lateral reference slip angles for the wheels, which are based on a feedforward implementation.

Regardless of the findings of the slip compensation in the experiments, it is concluded that the closed loop tracking performance should be optimized first, since the open loop tracking performance appeared to be insufficient. Although the wheel slip compensation improves the tracking performance of the vehicle, there is still the servo controller of the steer and drive actuator, respectively, which has to be able to deal with the commanded reference value. It is concluded that especially the drive servo controller suffers from the larger actual tyre/road-friction forces.

Chapter 9

Conclusions and recommendations

In this project, the motion control of a four wheel steer and four wheel drive over-actuated vehicle, called the ATS/AGV, is considered and special attention is paid to the integration of wheel slip into the control design. From the research performed, the following conclusions and recommendations are made.

9.1 Conclusions

The first objective of this project, i.e. enable the independent control of the longitudinal translation, lateral translation and orientation angle of the overactuated vehicle, has been met by designing a control algorithm, called the Dynamic Inverse Algorithm. In this DIA, an objective function consisting of the model error equations, the estimated vertical wheel loads and some additional constraints is formulated in order to deal with the redundant number of actuators. The minimization of the objective function results in four 'optimal' reference wheel rotational velocities and four 'optimal' reference steer angles. The steer and drive commands are dealt with by closing local loops around each steering and driving actuator; the presence of large friction forces makes it a necessity to apply servo control.

While improving the control of the vehicle in extreme performance conditions, wheel slip can not be neglected in the control design. For this reason, the steady-state non-linear force/slip-characteristics of the tyre are integrated in the control model. The DIA is designed to be able to deal with this non-linear vehicle modelling. Now, the coordination of the four steer servo controllers and the four drive servo controllers is based on a feedforward compensation of the longitudinal and the lateral wheel slip. Steady-state accelerating and cornering manoeuvres are simulated in order to validate the algorithm. The algorithm explicitly handles the control saturation in the longitudinal and the lateral direction of the tyre. Optimal tractive forces for the longitudinal and the lateral direction of the tyre are commanded without excessive wheel slip. In general, from the simulation results it can be concluded that the control system is capable of coordinating all eight actuators of the vehicle up to limit tyre adhesion conditions and thereby enables the control of the ATS/AGV in extreme performance

conditions.
For a proper functioning of the algorithm it is required that the steady-state force/slip-characteristics of the tyre are known a-priori and that the reference trajectory is smooth. Furthermore, the commanded reference values for the steer and drive servo controllers consist of a nominal part and an additional part accounting for the lateral and longitudinal wheel slip, respectively. This so called separation principle provides the necessary robustness to model errors in the assumed steady-state force/slip-characteristics of the tyre.

The control system is successfully implemented in a dSPACE real-time environment. The real-time minimization of the objective function with the eight optimization variables appeared to be a numerically demanding task, however, a sample frequency of 400 Hz is finally obtained for the real-time execution of the algorithm. The linear combined tyre model is used instead of the non-linear combined tyre model, as used in the simulations, in order to gain execution speed. This restriction rules out the possibility to experimentally test the control system in extreme performance conditions, since the linear tyre model is only valid till an acceleration level of approximately $5m/s^2$.

Due to a lack of time, it is chosen to conduct only open loop (without tracking controller) experiments in which a comparison will be made between the control with and without slip compensation. It is found that the longitudinal slip compensation improves the tracking performance significantly, while the lateral slip compensation does not. The effect of the lateral slip compensation is obscured by an exceptionally large measured side slip angle β in the center of gravity of the vehicle, which directly rules out the ability to properly compensate for the lateral reference acceleration in a feedforward manner.

9.2 Recommendations

Robust Optimization Concerning the convergence of Newton's unconstrained optimization method it is found that the optimization of the objective function fails to converge to an optimum when either the reference accelerations U(t) become exceptionally large or the reference trajectory is significantly non-smooth with respect to its second derivatives. Under these conditions it is suggested to run a second optimization to obtain the optimal stepsize λ for the search direction λs_k which resulted from Newton's unconstrained optimization method. In this way, the search domain for the optimization process is enlarged and hence convergence is more likely.

Tracking control In the closed loop scenario, the DIA is implemented in the loop between the tracking controller and the local servo controllers. However, a limited ability for the tracking controller to compensate for position errors has been observed. It would be interesting to investigate the benefits of placing the DIA out of the control loop and to use the obtained reference values as pure feedforward signals for the servo controllers. A disadvantage of this approach is that the ability to handle the control saturation of the tyre slip values is lost.

Servo control Regardless of the compensation of wheel slip, it is found that the tracking of the steer servo controller forms the limiting factor in the overall tracking performance of the vehicle. It would be worthwhile to investigate the use of a feedforward compensation for the steer servo in order to improve tracking performance. For example, the reference longitudinal and lateral slip values resulting from the DIA could be used for estimating the self-aligning moment of the tyre, which acts as a disturbance torque on the positioning of the steer actuator.

Tyre model For the implementation of the DIA in the dSPACE real-time environment, the linear combined tyre model has been used for the control model. Besides the limited operating range of the linear tyre model, the absence of the peak friction curve in the force/slip-characteristic has a negative influence on the convergence of the optimization process. In the simulated steady-state manoeuvring it is found that the upper (or lower) saturation bound in the non-linear force/slip-characteristic acts as a constraint on the tyre force, e.g. control saturation, when implemented in the control model. Because of it, the convergence of the optimization process is guaranteed to be more robust for non-smooth reference trajectories. Therefore, the implementation of the non-linear combined tyre model in the real-time DIA is strongly recommended.

Sample rate The final recommendation concerning the real-time implementation is the possibility to increase the sample frequency beyond the $400\,Hz$. Initial results show that the algorithm is capable of running at a sample frequency of $750\,Hz$ on the dSPACE 1005 environment. Doing so allows for a higher cut-off frequency for the sensor noise filtering. On the other hand, the margin on the unused execution time during a sample interval could allow the implementation of the combined non-linear tyre model in the DIA.

Feedback information The use of the measured orientation angle $\psi_m(t)$ instead of the reference vehicle orientation angle $\psi_{ref}(t)$ in the implementation of the DIA would result in a more realistic feedforward compensation of the wheel slip. However, since the measured vehicle orientation angle is subjected to measurement errors it could just as well de-stabilize the algorithm.

Friction estimator In the current tyre modelling, the tyre model parameters are not validated with the road surface in the VEHIL laboratory. The use of a Kalman filter for the estimation of the longitudinal and lateral friction levels in the steady-state force/slip-characteristics of the tyre is recommended in order to obtain a more accurate modelling.

Bibliography

[1] B.D'Andrea-Novel , G.Campion and G Bastin, Modelling and control of Nonholonomic Wheeled Mobile Robots, in Proc. Of the 1991 IEEE International Conference on Robotics and Automation, p1130-1135, 1991.

[2] ATSCAR, a Matlab Simulink library for vehicle simulations developed by TNO Automotive, department of Advanced Chassis and Transport Systems, section NTS, 2001. The original designers are A.C.M. Knaap, J. Ploeg and D.J. van der Verburg.

[3] J.C.Alexander and J.H.Maddocks, On the Kinematics of Wheeled Mobile Robots, int. J. Robotics Res., vol. 8, no. 5, October 1989.

[4] R.Balakrishna, A. Ghosal, Modeling of Slip for Wheeled Mobile Robots, IEEE Transactions on Robotics and Automation, vol.11, no.1, February 1995, p126-132.

[5] J.D.Bendtsen, P.Andersen and T.S.Pedersen, Robust Feedback Linearization-based Control Design for a Wheeled Mobile Robot, Department of Control Engineering, Aalborg University, 2002,
http://www.cs.auc.dk/~api/Referencer/mat/dimon.pdf

[6] G.Campion, G Bastin and B.D'Andrea-Novel Structural Properties and Classification of Kinematic and Dynamic Models of Wheeled Mobile Robots, IEEE Transactions on Robotics and Automation, vol. 12, no. 1 p47-62, February 1996.

[7] Carlos.C. de Wit, Bruno Siciliano and Georges Bastin (Eds), Theory of Robot Control, chapter 9, Springer 1996.

[8] Carlos.C. de Wit, Panagiotis Tsiotras, Dynamic Tire Friction Models for Vehicle Traction Control, American Control Conference, Philadelphia, June 1998.

[9] Davison, E.J., and Goldenberg, A., Robust control of a general servomechanism problem: the servo compensator, Automatica, 11, nr. 5, p461-471, 1975.

[10] Heath, M.T., Scientific computing, an introductory survey, second edition, McGraw-Hill, 2002, p 279.

[11] Maurice, J.P., Short wavelength and dynamic tyre behaviour under lateral and combined slip conditions, PhD thesis, Technical University Delft, 2000.

[12] Pacejka, H.B., Tyre and vehicle dynamics, Butterworth-Heinemann, ISBN 0 7506 5141 5, 2002.

[13] Ploeg, J., Knaap, A.C.M. van der., Verburg, D.J., ATS/AGV - Design, Implementation and Evaluation of a High Performance AGV, Proceedings IEEE Intelligent Vehicle Symposium IV 2002, Versailles, France, June 18-20, 2002.

[14] B.Thuilot, B.d'Andrea-Novel and A.Micaelli, Modelling and Feedback Control of Mobile Robots with several steering wheels, IEEE Transactions on Robotics and Automation, vol.12, no.3, June 1996, p375-390.

[15] Verburg, D.J., Ploeg, J., Knaap, A.C.M. van der., VEHIL - Developing and Testing Intelligent Vehicles, Proceedings IEEE Intelligent Vehicle Symposium IV 2002, Versailles, France, June 18-20, 2002.

[16] Zegelaar, P.W.A., The Dynamic Response of Tyres to Brake Torque Variations and Road Unevennesses, PhD Thesis, Delft University of Technology, The Netherlands, 1998.

[17] TNO workdocument, werkpakket 02:Regeling en Simulatie.

Appendix A

Technical specifications of the ATS/AGV

ATS/AGV is a robot vehicle that responds to position commands issued by the VEHIL experiment controller [15, 13]. In order to carry out the desired manoeuvres, ATS/AGV requires the independent control of its position in x- and y-direction, as well as its yaw angle ψ. Such manoeuvring flexibility is accomplished through a vehicle platform equipped with independent all-wheel steering, and consequently independent all-wheel drive, as depicted in figure A.1. This figure illustrates the platform's capability of motion in x-direction (a), crab-like motion in y-direction (b), pure rotation around its center of gravity (c) as well as any combination of these types of motion, i.e. rotation around a momentary pole P (d).

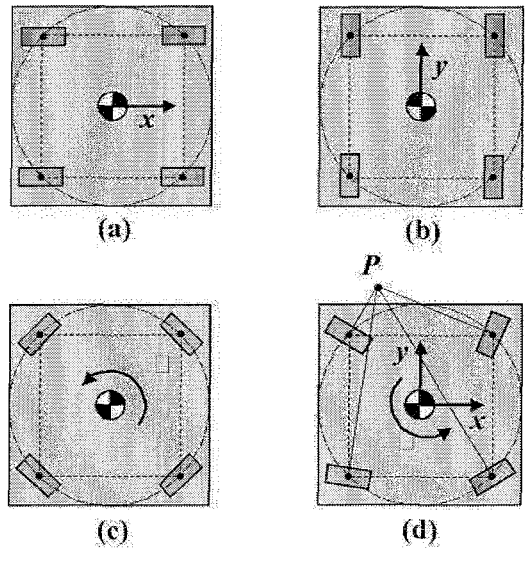

Figure A.1: Types of motion with three degrees of freedom.

In practice, an emergency stop of a passenger vehicle corresponds to a maximum of

10 $[m/s^2]$ deceleration. As a consequence, the AGV is capable of accelerating with 10 $[m/s^2]$ in order to simulate an emergency stop in the VEHIL experiment. The dynamic manoeuvring behavior of conventional passenger cars can be described in terms of yaw response to steer inputs and speed response to throttle/brake input. The corresponding transfer functions typically show a bandwidth in the 1 $[Hz]$ frequency range. This implies that the ATS/AGV must at least have a bandwidth of about 5 $[Hz]$ in order to minimize positioning phase lag. Finally the top speed, which in view of the relative VEHIL world corresponds to the maximum speed difference between the Vehicle Under Test and the ATS/AGV as a Moving Base, should at least be equal to 50 $[Km/h]$. These additional traction and handling performance requirements are accomplished using four high power brushless DC servomotors for generating the traction forces and four additional brushless DC servomotors controlling the steer angles in a range of $-350deg$ till $350deg$.
All electrical drives are of a servo disc type, allowing a compact design with a high torque/weight ration. Special attention has been paid to the design of a light weight aluminium space frame vehicle chassis with the center of gravity located close to the ground surface. The on-board energy is provided by a battery package consisting of 288 NiMH D-cells. Table H.1 lists the main ATS/AGV specifications.

vehicle mass	487 kg
wheel base	1.4 m
track width	1.4 m
maximum speed	50 km/h
maximum acceleration	10 m/s^2
battery power	30 kW
acceleration from 0 to 50 km/h	2.1 s

Table A.1: Specifications of ATS/AGV

Figure H.1 shows the ATS/AGV. Note that there is no wheel suspension and that the four formula SAE race tyres are directly connected to the chassis.

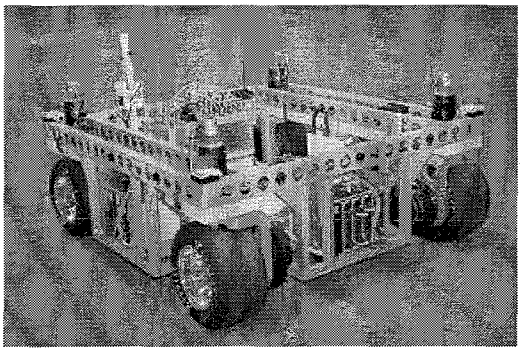

Figure A.2: The ATS/AGV

ATS/AGV is essentially a positioning device that responds to open loop position reference commands. The reference position coordinates $x_{g,ref}$, $y_{g,ref}$ and ψ_{ref} are defined with respect to a fixed global reference frame. The reference trajectory, plus first and second order derivatives, are provided on a samplewise basis, since the complete reference trajectory of the vehicle is not known on forehand in the VEHIL experiment. These reference signals are communicated to the ATS/AGV by wireless ethernet. The actual position coordinates x_g, y_g and ψ are estimated by the use of a Kalman filter, combining position and speed information obtained from a magnet grid, acceleration sensors, steer angle and wheel rotational velocity encoders, and a gyro for measuring the angular velocity in the center of gravity of the vehicle. In this work, it is assumed that the estimated values for x_g, y_g and ψ correspond to the true values.

Appendix B

Wheel corner velocities

The wheel corner velocities for the front left wheel read

$$\nu_{x,1L} = v_x - S_f/2 \cdot \dot{\psi} \tag{B.1}$$
$$\nu_{y,1L} = v_y + L_f \cdot \dot{\psi} \tag{B.2}$$

front right wheel,

$$\nu_{x,1R} = v_x + S_f/2 \cdot \dot{\psi} \tag{B.3}$$
$$\nu_{y,1R} = v_y + L_f \cdot \dot{\psi} \tag{B.4}$$

rear left wheel,

$$\nu_{x,2L} = v_x - S_r/2 \cdot \dot{\psi} \tag{B.5}$$
$$\nu_{y,2L} = v_y - L_r \cdot \dot{\psi} \tag{B.6}$$

and rear right wheel,

$$\nu_{x,2R} = v_x + S_r/2 \cdot \dot{\psi} \tag{B.7}$$
$$\nu_{y,2R} = v_y - L_r \cdot \dot{\psi} \tag{B.8}$$

with the velocities in the center of gravity

$$\begin{bmatrix} v_x \\ v_y \end{bmatrix} = \begin{bmatrix} \cos(\psi) & \sin(\psi) \\ -\sin(\psi) & \cos(\psi) \end{bmatrix} \cdot \begin{bmatrix} \dot{x}_g \\ \dot{y}_g \end{bmatrix} \tag{B.9}$$

Appendix C

Fundamental tyre behavior

In this chapter, some fundamentals of the tyre/road contact behavior are explained in more detail. The forces that mainly determine the dynamics of a vehicle are generated by the tyres. The tyre therefore plays a very important role in this study.
In figure C.1 a side and top view of one of the wheels of the ATS/CAR is drawn. The left part (side view) shows the construction parts of the wheel and its rotational velocity ω. The center of the rim is located at a distance above the road surface, which is defined by the loaded tyre radius R_l. The slip point S is introduced. The distance of point S to the wheel center is defined as the effective rolling radius R_e. In general, the effective rolling radius is larger than the loaded tyre radius but smaller than the unloaded tyre radius. This imaginary point S is attached to the wheel rim and moves parallel to the road surface with a velocity of $\omega \cdot R_e$. The wheel slip is then defined to be the difference between the velocity in point S and the velocity of the wheel's center of rotation, $\nu_{w,x}$ and $\nu_{w,y}$ for the longitudinal and lateral wheel direction, respectively. The forces and moments in the horizontal plane are the longitudinal force F_x, the lateral force F_y and the aligning torque M_z which act on the tyre at the contact patch between the tyre tread and the road surface. The wheel load is denoted as F_z. In the right side of figure C.1 a schematic depiction of the tyre forces is shown. These forces are generated by the tyre deflections at the tyre contact patch, which are generated by the wheel slip.
The wheel's center of rotation is travelling with the planar velocity ν_w, which can be decomposed into a longitudinal velocity $\nu_{w,x}$ and a lateral velocity $\nu_{w,y}$. The slip velocity in the slippoint S is ν_s with the longitudinal and lateral components ν_{sx} and ν_{sy}, respectively. The slip velocity components are defined as

$$\nu_{sx} = R_e \cdot \omega - \nu_{w,x} \tag{C.1}$$

$$\nu_{sy} = -\nu_{w,y} \tag{C.2}$$

The longitudinal steady-state slip κ_{ss} is defined as the ratio of the longitudinal slip velocity ν_{sx} and the absolute longitudinal velocity $|\nu_{w,x}|$ in the wheel center [12].

$$\kappa_{ss} = \frac{\nu_{sx}}{|\nu_{w,x}|} = \frac{R_e \cdot \omega - \nu_{w,x}}{|\nu_{w,x}|} \tag{C.3}$$

Equivalently, the steady-state lateral slip α_{ss} is defined as the tangent of the angle between the tyre longitudinal axis and the direction of motion of the wheel center, as

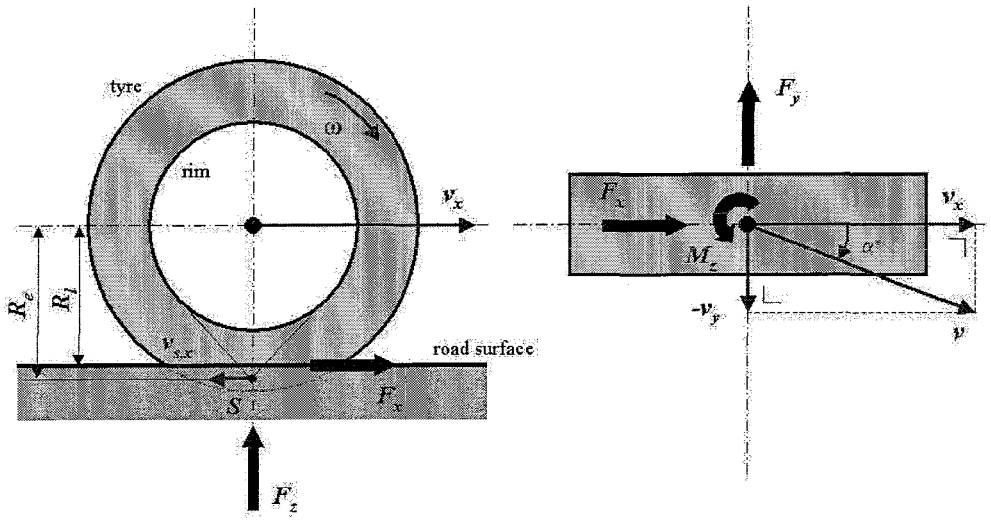

Figure C.1: The forces acting in the contact patch of a slipping tyre during accelerating and cornering

shown in figure C.1.

$$\alpha_{ss} = \tan(\alpha*) = \frac{\nu_{sy}}{|\nu_{w,x}|} \tag{C.4}$$

With these definitions, the relationship between the generated tyre force as a function of the slip can be examined. The steady-state tyre behavior as well as the dynamic characteristics will be examined in section C.1 and C.2, respectively.

C.1 Steady-state behavior

The steady-state force generation of the tyre is highly non-linear with respect to slip. Figure C.2 shows typical diagrams of tyre forces under pure longitudinal and lateral slip conditions, respectively. It can be seen that the tyre has the characteristic that for small values of slip the force generation is approximately proportional to the slip. As the slip increases the force reaches a point of saturation after which it declines. In the modelled force/slip-curves the longitudinal force reaches this point of saturation at approximately 0.06 slip, i.e. a slip percentage of 6%. For the lateral force the maximum is reached at an approximately 7 deg (= $atan(\alpha)$) slip angle. One can see that the shape of the curves show a similar behavior for the longitudinal and lateral direction. The slopes of the curves in the linear region of the characteristic are denoted as c_κ and c_α for the longitudinal and lateral direction, respectively. The longitudinal and lateral friction coefficients μ_x and μ_y are the relationships between the tyre forces F_x and F_y respectively and the vertical tyre load F_z.

$$\mu_x = \frac{F_x}{F_z} \tag{C.5}$$

$$\mu_y = \frac{F_y}{F_z} \tag{C.6}$$

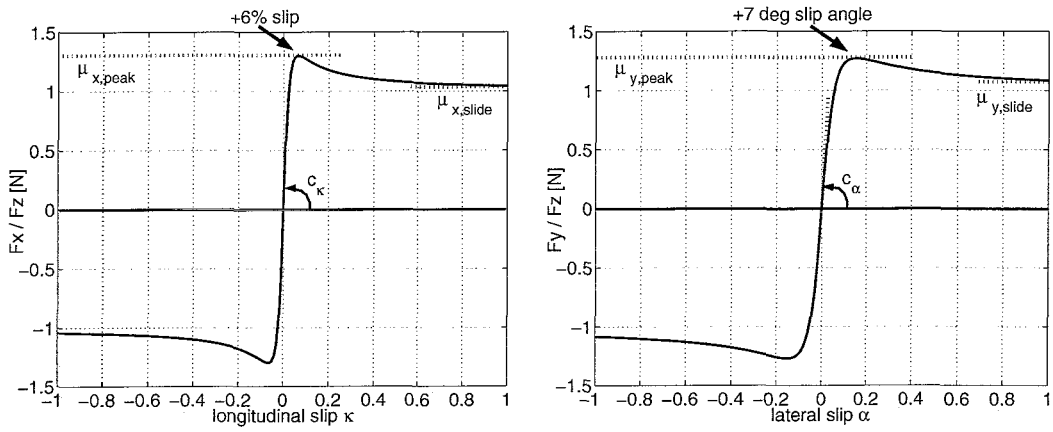

Figure C.2: Typical force/slip characteristics; (left) pure longitudinal (right) pure lateral. Both curves are normalized with respect to the vertical wheel load F_z

The maximum longitudinal and lateral friction coefficients $\mu_{x,peak}$ and $\mu_{y,peak}$ (also shown in figure C.2) determine the maximum level of friction in the corresponding direction.

The longitudinal force generation is influenced by lateral slip and vice versa. This effect can be seen clearest by examining the longitudinal and the lateral forces for simultaneous longitudinal and lateral slip. This is denoted as combined slip. A typical example of such curves is shown in figure C.3. The slip angle $\alpha*$ is kept constant and the longitudinal slip κ is varied from -1 to 1. The lateral force F_y is maximal when no longitudinal slip is present and with increasing longitudinal slip, either brake or drive, the lateral force declines. This is for example why it is not preferable to brake during a cornering manoeuvre of the tyre. The figure also shows that the maximum achievable force is relatively independent of the direction of the force. In other words, if the force on the tyre is a vector then this vector will remain within the friction circle depicted in the right side of figure C.3. The use of a circle is a simplification, in practice it will be more elliptically shaped in the longitudinal direction. Thus, if a tyre is running at the maximum of lateral force, then the addition of longitudinal slip will cause the resulting force vector to rotate around the tyre contact patch, practically without changing the magnitude of the force (radius of friction circle).
Another important aspect in the behavior of the tyre is the influence of the vertical wheel load F_z. The basic Coulomb friction law states that the maximum friction force is proportional to the friction coefficient multiplied by the load between the two surfaces. However, in practice, the tyre behavior also has non-linearities in this respect. Both longitudinal and lateral friction coefficients μ_x and μ_y are a function of the wheel load. Because the mass of the ATS/AGV is constant and the weight transfer is limited during cornering and/or driving, the friction level μ_x is assumed to be proportional to the wheel load. While in reality, the lateral slip stiffness c_{alpha} is actually a function of the vertical wheel load F_z, it is in this study assumed that μ_y is also proportional to

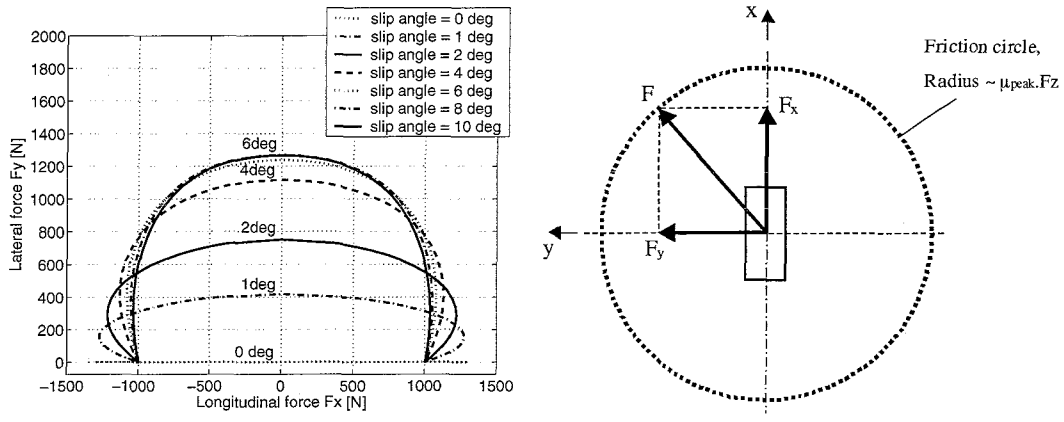

Figure C.3: (left) Force diagram of the tyre forces for combined longitudinal and lateral slip ($\kappa \in [-1, 1]$, $F_z = 1kN$). (right) Schematic depiction of the tyre from the top with a friction circle.

the vertical wheel load F_z (see the right side of figure C.4). Furthermore, it is assumed that the lateral slip stiffness c_α is independent of the vertical wheel load.

For modelling the non-linear tyre characteristics an empirical tyre model, the Magic Formula, is chosen. This model is based on a set of mathematical expressions, with coefficients that are strongly related to the physical tyre properties (friction level, slip stiffness, etc.), representing the experimental data. The advantage of using such an empirical model is that it can give an accurate representation of the experimental data and it is computationally fast. The Magic Formula was first presented in 1987 by Bakker et al. and the latest version was published in 1996 by Pacejka [12]. The Magic Formula, as presented in [12], has an enormous amount of parameters to describe the load, camber, ply-steer and friction dependencies of its coefficients. In this study, the most basic shape of the Magic Formula is used which has a minimum number of tunable parameters. Nevertheless, the simplified model is suitable for the description of the tyre behavior up till peak slip values of the force/slip characteristic. The force/slip behavior at levels of slip larger than the peak slip values is not relevant for the research done in this study. The general shape of this simplified Magic Formula for describing the pure slip characteristics is a sine function with a tangent as an argument:

$$F = D \sin(C \arctan(Bx)) \tag{C.7}$$

Where x denotes the slip value κ or α. The coefficients B,C and D characterize the shape of the force/slip characteristic. Together they represent the slip stiffness c_x ($= B \cdot C \cdot D$), which coincides with the slope of the characteristic at low values of slip. To simplify the tuning of the tyre model, the three tyre model coefficients are related to three tunable parameters; the slip stiffness c_x, the peak friction coefficient $\mu_{x,peak}$ and the location of the peak slip value x_{peak}. Figure C.4 shows a pure slip characteristic with the three minimum required parameters for describing the steady-state tyre behavior. A fourth parameter for describing the slip characteristic, $\mu_{x,slide}$, is

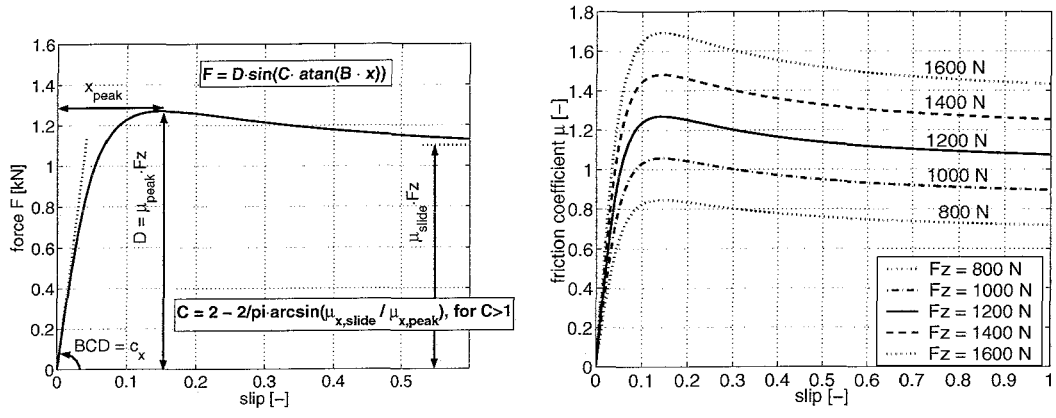

Figure C.4: (left) Input parameters for defining the shape of the pure tyre slip characteristics. (right) wheel load dependency of the friction level (the curves are normalized with respect to the vertical load F_z)

irrelevant for the control design proces because it lies out of the region of interest and is therefore not discussed in any further detail. The only requirement for the control design is that its value must be substantially lower than the value of $\mu_{x,peak}$, both in longitudinal and lateral direction.
As stated, the magnitude of the tyre forces is strongly dependent on the vertical wheel load F_z. Therefore the normalized slip characteristic is introduced which is merely a division of the tyre force F by the vertical wheel load F_z. The normalized characteristic is merely an approximation but well accepted in literature by Pacejka et al. [12, 11]. The normalized tyre model coefficients are denoted with the norm subscript. The result is that as an approximation the tyre behavior can be modelled with only one curve in longitudinal and lateral direction.

Summarizing, the non-linear steady-state combined longitudinal tyre force F_x and lateral tyre force F_y, both with the longitudinal slip κ and lateral slip α as input, are given by

$$F_x(\kappa, \alpha, F_z) = G(\kappa, \alpha)_x \cdot F_{x,norm,0}(\kappa) \cdot F_z \quad \text{(C.8)}$$

$$F_y(\kappa, \alpha, F_z) = G(\kappa, \alpha)_y \cdot F_{y,norm,0}(\alpha) \cdot F_z \quad \text{(C.9)}$$

in which $G(\kappa, \alpha)_x$ and $G(\kappa, \alpha)_y$ are the weight functions for the interaction of the longitudinal and lateral slip. $F_{x,norm,0}$ and $F_{y,norm,0}$ are the normalized tyre forces, derived from (C.7), at pure longitudinal and lateral slip, respectively.

C.2 Transient behavior

The influence of transient tyre behavior on the vehicle longitudinal and lateral dynamics can be quite large, especially for low vehicle velocities. It is well known that the force and moment responses of the tyre to various external inputs show a lag in time.

The fact that the tyre deflections (deflections of tyre side walls, carcass and rubber thread) have to be built up to create a force calls for a model that contains carcass compliance. For this purpose the relaxation length phenomenon is introduced. Higher frequent dynamics or tyre oscillations will be neglected. The rolling distance required to build up traction force is called the relaxation length σ. The relaxation length of a tyre depends on the tyre construction. An average value for the relaxation length of a passenger car tyre with nominal wheel load is $0.5m$ which corresponds to $0.04s$ at $50km/h$. The time lag in developing the traction force is also dependent on the speed of travelling in longitudinal wheel direction $\nu_{w,x}$ and the magnitude of the slip. In the automotive literature it is most common to describe the transient tyre behavior with a first-order lowpass filter with time constant equal to $\sigma/\nu_{w,x}$. Because of numerical difficulties it is more convenient to filter the slip rather than the tyre force [16]. This gives for the longitudinal slip dynamics

$$\sigma(\kappa)\cdot\dot{\kappa}+|\nu_{w,x}|\cdot\kappa=R_e\cdot\omega-\nu_{w,x}\quad\rightarrow\quad\frac{\kappa(s)}{\kappa_{ss}(s)}=\frac{1}{\frac{\sigma(\kappa)}{\|\nu_{w,x}\|}s+1} \tag{C.10}$$

and

$$\sigma(\alpha)\cdot\dot{\alpha}+|\nu_{w,x}|\cdot\alpha=-\nu_{lat}\quad\rightarrow\quad\frac{\alpha(s)}{\alpha_{ss}(s)}=\frac{1}{\frac{\sigma(\alpha)}{\|\nu_{w,x}\|}s+1} \tag{C.11}$$

for the lateral slip dynamics. A variation of the slip velocity ν_{sx} or ν_{sy} will generate through differential equation (C.10) and (C.11) a transient slip, which is used as an input to the slip characteristics (C.8) and (C.9). From the time constant of the first-order filters in (C.10) and (C.11) it can be concluded that when $\nu_{w,x}\rightarrow 0$ the slip dynamics get a pure integral behavior, e.g. a poor initial response behavior. The influence of the vertical wheel load on the transient behavior of the tyre is neglected by this first-order filter. This means that a variation in the vertical wheel load at constant slip will generate a direct (non-delayed) response of the tyre force. Therefore, this model is not suitable for simulations where fast changes in vertical load occur.

Appendix D

Linearization of the quarter car model

The analysis of the non-linear dynamics of the drive actuator is done by linearizing the equations of motion, represented by (3.16a) till (3.16d), in a work-point with velocity v_0 and relaxation length σ_0 under the following model features:
1. The behavior of the tyre is assumed linear. The force F is thus assumed proportional to the wheel slip κ where the stiffness c_x is the proportional gain.

$$F = c_x \cdot \kappa \tag{D.1}$$

2. The relaxation length σ is assumed to be a constant. In reality, the relaxation length is a function of the slip value with a range of approximately $0.42m$ for zero wheel slip till a minimum of $0.03m$ for larger wheel slip values.
3. The velocity v is also assumed constant with a parametric range of $0 - 50km/h$.
4. The wheel slip remains small.

The equations of motion, linearized in work-point v_0 and σ_0, are formulated in state-space form with three states: the wheel slip κ, the wheel rotational velocity ω and the distributed drive torque T_d resulting from the electrical actuator. u_d is the system input.

$$\begin{bmatrix} \dot{\kappa} \\ \dot{\omega} \\ \dot{T}_d \end{bmatrix} = \begin{bmatrix} -\frac{|v_0|}{\sigma_0} & \frac{R_e}{\sigma_0} & 0 \\ -\frac{R_e c_x}{J_w} & -\frac{B_w}{J_w} & \frac{i_{drv}}{J_w} \\ 0 & 0 & -\frac{1}{\tau_d} \end{bmatrix} \begin{bmatrix} \kappa \\ \omega \\ T_d \end{bmatrix} + \begin{bmatrix} 0 \\ 0 \\ \frac{1}{\tau_d} \end{bmatrix} u_d \tag{D.2}$$

$$y = F = c_x \kappa$$

With this linearized model, important steady-state characteristics of the vehicle can be analyzed in order to get a better understanding of the vehicle's behavior. The frequency characteristics of the linearized model are presented in figure D.1 were derived. It can be concluded that the system dynamics are highly dependent on the velocity v and the tyre relaxation length σ. In the left graph, the curves of a varying velocity $v = 0, 5, 10, 20, 40km/h$ are plotted with the tyre relaxation length

$\sigma = 0.03$ as a constant and in the right graph, the curves of a varying relaxation length $\sigma = 0.03, 0.1, 0.2, 0.3, 0.42$ are plotted with the velocity $v = 0km/h$ as a constant. For higher velocities the drive actuator shows a reasonable damped behavior. However, when the velocity is near zero the system shows a weak damped behavior. The same holds for the bandwidth of the uncontrolled system, which decreases at higher velocities and/or larger relaxation length values. It is clear that for the non-linear system these parameters are time-varying and therefore cause a complex non-linear multivariable behavior which is rather difficult to analyse.

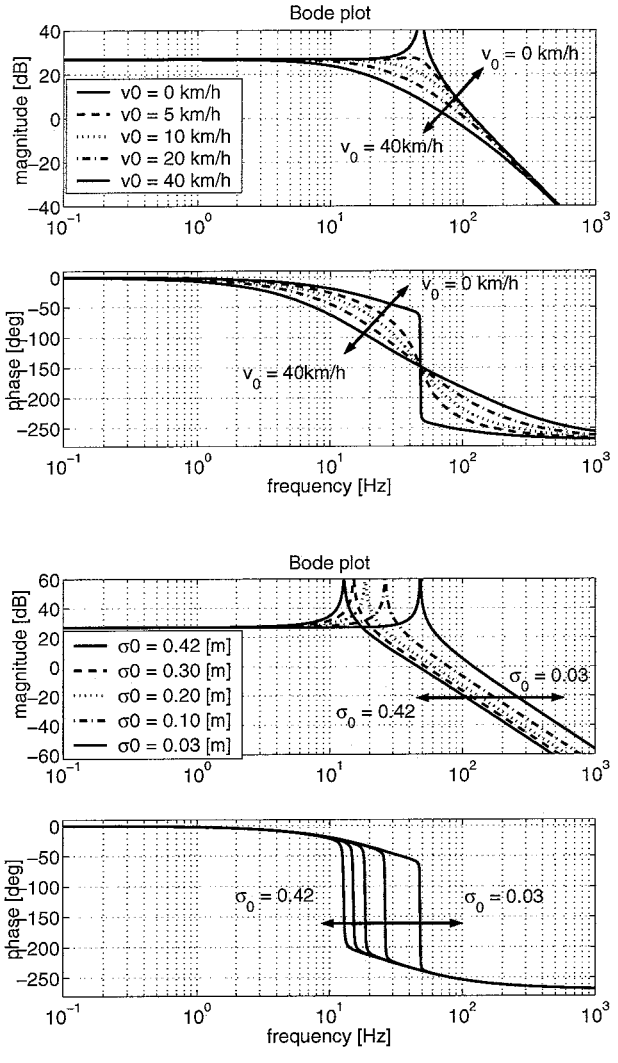

Figure D.1: Frequency response characteristics of the linearized quarter car model (D.2); Varying velocity v_0 (top), varying relaxation length σ_0 (bottom), $F_z = mg/4\,[N]$.

Appendix E

Equations of motion of the two-track model

The equations of motion for the two-track planar vehicle model are in longitudinal vehicle direction,

$$m \cdot \dot{v}_x = m v_y \dot{\psi} + \sum F_{long} \quad [N] \tag{E.1}$$

$$\begin{aligned} \sum F_{long} = & \left(\sum_{i=1,2}^{j=L,R} F_{x,ij} \cos(\delta_{ij}) - \sum_{i=1,2}^{j=L,R} F_{y,ij} \sin(\delta_{ij}) \right) \\ = & F_{x,1L} \cdot \cos(\delta_{1L}) + F_{x,1R} \cdot \cos(\delta_{1R}) \\ & + F_{x,2L} \cdot \cos(\delta_{2L}) + F_{x,2R} \cdot \cos(\delta_{2R}) \\ & - F_{y,1L} \cdot \sin(\delta_{1L}) - F_{y,1R} \cdot \sin(\delta_{1R}) \\ & - F_{y,2L} \cdot \sin(\delta_{2L}) - F_{y,2R} \cdot \sin(\delta_{2R}) \end{aligned} \tag{E.2}$$

and lateral vehicle direction,

$$m \cdot \dot{v}_y = -m v_x \dot{\psi} + \sum F_{lat} \quad [N] \tag{E.3}$$

$$\begin{aligned} \sum F_{lat} = & \left(\sum_{i=1,2}^{j=L,R} F_{x,ij} \sin(\delta_{ij}) + \sum_{i=1,2}^{j=L,R} F_{y,ij} \cos(\delta_{ij}) \right) \\ = & F_{x,1L} \cdot \sin(\delta_{1L}) + F_{x,1R} \cdot \sin(\delta_{1R}) \\ & + F_{x,2L} \cdot \sin(\delta_{2L}) + F_{x,2R} \cdot \sin(\delta_{2R}) \\ & + F_{y,1L} \cdot \cos(\delta_{1L}) + F_{y,1R} \cdot \cos(\delta_{1R}) \\ & + F_{y,2L} \cdot \cos(\delta_{2L}) + F_{y,2R} \cdot \cos(\delta_{2R}) \end{aligned} \tag{E.4}$$

and angular rotation

$$I_z \cdot \ddot{\psi} = M \quad [Nm] \tag{E.5}$$

$$
\begin{aligned}
M = \; & L_F \cdot (F_{x,1L} \cdot \sin(\delta_{1L}) + F_{y,1L} \cdot \cos(\delta_{1L})) \\
& -\frac{1}{2} \cdot S_F \cdot (F_{x,1L} \cdot \cos(\delta_{1L}) - F_{y,1L} \cdot \sin(\delta_{1L})) \\
& +L_F \cdot (F_{x,1R} \cdot \sin(\delta_{1R}) + F_{y,1R} \cdot \cos(\delta_{1R})) \\
& +\frac{1}{2} \cdot S_F \cdot (F_{x,1R} \cdot \cos(\delta_{1R}) - F_{y,1R} \cdot \sin(\delta_{1R})) \\
& -L_R \cdot (F_{x,2L} \cdot \sin(\delta_{2L}) + F_{y,2L} \cdot \cos(\delta_{2L})) \\
& -\frac{1}{2} \cdot S_R \cdot (F_{x,2L} \cdot \cos(\delta_{2L}) - F_{y,2L} \cdot \sin(\delta_{2L})) \\
& -L_R \cdot (F_{x,2R} \cdot \sin(\delta_{2R}) + F_{y,2R} \cdot \cos(\delta_{2R})) \\
& +\frac{1}{2} \cdot S_R \cdot (F_{x,2R} \cdot \cos(\delta_{2R}) - F_{y,2R} \cdot \sin(\delta_{2R}))
\end{aligned} \tag{E.6}
$$

The combined longitudinal and lateral tyre forces as a function of the slip values κ_{ij} and α_{ij} are (see section 3.1.2)

$$
\begin{aligned}
F_{x,ij} &= G(\alpha_{ij}, \kappa_{ij})_x \cdot B_{x,norm} \sin(C_{x,norm} \arctan(B_{x,norm} \cdot \kappa_{ij})) F_{z,ij} \\
F_{y,ij} &= G(\alpha_{ij}, \kappa_{ij})_y \cdot B_{y,norm} \sin(C_{y,norm} \arctan(B_{y,norm} \cdot \alpha_{ij})) F_{z,ij}
\end{aligned}
$$

and L_F, L_R, S_F and S_R are the characteristic chassis dimensions. The time element is omitted from the notations.

Appendix F

Vertical wheel load estimates

The vertical load $F_{z,ij}$ on each wheel is a function of both the vehicle's static weight and the dynamic weight transfer associated with the longitudinal acceleration a_x and the lateral acceleration a_y in the center of gravity. The longitudinal acceleration affects the normal loading in the vehicle pitch mode, while the lateral acceleration affects the normal loading through the vehicle roll motion. Although the pitch and roll motions are not included in the vehicle model, their effect on the normal tyre forces is estimated. The center of gravity of the vehicle lies $h = 0.35m$ above the road surface. Figure F.1 gives a schematic depiction of the pitch and roll motion of the vehicle.

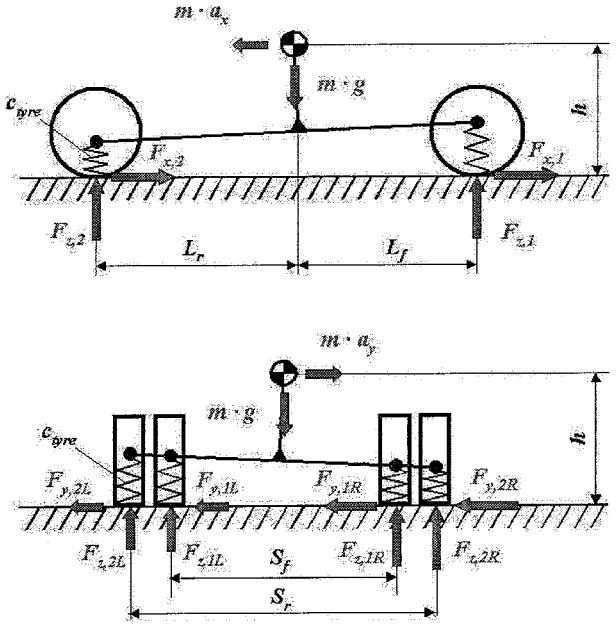

Figure F.1: (top) Weight transfer in pitch mode due to longitudinal acceleration . (bottom) Weight transfer in roll mode due to lateral acceleration.

The wheel loads are calculated with the following estimates

$$\begin{aligned} F_{z,1L} &= \frac{mg}{4} - \frac{m}{2} \cdot \frac{h}{L_F + L_R} \cdot a_{filt,x} - mh \cdot \frac{S_F}{S_F^2 + S_R^2} \cdot a_{filt,y} \\ &= F_{mg,11} - H_{pitch}(s) \cdot a_x - H_{roll}(s) \cdot a_y \qquad \text{(F.1)} \\ F_{z,1R} &= \frac{mg}{4} - \frac{m}{2} \cdot \frac{h}{L_F + L_R} \cdot a_{filt,x} + mh \cdot \frac{S_F}{S_F^2 + S_R^2} \cdot a_{filt,y} \\ &= F_{mg,12} - H_{pitch}(s) \cdot a_x + H_{roll}(s) \cdot a_y \qquad \text{(F.2)} \\ F_{z,2L} &= \frac{mg}{4} + \frac{m}{2} \cdot \frac{h}{L_F + L_R} \cdot a_{filt,x} - mh \cdot \frac{S_F}{S_F^2 + S_R^2} \cdot a_{filt,y} \\ &= F_{mg,21} + H_{pitch}(s) \cdot a_x - H_{roll}(s) \cdot a_y \qquad \text{(F.3)} \\ F_{z,2R} &= \frac{mg}{4} + \frac{m}{2} \cdot \frac{h}{L_F + L_R} \cdot a_{filt,x} + mh \cdot \frac{S_F}{S_F^2 + S_R^2} \cdot a_{filt,y} \\ &= F_{mg,22} + H_{pitch}(s) \cdot a_x + H_{roll}(s) \cdot a_y \qquad \text{(F.4)} \end{aligned}$$

The dynamic behavior of the weight transfer estimates is approached by applying the second order filters $H_{pitch}(s)$ and $H_{roll}(s)$ to the longitudinal and lateral acceleration of the center of gravity, respectively. The undamped eigenfrequencties are chosen such that they correlate with the tyre stiffnesses and vehicle inertia masses [17]. The damping is deliberately chosen too high in order to compensate for the poor signal/noise ratio of the measured acceleration. In reality, tyres do have very little damping properties. The frequency response characteristics of the filters including the static gains are plotted in figure F.2 for respectively the pitch mode and the roll mode.

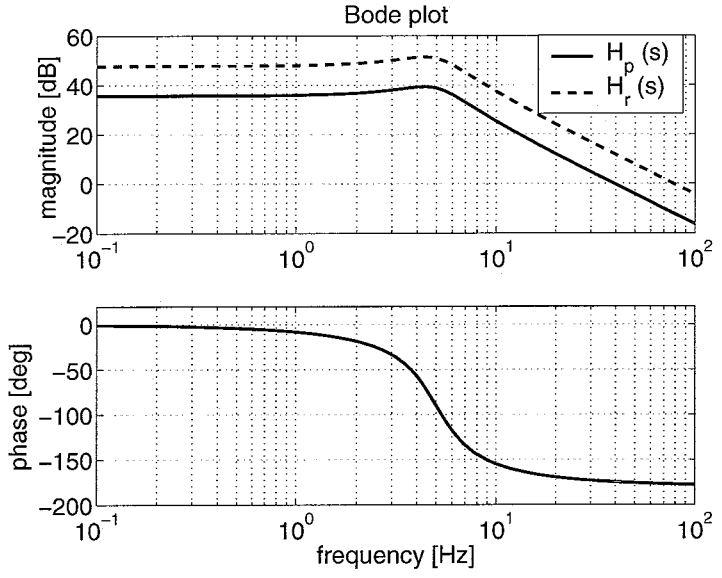

Figure F.2: Frequency response of the weight transfer filters $H_{pitch}(s)$ in pitch mode and $H_{roll}(s)$ in roll mode.

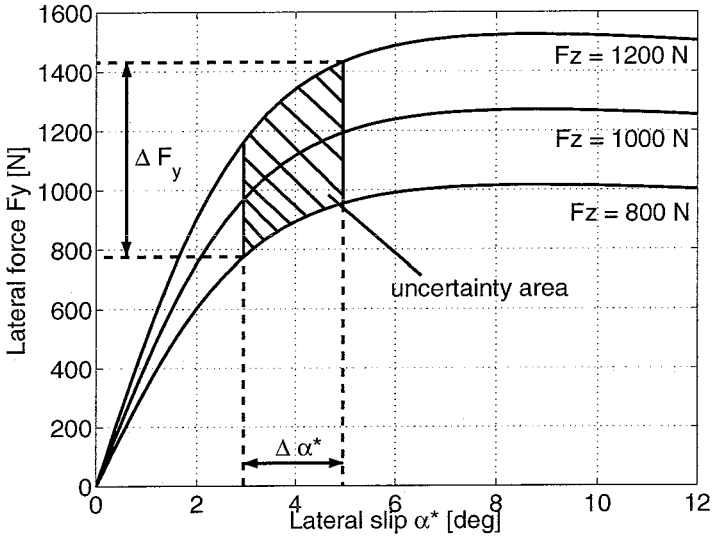

Figure F.3: Illustration of the tyre force uncertainty.

Figure F.3 illustrates the tyre force uncertainty ΔF_y induced by a mismatch between the estimated and the real vertical wheel load or an offset in the achieved amount of slip $\Delta\alpha*$, which is caused by either a tracking error or an inaccurate velocity estimate in the control of the wheel rotational velocity. The shaded area in the graph represents the uncertainty area. It can be concluded that the estimated vertical wheel load, as well as the accuracy of the obtained slip value, play a crucial role in describing the dynamic behavior of the tyre, and thereby the vehicle model as a whole.

Appendix G

Control model

The force and momentum equilibrium equations in the objective function are entirely based on reference value information. The time element is omitted from the notations. In longitudinal direction they read:

$$\sum F_{p1} = \left(\sum_{i=1,2}^{j=L,R} F_{x,ij} \cos(\delta_{ij} - \beta_{ref}) - \sum_{i=1,2}^{j=L,R} F_{y,ij} \sin(\delta_{ij} - \beta_{ref}) \right) \quad [N] \quad \text{(G.1)}$$

$$\begin{aligned} \sum F_{p1} = \; & F_{x,1L} \cdot \cos(\delta_{1L} - \beta_{ref}) + F_{x,1R} \cdot \cos(\delta_{1R} - \beta_{ref}) \\ & + F_{x,2L} \cdot \cos(\delta_{2L} - \beta_{ref}) + F_{x,2R} \cdot \cos(\delta_{2R} - \beta_{ref}) \\ & - F_{y,1L} \cdot \sin(\delta_{1L} - \beta_{ref}) - F_{y,1R} \cdot \sin(\delta_{1R} - \beta_{ref}) \\ & - F_{y,2L} \cdot \sin(\delta_{2L} - \beta_{ref}) - F_{y,2R} \cdot \sin(\delta_{2R} - \beta_{ref}) \end{aligned} \quad \text{(G.2)}$$

and in lateral direction:

$$\sum F_{p2} = \left(\sum_{i=1,2}^{j=L,R} F_{x,ij} \sin(\delta_{ij} - \beta_{ref}) + \sum_{i=1,2}^{j=L,R} F_{y,ij} \cos(\delta_{ij} - \beta_{ref}) \right) \quad [N] \quad \text{(G.3)}$$

$$\begin{aligned} \sum F_{p2} = \; & F_{x,1L} \cdot \sin(\delta_{1L} - \beta_{ref}) + F_{x,1R} \cdot \sin(\delta_{1R} - \beta_{ref}) \\ & + F_{x,2L} \cdot \sin(\delta_{2L} - \beta_{ref}) + F_{x,2R} \cdot \sin(\delta_{2R} - \beta_{ref}) \\ & + F_{y,1L} \cdot \cos(\delta_{1L} - \beta_{ref}) + F_{y,1R} \cdot \cos(\delta_{1R} - \beta_{ref}) \\ & + F_{y,2L} \cdot \cos(\delta_{2L} - \beta_{ref}) + F_{y,2R} \cdot \cos(\delta_{2R} - \beta_{ref}) \end{aligned} \quad \text{(G.4)}$$

and in yaw direction:

$$\begin{aligned} M_{p3} = \; & L_F \cdot (F_{x,1L} \cdot \sin(\delta_{1L}) + F_{y,1L} \cdot \cos(\delta_{1L})) \\ & -\frac{1}{2} \cdot S_F \cdot (F_{x,1L} \cdot \cos(\delta_{1L}) - F_{y,1L} \cdot \sin(\delta_{1L})) \\ & +L_F \cdot (F_{x,1R} \cdot \sin(\delta_{1R}) + F_{y,1R} \cdot \cos(\delta_{1R})) \\ & +\frac{1}{2} \cdot S_F \cdot (F_{x,1R} \cdot \cos(\delta_{1R}) - F_{y,1R} \cdot \sin(\delta_{1R})) \\ & -L_R \cdot (F_{x,2L} \cdot \sin(\delta_{2L}) + F_{y,2L} \cdot \cos(\delta_{2L})) \\ & -\frac{1}{2} \cdot S_R \cdot (F_{x,2L} \cdot \cos(\delta_{2L}) - F_{y,2L} \cdot \sin(\delta_{2L})) \\ & -L_R \cdot (F_{x,2R} \cdot \sin(\delta_{2R}) + F_{y,2R} \cdot \cos(\delta_{2R})) \\ & +\frac{1}{2} \cdot S_R \cdot (F_{x,2R} \cdot \cos(\delta_{2R}) - F_{y,2R} \cdot \sin(\delta_{2R})) \qquad [Nm] \end{aligned} \tag{G.5}$$

where the reference side slip angle β_{ref} in the center of gravity of the vehicle is calculated as

$$\beta_{ref} = \theta_{ref} - \psi_{ref} \tag{G.6}$$

with

$$\theta_{ref} = atan\left(\frac{\dot{y}_{g,ref}}{\dot{x}_{g,ref}}\right) \tag{G.7}$$

L_F, L_R, S_F and S_R are the characteristic chassis dimensions. The combined longitudinal and lateral tyre forces as a function of the slip values κ_{ij} and α_{ij} are:

$$\begin{aligned} F_{x,ij} &= G(\alpha_{ij}, \kappa_{ij})_x \cdot D_{x,norm} \sin(C_{x,norm} \arctan(B_{x,norm} \cdot \kappa_{ij}))F_{z,ij} \qquad [N] \\ F_{y,ij} &= G(\alpha_{ij}, \kappa_{ij})_y \cdot D_{y,norm} \sin(C_{y,norm} \arctan(B_{y,norm} \cdot \alpha_{ij}))F_{z,ij} \qquad [N] \end{aligned}$$

with

$$\alpha_{ij} = \tan(\delta_{ij} - \delta_{ideal,ij}) \tag{G.8}$$

The ideal steer angles based on the reference vehicle velocities are calculated as

$$\delta_{ideal,ij} = atan\left(\frac{\nu_{ref,y,ij}}{\nu_{ref,x,ij}}\right) \tag{G.9}$$

with

$$\nu_{ref,x,1L} = v_{ref,x} - S_f/2 \cdot \dot{\psi}_{ref} \tag{G.10}$$
$$\nu_{ref,y,1L} = v_{ref,y} + L_f \cdot \dot{\psi}_{ref} \tag{G.11}$$
$$\nu_{ref,x,1R} = v_{ref,x} + S_f/2 \cdot \dot{\psi}_{ref} \tag{G.12}$$
$$\nu_{ref,y,1R} = v_{ref,y} + L_f \cdot \dot{\psi}_{ref} \tag{G.13}$$
$$\nu_{ref,x,2L} = v_{ref,x} - S_r/2 \cdot \dot{\psi}_{ref} \tag{G.14}$$
$$\nu_{ref,y,2L} = v_{ref,y} - L_r \cdot \dot{\psi}_{ref} \tag{G.15}$$
$$\nu_{ref,x,2R} = v_{ref,x} + S_r/2 \cdot \dot{\psi}_{ref} \tag{G.16}$$
$$\nu_{ref,y,2R} = v_{ref,y} - L_r \cdot \dot{\psi}_{ref} \tag{G.17}$$

and the reference velocities in the center of gravity

$$\begin{bmatrix} v_{ref,x} \\ v_{ref,y} \end{bmatrix} = \begin{bmatrix} \cos(\psi_{ref}) & \sin(\psi_{ref}) \\ -\sin(\psi_{ref}) & \cos(\psi_{ref}) \end{bmatrix} \cdot \begin{bmatrix} \dot{x}_{g,ref} \\ \dot{y}_{g,ref} \end{bmatrix} \tag{G.18}$$

For notational simplicity the ideal steer angles are calculated with the use of the global reference coordinates $[x_{g,ref} \;\; y_{g,ref} \;\; \psi_{ref}]^T$ and derivatives in stead of the operational space coordinates in the state vector p_{ref} of the control model.

Appendix H

On the control of an autonomous four wheel steer and four wheel drive high performance vehicle

This appendix contains the abstract:

> "On the control of an autonomous four wheel steer and four wheel drive high performance vehicle"

submitted to the 7th International Symposium on Advanced Vehicle Control, 23-27 August 2004, HAN University Arnhem, The Netherlands.

The co-authors of this paper are Jeroen Ploeg, Luc Moreau and Henk Nijmeijer.

On the control of an autonomous four wheel steer and four wheel drive high performance vehicle

Roel Leenen[1], Jeroen Ploeg[2], Luc Moreau[3] and Henk Nijmeijer[4]

Eindhoven University of Technology, Department of Mechanical Engineering, Dynamics and Control Technology Group, P.O. Box 513, 5600 MB Eindhoven, The Netherlands. [2]TNO Automotive, Department of Advanced Chassis and Transport Systems, P.O. Box 756, 5700 AT Helmond, The Netherlands.
[1]R.Leenen@tue.student.nl, [2]Ploeg@wt.tno.nl, [3]L.P.M.Moreau@tue.nl, [4]H.Nijmeijer@tue.nl.

Abstract:
Within the framework of a full-scale hardware-in-the-loop intelligent vehicle simulator called VEHIL [3], an automatic guided vehicle is developed in order to simulate traffic participants. This vehicle, called ATS/AGV, is based on a four wheel steer and four wheel drive concept which allows for a high handling performance in combination with the ability to carry out very complex manoeuvres [2]. Moreover, its dynamic response to position commands has to exceed the handling performance of modern road vehicles considerably. This results in a set of control requirements for the ATS/AGV that is new in the world of automated vehicles. See figure H.1 for an illustration of the ATS/AGV. Table H.1 lists the main ATS/AGV specifications. A linear control system for the trajectory tracking of the ATS/AGV is designed, implemented and evaluated in [4]. Based on this research a more advanced nonlinear control method is proposed in this study which enables the high performance control of the ATS/AGV.
What distinguishes the ATS/AGV from most of the other wheeled mobile robots or automated vehicles are the extreme manoeuvring and accelerating requirements of the vehicle. Because of this, wheel slip can not be neglected in the control design. Furthermore, the total of eight actuators are independently controllable. Since there are more actuator inputs than control objectives in the motion control problem the vehicle is considered to be an overactuated system. While controlling the motion of the vehicle one typically has to deal with the redundant number of actuators.
This paper proposes a nonlinear control system which enables independent four wheel steering and independent four wheel torque control for a high performance automatic guided vehicle. Special attention is paid to the integration of wheel slip into the control design. The objective of the control algorithm is to enable the independent control of the longitudinal translation, lateral translation and orientation angle of the vehicle up to limit tyre-adhesion conditions.
A control model is formulated which describes the force and momentum equilibria in the center of gravity of the vehicle. The empirical tyre model of Pacejka [1], called the 'Magic Formula', is used to represent the steady-state force/slip-characteristics of the tyre in the control model. The steer and drive actuator dynamics are neglected in the control model. For the combined longitudinal, lateral and/or yaw manoeuvring of the vehicle there typically exist more than one allowable actuator configurations. Therefore, it is hypothesized that the 'optimal' coordination of the redundant number of actuators has to be directed through the use of optimization techniques in combination with the formulation of a performance criterium. Finally, an objective function

consisting of the model error equations, the estimated vertical wheel loads and some additional constraints is formulated in order to deal with the redundant number of actuators. In the control system, the objective function is minimized once during each sample interval using the previous obtained 'minimum' as an initial starting guess in the iterative optimization process. The minimization of the objective function results in four reference wheel rotational velocities and four reference steer angles. The steer and drive commands are dealt with by closing local loops around each steering and driving motor; the presence of large friction forces makes it a necessity to apply servo control. Furthermore, estimated longitudinal tyre forces are used in the feedforward compensation for the drive actuators in order to increase the tracking performance.
The experimental environment in the VEHIL laboratory provides a perfectly flat road surface with a well known tyre/road-friction behavior. This implies that the nonlinear force/slip-characteristics of the tyre are known a-priori. These two conditions are the minimum requirements for a proper active coordination of the four wheel steering and four wheel driving control. Nevertheless, the proposed nonlinear control system accounts for the weight transfer of the vehicle in the coordination of its actuators.
The results are illustrated through computer simulation and experiments conducted with the ATS/AGV test facility depicted in figure H.1. It is shown that the vehicle manoeuvrability and stability can be remarkably improved near limit cornering and accelerating conditions. Because of the implemented steady-state force/slip-characteristics in the control model, the control system explicitly handles the control saturation.

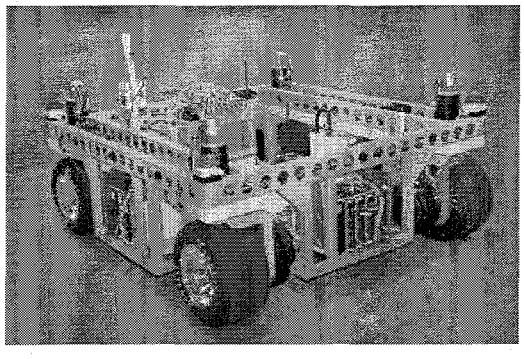

Figure H.1: The ATS/AGV

vehicle mass	487 kg
wheel base	1.4 m
track width	1.4 m
maximum speed	50 km/h
maximum acceleration	10 m/s^2
battery power	30 kW
acceleration from 0 to 50 km/h	2.1 s

Table H.1: Specifications of ATS/AGV

References

1 Pacejka, H.B., The tyre as a vehicle component, Proceedings of XXVI Fisita Congress, Prague, Czech Republic, June 16-23, 1996.

2 Ploeg, J., Knaap, A.C.M. van der., Verburg, D.J., ATS/AGV - Design, Implementation and Evaluation of a High Performance AGV, Proceedings IEEE Intelligent Vehicle Symposium IV 2002, Versailles, France, June 18-20, 2002.

3 Verburg, D.J., Ploeg, J., Knaap, A.C.M. van der., VEHIL - Developing and Testing Intelligent Vehicles, Proceedings IEEE Intelligent Vehicle Symposium IV 2002, Versailles, France, June 18-20, 2002

4 Ploeg, J., Trajectory tracking for an all wheel steer and all wheel drive automatic guided vehicle, paper for submission, AVEC'04